UNIVERSITY OF CALIFORNIA SAN DIEGO

Context dependence of cancer cell migration and metastasis

A dissertation submitted in partial satisfaction of the
requirements for the degree
Doctor of Philosophy

in

Bioengineering

by

Daniel Ortiz Vélez

Committee in charge:

Professor Stephanie I. Fraley, Chair
Professor Hannah Carter
Professor Adam J. Engler
Professor Yingxiao (Peter) Wang
Professor Jing Yang

2018

The dissertation of Daniel Ortiz Vélez is approved, and it is acceptable in quality and form for publication on microfilm and electronically:

_____

_____

_____

_____

_____

Chair

University of California San Diego

2018

DEDICATION

Para Mari, who has been by my side all along.

EPIGRAPH

Pensar es tener los ojos enfermos

-Bajo Tierra

TABLE OF CONTENTS

LIST OF FIGURES

LIST OF TABLES

ACKNOWLEDGEMENTS

I would like to thank Dr. Stephanie Fraley, for mentoring me during all my PhD. For trusting me with being a pioneer in her lab and for leading by example with hard work.

I like to thank Dr. Pedro Cabrales, for giving me the opportunity to join his group and enter the PhD. program at UCSD. The time I spent under his tutoring has been incredibly important for everything I have done since.

Chapter I, is a partial reprint of ”3D collagen architecture induces a conserved migratory and transcriptional response linked to vasculogenic mimicry” as it appears on *Nature communications* 8, 1651 (2017). Velez, D.O., Tsui, B., Goshia, T., Chute, C., Han, A., Carter, H., Fraley, S. 3D collagen architecture induces a conserved migratory and transcriptional response linked to vasculogenic mimicry. The dissertation author was the primary investigator and author of this paper.

Chapter II, is a partial reprint of Velez, D.O , S.K. Ranamukhaarachchi , R.N. Modi , A. Kumar , A. J Engler , S.I. Fraley ”Collagen architecture-induced metabolic and oxidative stress precede collective migration”. Which has been submitted for publication. The dissertation author was the primary investigator and author of this paper.

Chapter III contains preliminary data and proposed future work.

VITA

2010	B. S. in Biomedical Engineering, EIA-CES, Medellin, Colombia
2012	MS. in Mechanical Engineering, Universidad de los Andes, Bogota, Colombia
2013-2014	Research Assistant, University of California San Diego
2018	Ph. D. in Bioengineering, University of California San Diego

PUBLICATIONS

Zhang, W., Bojorquez, A., **Velez, D.O.**, Shen, JP., Xu,G., Chen, K., Licon,K., Melton, C.,Olson, K., Yu,M., Huang, J., Carter, H., Farley, E., Snyder, M., Fraley, SI., Kreisberg, J., Ideker, T. A global transcriptional network connecting noncoding mutations to changes in tumor gene expression. *Nature Genetics*, doi:10.1038/s41588-018-0091-2 (2018).

Velez, D.O., Tsui, B., Goshia, T., Chute, C., Han, A., Carter, H., Fraley, S. 3D collagen architecture induces a conserved migratory and transcriptional response linked to vasculogenic mimicry. *Nature communications* 8, 1651 (2017).

Velez, D. O., Mack, H., Jupe, J., Hawker, S., Kulkarni, N., Hedayatnia, B., Zhang, Y., Lawrence, S. , Fraley, S. I. Massively parallel digital high resolution melt for rapid and absolutely quantitative sequence profiling. *Scientific reports* 7 (2017).

Kar, M., Shih, Y.-R. V., **Velez, D. O.**, Cabrales, P. , Varghese, S. Poly (ethylene glycol) hydrogels with cell cleavable groups for autonomous cell delivery. *Biomaterials*— 77, 186-197 (2016).

Stobdan, T., Zhou, D., Ao-Ieong, E., **Ortiz, D.**, Ronen, R., Hartley, I., Haddad, G. G. (2015). Endothelin receptor B, a candidate gene from human studies at high altitude, improves cardiac tolerance to hypoxia in genetically engineered heterozygote mice. *Proceedings of the National Academy of Sciences* 12(33), 10425-10430.

Yalcin, O., **Ortiz, D.**, Williams, A. T., Johnson, P. C. , Cabrales, P. Perfusion pressure and blood flow determine microvascular apparent viscosity. *Experimental physiology* 100, 977-987 (2015)

Liong, C., **Ortiz, D.**, Ao-ieong, E., Navati, M. S., Friedman, J. M., Cabrales, P. (2014). Localized increase of tissue oxygen tension by magnetic targeted drug delivery *Nanotechnology*, 25(26) 265102.

Ortiz, D., Briceno, J. C., Cabrales, P. (2014). Microhemodynamic parameters quantification from intravital microscopy videos. *Physiological measurement*,35(3), 351.

Ortiz, D., Barros, M., Yan, S., Cabrales, P. (2014). Resuscitation from hemorrhagic shock using polymerized hemoglobin compared to blood. *The American journal of emergency medicine*, 32(3), 248-255.

Ortiz, D., Cabrales, P., Briceno, J. C. Transport of nitric oxide by perfluorocarbon emulsion. *Biotechnology progress* (2013) 29.6 (2013): 1565-1572

Yalcin, O., **Ortiz, D.**, Tsai, A. G., Johnson, P. C., Cabrales, P. Microhemodynamic aberrations created by transfusion of stored blood. *Transfusion* (2013) 54.4 (2014): 1015-1027

Vásquez, D. M., **Ortiz, D.**, Alvarez, O. A., Briceno, J. C., Cabrales, P. Hemorheological implications of perfluorocarbon based oxygen carrier interaction with colloid plasma expanders and blood. *Biotechnology progress* 29, 769-807 (2013).

ABSTRACT OF THE DISSERTATION

Context dependence of cancer cell migration and metastasis

by

Daniel Ortiz Vélez

Doctor of Philosophy in Bioengineering

University of California San Diego, 2018

Professor Stephanie I. Fraley, Chair

Cancer is a leading cause of death worldwide. During metastasis, cells from a primary tumor escape, invade local tissues and spread to distant organs. Even though this process represents the highest risk for cancer related death, a lot remains unknown about the principles behind its beginning and progression. The main barrier that cancer cells face at each step of the metastatic process is a complex 3D extracellular matrix (ECM), which they need to bind to, pull on and degrade. In this dissertation I use 3D culture systems to mimic a native 3D ECM *in vitro*, to quantitatively study the role of the ECM structure and physical properties on the development of invasive phenotypes and gene expression programs.

In chapter 1, I identified a switch to a highly persistent and polarized cell motility in a high density environment and discovered that cells undergoing this migration formed multicellular structures. Using RNA sequencing I found an upregulated 70 gene module that together with the motility response has been describes as vasculogenic mimicry (VM). I show evidence that the identified transcriptional program predicts survival in patient data across nine distinct tumor types, suggesting it may represent a conserved metastatic response.

In chapter 2, I investigate the biophysical mechanisms of cell-ECM interactions. I find that matrices with low degradability limit cell adhesion. Cells in these matrices display hallmarks of anchorage independent growth, including oxidative stress. They show decreased expression of several mTOR target genes and downregulation of TCA cycle and pyruvate metabolism pathways. Lastly, I show that as part of the response to low adhesion state, cells upregulate key NOTCH signaling molecules.

In chapter 3, I propose the use of *in vivo* models to deconstruct the role of collagen density in promoting cancer cell metastasis. I present preliminary data and future directions for these *in vivo* models.

The data presented in this dissertation provides a multiscale view of the role of the collagen microenvironment in the development of cancer cell invasive motility and metastatic phenotypes. The discoveries presented hereby highlight the value of using 3D culture assays in combination with quantitative analysis to uncover biological phenomenon with high translational potential.

Chapter 1

3D collagen architecture induces a conserved migratory and transcriptional response linked to vasculogenic mimicry

1.1 Introduction

An initial step in cancer metastasis is the migration of tumor cells through the extracellular matrix (ECM) and into the lymphatic or vascular systems[1]. Several features of the tumor ECM have been associated with progression to metastasis. In particular, regions of dense collagen are co-localized with aggressive tumor cell phenotypes in numerous solid tumors[2], including breast[3], ovarian[4], pancreatic[5] and brain cancers[6]. However, sparse and aligned collagen fibers at the edges of tumors have also been reported to correlate with aggressive disease[7]. It remains unclear whether and how collagen architectures have a role in driving metastatic migration programs or if they simply correlate with progression of the tumor.

Intravital microscopy studies have shown that distinct collagen architectures are associated with specific cell motility behaviors. Cancer cells migrating through densely packed collagen

within the tumor use invadopodia and matrix metalloproteinase (MMP) activity to move, whereas cells in regions with less dense collagen and long, aligned fibers migrate rapidly using larger pseudopodial protrusions or MMP-independent ameboid blebbing[8, 9]. Likewise, we previously showed *in vitro* that cell migration speed, invasion distance, and cellular protrusion dynamics are modulated by collagen fiber alignment, but that this relationship breaks down at high collagen densities (>2.5 mg ml^{-1})[10]. These findings suggest that distinct motility regimes exist in low-density and high-density collagen, which may have implications for metastatic progression.

1.2 Results

1.2.1 High-density collagen promotes fast and persistent migration

To first investigate the role of 3D collagen density in modulating the migration phenotype of breast cancer cells, we embedded MDA-MB-231 cells in collagen I matrices at densities mimicking normal breast tissue, 2.5 mgmL^{-1} collagen and cancerous breast tissue, 6 mgmL^{-1} collagen[10, 11]. We observed that cells migrating in dense collagen initially appeared to be trapped and were unable to invade. However, after one division cycle, most cells switched to a highly invasive motility behavior, significantly increasing their persistence, velocity, and total invasion distance (Fig. 1.1 a-d, left panels). This behavior was not observed in cells embedded in the low-density matrix, where cell migration was the same before and after division (Fig. 1.1 a-d, right panels). Interestingly, cells that were in contact with the coverslip and not fully embedded in the high-density condition did not undergo the same migration transition upon division (Supplementary Fig. 1.1 a, b). The motility responses we observed in 2.5 and 6 mgmL^{-1}collagen matrices were not unique to MDA-MB-231 breast cancer cells. Similar migration patterns were observed for HT-1080 fibrosarcoma cells embedded in the same collagen matrix conditions (Supplementary Fig. 1.1c), suggesting that these responses may be conserved among distinct cancer types. To further examine whether the observed migration behavior was

cell-type dependent, we tested the response of normal mesenchymal human foreskin fibroblasts (HFF-1) to low-density and high-density collagen conditions. Over an observation period of 48h, HFF cells migrated consistently with very low persistence. Cells invaded less than three cell lengths in low-density collagen. In high density, HFFs elongated to reach cell lengths up to 300μm but did not invade significantly (Supplementary Fig. 1.1d).

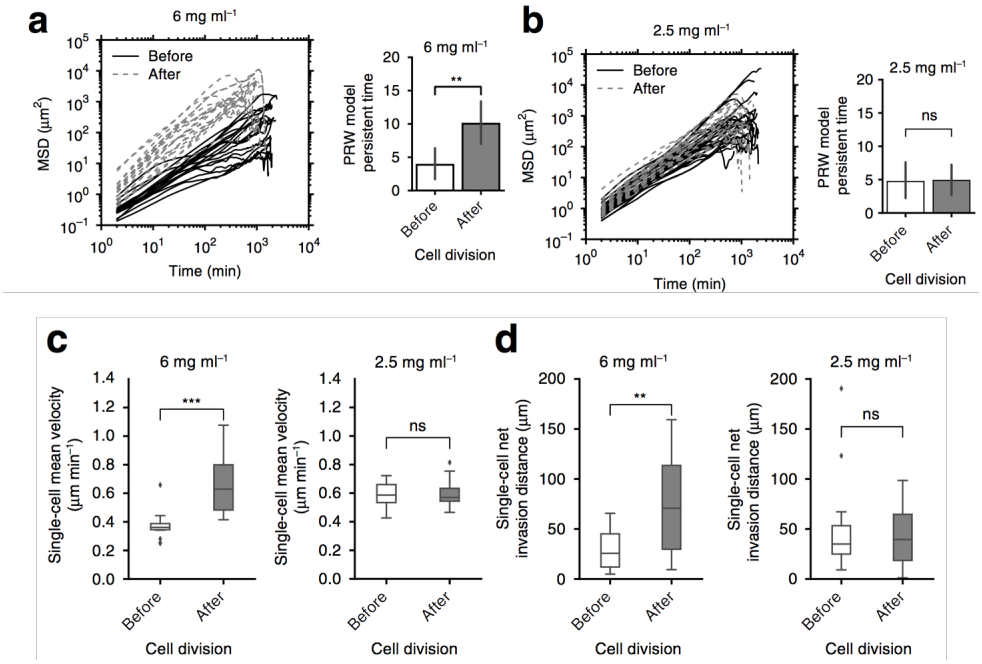

Figure 1.1: **High-density 3D collagen microenvironment promotes a switch to persistent cell migration in cancer cells. a.**Mean squared displacement (MSD) and persistent time of MDA-MB-231 cells before and after cell division in high-density collagen. The persistent time was calculated from the MSDs using the persistent random walk model (see *Methods*). MSDs are shown for 12 representative cell trajectories. **b.**Mean MSD and persistent time of MDA-MB-231 cells before and after cell division in low-density collagen. The persistent time was calculated from the MSDs using the persistent random walk model (see *Methods*). MSDs are shown for 12 representative cell trajectories. **c.** Single-cell velocity measured at 2min intervals before and after cell division. **d.** Single-cell net invasion distance before and after cell division for cells in high-density and low-density collagen. Box plots show quartiles of the dataset with whiskers extending to first and third quartiles. n=3 biological replicates for all experiments unless otherwise noted. Statistical significance was determined by Mann-Whitney U test and is indicated as *, **, *** for $p<0.05$, $p<0.01$, $p<0.001$, respectively

1.2.2 Density-induced migration results in cell network structures

It was unexpected that both MDA-MB-231 and HT-1080 cancer cells migrated faster and further in high-density collagen conditions. Intuitively, cell migration would be expected to slow in dense conditions where more matrix must be remodeled to enable cell movement. Moreover, this behavior was common to both cancer cell types but not displayed by normal fibroblasts, which represent residents of the stroma and also undergo mesenchymal migration in collagen. This motivated us to investigate the long-term implications of the rapid migration phenotype induced in cancer cells under high-density conditions. After 1 week of culture in high-density collagen, breast cancer cells undergoing rapid, and persistent migration formed interconnected network structures that resembled the early stages of endothelial tubulogenesis (Fig. 1.2a, left). The average length of cell networks after 1 week was 437μm (Fig. 1.2 b). Interestingly, these network structures do not appear to be caused by cells aligning along collagen fibers (Supplementary Fig. 1.1e). In contrast, cells cultured in low-density collagen for 1 week migrated slowly with low persistence, and remained as single cells (Fig. 1.2 a, right). HT-1080 cells also formed network structures in high-density collagen and remained as single cells in low-density collagen (Supplementary Fig. 1.1 f). HFFs remained as single cells in both high-density and low-density conditions (Supplementary Fig. 1.1g). The transition of cancer cells from single-cell migration to network formation suggested a potential transdifferentiation event, and the cell networks were reminiscent of a cancer phenotype known as vasculogenic mimicry (VM). VM is thought to arise from tumor cells that acquire the ability to form networks in the tumor ECM lined with glycogen-rich molecules and basement membrane proteins that can be perfused with blood. However, the tumor cells lining these networks do not express endothelial surface markers such as CD31[5, 6]. Periodic acid schiff (PAS) staining of the networks formed in our high-density collagen condition confirmed the presence of glycogen-rich molecules (Fig. 1.2 c) and immunofluorescence confirmed the presence of basement membrane protein COL4A1 (Fig. 1.2 d), as in VM.

Previous pioneering studies have shown that several aggressive melanoma cell lines, which produce VM *in vitro* also intrinsically form VM network structures when cultured on top of Matrigel or collagen I in a 2D *in vitro* context [12, 13]. Recently, other aggressive tumor cell types have been shown to intrinsically form VM-like network structures on top of Matrigel or in 2.5D culture in Matrigel [14, 15, 16, 17, 18]. Here, it is important to note that variations exist in the consistency of commercial ECM products as well as the terminology used to describe 3D culture. We define 3D culture strictly as a condition where cells are fully embedded, in contact with ECM on all sides, and located a sufficient distance away from the coverslip bottom and sides of the culture dish to avoid their influence. We define 2.5D culture as a pseudo 3D culture where cells are embedded in the ECM but in contact with coverslip. Our previous studies have demonstrated the importance of these distinctions, as cell behavior and protein localization are differentially regulated in each context [19, 20, 21]. Therefore, we sought to understand whether the network phenotype induced by a 3D collagen I environment was distinct from that induced by a 2D Matrigel environment. First, we asked whether our cells formed network structures on top of Matrigel. Few cells aligned within the first 24hrs of culture, and nearly all cells aggregated after 72 h (Fig. 1.2 e). Next, we embedded MDA-MB-231 cells inside of Matrigel, in 3D culture. In this context, cells did not form network structures but instead formed rough-edged, disorganized spheroids (Fig. 1.2 f). Thus, high-density collagen uniquely induced the network-forming phenotype in a more physiologically relevant 3D context.

1.2.3 A conserved transcriptional response precedes migration

We hypothesized that the persistent migration phenotype of cancer cells leading to network formation in high-density collagen conditions (collagen-induced network phenotype, CINP) could be the result of a transdifferentiation event wherein a unique cell motility gene module was upregulated. To test this, we conducted RNA sequencing of MDA-MB-231, HT-1080, and HFF cells cultured in low-density and high-density collagen matrices after 24h (Fig. 1.3 a), the time

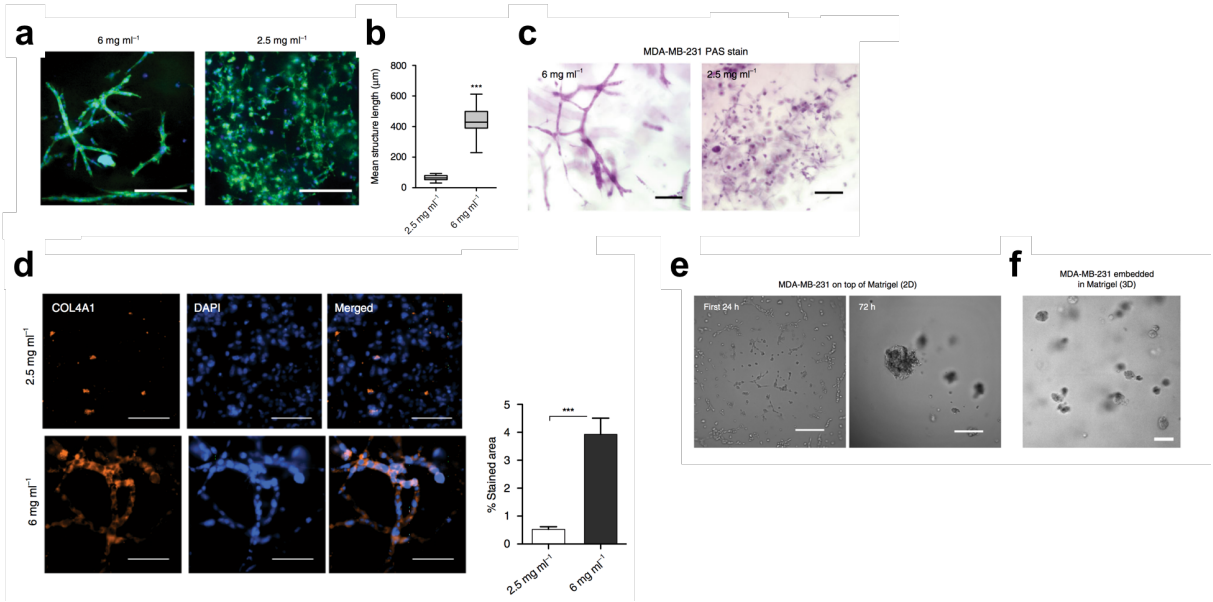

Figure 1.2: **Density-induced migration results in cell network structures. a.** Representative image of MDA-MB-231 cells cultured in a 6 mgmL^{-1}(left) and in a 2.5mgmL^{-1} (right) collagen I matrix after 7 days of culture. Cells are stained with Alexa-488 Phalloidin (F-Actin) and DAPI (nuclei). Scale bar 250μm. **b.** Quantification of mean structure length in low-density and high-density collagen, from images acquired in three independent experiments. **c.** PAS stain of MDA-MB-231 cells cultured for 7 days in a 3D collagen gel of high-density (left) and low-density (right). Scale bar 100μm. **d.** Immunofluorescence staining of MDA-MB-231 cells for collagen IV after 7 days of culture in 6 vs. 2.5 mgmL^{-1}. Representative images of n=2 biological replicates. Bar graph shows mean and s.e.m. of quantification of stained area performed in 15 different fields of view. Scale bar 100 μm. **e.** MDA-MB-231 cells cultured on top of growth factor-reduced matrigel after 24h (left) and after 72 h (right). Scale bar 250 μm. **f.** MDA-MB-231 cells cultured inside growth factor-reduced matrigel in 3D culture for 7 days. Scale bar 100 μm. Box plots show quartiles of the dataset with whiskers extending to first and third quartiles. n=3 biological replicates for all experiments unless otherwise noted. Statistical significance was determined by Mann-Whitney U test and is indicated as *, **, *** for $p<0.05$, $p<0.01$, $p<0.001$, respectively

point just before most cancer cells in the high-density collagen matrix underwent at least one cycle of cell division and began to invade with increased persistence. As the majority of cancer cells cultured under high-density conditions participated in network formation, we expected their bulk transcriptional profile to be dominated by this phenotype[22]. Then we asked whether common stem cell and differentiation markers were upregulated in association with the network-forming phenotype. Indeed, several known stem cell markers were upregulated (Fig. 1.3 b), and three

were common to both cancer cell types: JAG1, ITGB1, and FGFR1. This suggested that both cancer cell types harbored stem-like qualities, which could facilitate significant transcriptional reprogramming.

Analyzing more broadly, we then asked which genes were differentially regulated (TPM fold change >1.5) in high-density collagen compared to low-density collagen in each cell type and whether these genes represented unique or conserved transcriptional response modules. As expected, cell type accounted for the most variance in gene expression (Fig. 1.3 c). However, after a z-score transformation of the gene expression of each cell type, the collagen matrix condition accounted for the bulk of the remaining variance in gene expression (Fig. 1.3 d). This suggested the presence of gene expression programs linked to collagen matrix conditions.

Using a Venn diagram approach to identify conserved expression modules, we discovered a set of 70 genes that were upregulated by both cancer cell types but not normal cells in response to high-density collagen (Fig. 1.4 a; Supplementary Fig. 2a). Gene ontology (GO) enrichment analysis revealed that these 70 common-to-cancer genes were significantly enriched for annotations in blood vessel development and regulation of migration (Fig. 1.4 b,c). Importantly, changes in the threshold for differential expression did not significantly alter the primary gene ontology categories identified (Supplementary Fig. 2d; Supplementary Table 1). Key genes involved in Notch signaling, i.e., RBPJ and LFNG, were among the 70. Importantly, LAMC2, JAG1, and THBS1 genes identified in this common-to-cancer gene set have been previously associated with a VM phenotype intrinsically displayed by metastatic melanoma, which was assessed by targeted microarray analysis for angiogenesis, ECM, and cell adhesion genes [23, 24]. Upregulated surface markers were not endothelial in nature, and did not represent any specific tissue or cell type (Fig. 1.4 c).

Further exploration of our dataset with respect to individual cancer cell types revealed that, beyond the conserved transcriptional response, high-density collagen also triggered the expression of genes related to vasculogenesis in a cell type-dependent manner. For example, breast

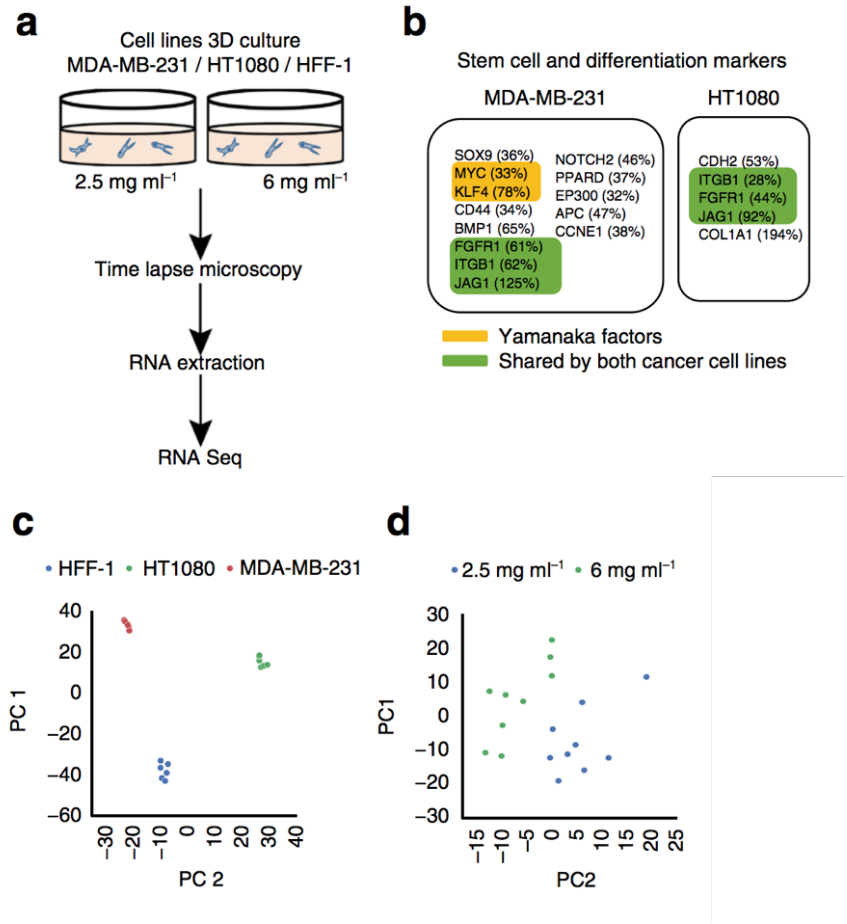

Figure 1.3: **Differential transcriptional states modulated by 3D extracellular matrix a.** Schematic of the experimental approach. Each cell line in each condition was cultured in biological triplicate, and each replicate was sequenced (n=3 for each cell type per condition). **b.** List of genes upregulated in each of the cancer cell lines that are known stem cell or differentiation markers. **c.** Principal component analysis of raw RNA-Seq data shows cell type as main driver of variance in gene expression. **d.** Principal component analysis of z-score transformed data shows culture condition as the main driver of variance in gene expression.

cancer cell networks upregulated VEGFA fold change= 1.65 and MMP14 fold change=1.72, but fibrosarcoma cell networks did not. Some of these genes have been previously associated with the VM network phenotype of melanoma cells (Supplementary Fig. 2c) [23].

Next, we assessed the 35 genes that were upregulated in response to high-density collagen by all three cell types (Fig. 1.4 a). These genes were enriched primarily for annotations in regulation of cell differentiation (Fig. 1.4 d). However, it is important to take into account the

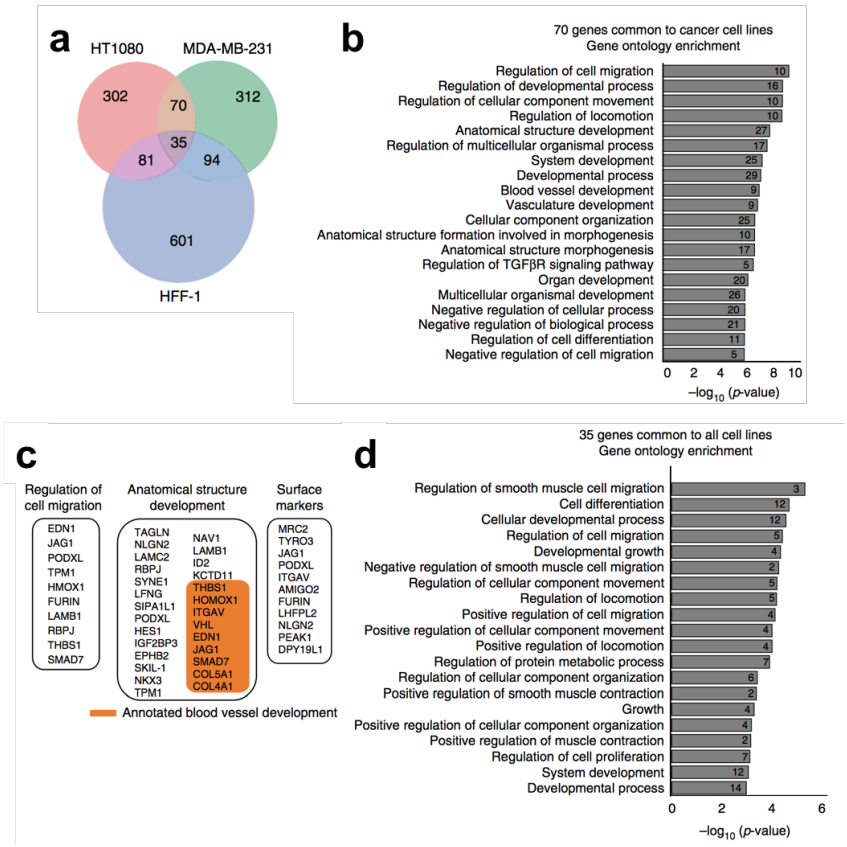

Figure 1.4: **A conserved transcriptional response precedes migration a.** Venn diagram showing the overlap between genes upregulated in 6 vs. 2.5 mgmL^{-1} collagen in the three cell lines analyzed. **b.** Gene ontology (GO) of biological processes enriched in the 70 genes upregulated by cancer cells in 6 mgmL^{-1}collagen. Number at the end of the bars represents number of genes annotated for the particular GO term. **c.** Lists of genes with annotations relevant to the observed phenotype. Left: regulation of cell migration. Middle: regulation of anatomical structure development. Orange color highlights genes annotated for blood vessel development. Right: surfance markers. **d.** GO of biological processes enriched in the 35 genes shared by cancer cells and HFF-1 fibroblasts. Number at the end of the bars represents number of genes annotated for the particular GO term. See *Methods* for analysis details.

inherent flaws associated with GO enrichment analysis. For example, some categories showing enrichment in the 35 genes common-to-all cell lines contain very few genes and may not represent real enrichment. However, this limitation is not observed in the top enriched categories in the 70 genes common-to-cancer cells, where most category contains at least 10 genes (Fig. 1.4 b). The genes associated with each enrichment category are given in Supplementary Tables 2 and 3.

Interestingly, SERPINE1, a secreted protease inhibitor involved in coagulation and inflam-

mation regulation, was identified in the common-to-all gene module (Supplementary Fig. 2b). Several Serpine protein family members have previously been implicated as drivers of metastasis correlating with VM [17] and with brain metastases of lung and breast cancers [25].

1.2.4 Physical properties of the 3D ECM involved in CINP

We next sought to identify the matrix feature triggering transdifferentiation. The physical parameters of stiffness, pore size, and fiber organization differ between the low density 2.5 mgmL^{-1} and high density 6 mgmL^{-1} collagen matrices [26] . Chemical cues may also change. For example, adhesive ligand density and binding site presentation to integrins and other matrix receptors may differ [27, 28]as well as accumulation or release of autocrine and paracrine signals sequestered by the ECM [29, 30, 31]. Each of these features could potentially impact cancer cell motility behavior and gene expression.

As matrix stiffness has been implicated in driving epithelial-to-mesenchymal transitions (EMT) and aggressive phenotypes [4, 22, 23] we first asked whether increased stiffness of the high-density collagen matrix was responsible for triggering transdifferentiation. To test this, we developed a collagen polymerization procedure (*Methods*) that increases the stiffness of the low-density matrix to match the stiffness of the high-density matrix (Fig. 1.5a). By lowering the polymerization temperature from 37 to 20°C, polymerization slowed, allowing fibers to form more organized and reinforced fiber structures with larger pores (Supplementary Fig. 1I). Breast cancer cells cultured in this stiffened low-density condition did not undergo network formation (Fig. 1.5 b), suggesting that 3D stiffness is not sufficient for triggering the transdifferentiation.

Next, we sought to determine whether the smaller pore size of the high-density matrices triggered transdifferentiation. One way in which smaller pore sizes could influence cell behavior is by restricting the diffusion of molecules to and from the cells [32]. More specifically, the imbalance between oxygen diffusion to cells and oxygen consumption by cells in 3D matrices has been shown to promote hypoxic conditions in some cases [33]. Since regions of VM have

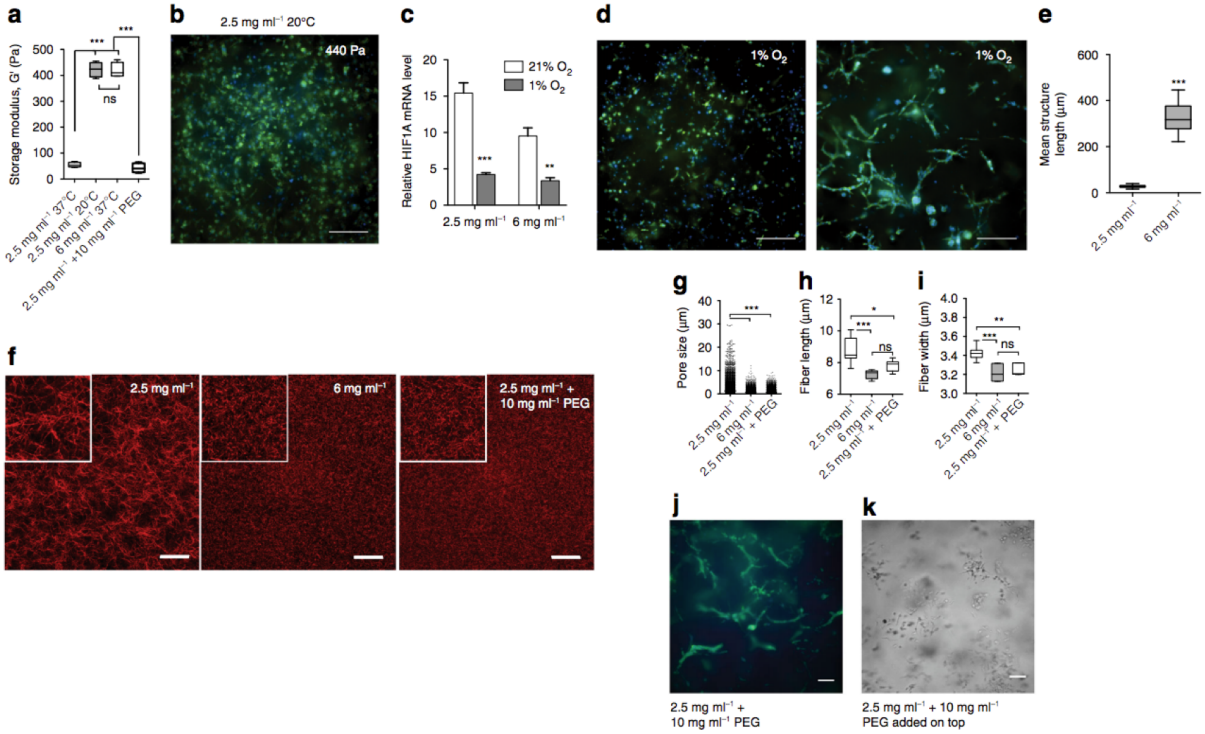

Figure 1.5: **Cell network formation is not triggered by hypoxia or matrix stiffness but rather by matrix architecture a.** Storage modulus of collagen gels as estimated by shear rheology after polymerization at different temperatures. **b.** Representative images of cells after 7 days of culture in low-density collagen polymerized at 20°C (high stiffness, 440Pa). **c.** HIF1 A expression in low-density and high-density 3D collagen after 7 days of culture under normoxic (21% O2) or hypoxic (1% O2) conditions. **d.** Representative images of MDA-MB-231 cells in low-density and high-density 3D collagen after 7 days of culture under hypoxic (1% O2) conditions, scale bar 250μm. **e.** Quantification of mean structure length after 7 days of culture under hypoxic (1% O2) conditions in low-density and high-density collagen. **f.** Confocal reflection images of collagen fibers in 3D matrices. Left: 2.5 mgmL^{-1} collagen I, center: 6 mgmL^{-1} collagen I, and right: 2.5 mgmL^{-1} collagen + 10 mgmL $^{-1}$ PEG. Insert shows a 2x zoom. Scale bar 100μm.**g.** Quantification of pore size in the three conditions showed in f. **h.** Fiber length and **i.** fiber width as measured from the confocal reflection images in the three conditions showed in f. **j.** Representative image of MDA-MB-231 cells cultured for 7 days in a 2.5 mgmL^{-1} collagen + 10 mgmL^{-1}PEG 3D matrix. Cells are stained with Alexa-488 Phalloidin (F-Actin) and DAPI (nuclei). Scale bar 250μm. **k.** Representative bright field image of MDA-MB-231 breast cancer cells cultured in a 2.5 mgmL^{-1} collagen matrix where 10 mgmL^{-1} PEG was added to the media after polymerization. Scale bar 125 μm. Bar graphs represent mean $\pm$s.d. and data in box and whiskers plots is presented using Tukey method. n=3 biological replicates for all experiments unless otherwise noted. Statistical significance was determined by ANOVA (a, c, g,i) and Mann Whitney U test (e) and is indicated as *, **, *** for $p<0.05$, $p<0.01$, $p<0.001$, respectively . Bars plots are mean $\pm$s.d

previously been associated with markers of hypoxia *in vitro* [34, 35], we hypothesized that cells in high-density collagen created a more hypoxic condition than in low-density collagen and that low-oxygen levels could trigger network formation. To test this, we cultured MDA-MB-231 cells in low-density collagen under a hypoxic atmosphere of 1% oxygen for 1 week. To confirm that a hypoxic response was achieved, we assessed the level of HIF1A mRNA expression by RT-qPCR at day 7 and found a significant decrease in HIF1A expression (Fig. 1.5 c). This is a common response to long-term hypoxia by various cancer cell lines [36, 37, 38]. However, hypoxia was not sufficient to induce network formation in any portion of the cancer cell population in the low-density collagen matrix (Fig. 1.5 d, left). For comparison, we also assessed the HIF1A mRNA expression of breast cancer cells cultured for 1 week in low-density collagen under 21% oxygen, in high-density collagen under 1% oxygen, and in high-density collagen under 21% oxygen (Fig. 1.5 c). These results suggested that cells cultured in high-density collagen experience increased hypoxia compared to cells cultured in low-density collagen under normal atmospheric conditions. Nevertheless, the hypoxic response achieved in low-density collagen under 1% oxygen exceeded that induced by high-density matrix alone. Cells in high-density matrix under 1% oxygen continued to predominately display a network phenotype (Fig. 1.5 d, right), but the average network length (Fig. 1.5 e) was significantly shorter than cells in high-density collagen under normoxic conditions (Supplementary Fig. 1h). Previous studies have reported that hypoxia is not sufficient to induce a VM phenotype in melanoma cells *in vitro* [12]. It is possible that *in vitro*, additional stromal cell secreted factors or cell-cell interactions modulated by hypoxia may indirectly influence the VM process[35, 39].

To further explore whether pore size reduction induced transdifferentiation of cancer cells, we sought to interrogate this parameter independently of collagen density. In our model, the high-density condition contains 2.4 times more collagen than the low-density condition. This increase in total collagen reduces pore size, but also presents more adhesive ligands to cells, which could increase integrin activation. To separate pore size from bulk density, we developed

a collagen structure engineering technique that reduced the pore size and fiber length of the low-density matrix to approximate that of the high-density matrix. Under normal polymerization conditions, low-density collagen self-assembles into relatively long, structured fibers. When non-functionalized, inert polyethylene glycol (PEG) was mixed into collagen monomer solution prior to polymerization, molecular crowding-restricted fiber formation. This resulted in shorter, more interconnected fibers yielding smaller pores (Fig. 1.5f-i) without increasing stiffness (Fig. 1.5a). Breast cancer cells encapsulated in this pore size-reduced low-density matrix underwent network formation over the course of 1 week (Fig. 1.5j). To control for the possible influence of PEG itself, PEG was added into media on top of a normally polymerized low-density gel embedded with cells and allowed to diffuse into the interstitial spaces among the fibers to reach the same final concentration as was used in the pore size-reduced low-density matrix (10 mg/mL^{-1} PEG). Cells maintained in this molecularly crowded condition over 1 week did not form networks, but instead remained as single cells. However, a noticeable slowing of cell migration occurred, which resulted in an anisotropic patterning of single cells throughout the matrix (Fig. 1.5 k). These results suggested that the fiber architecture of high-density collagen induces network formation independently of the bulk increase in adhesive ligand density and confirms that bulk matrix stiffness is not involved.

1.2.5 Integrin-β1 upregulation is required for CINP

The short, more isotropic arrangement of fibers associated with both the high-density collagen and low-density PEG crowded collagen conditions could act on cells through local cell-matrix interactions transduced by integrin signaling. Integrin-β1 (ITGB1) is a canonical receptor for collagen I, a central node in ECM signal transduction, and a critical mediator of breast cancer progression in mouse and *in vitro* models [40]. Here, ITGB1 was upregulated by both cancer cell types in response to confining matrix conditions (Fig. 1.3 b). Thus, we next asked whether the network-forming phenotype observed in confining matrix conditions was

mediated by ITGB1. CRISPR-Cas9 technology was used to silence ITGB1 expression with single guide RNAs (sgRNAs), and constructs expressing sgRNAs targeting eGFP were used as controls (Fig. 1.6 a). Silenced and control cells were embedded separately and sparsely in low-density and high-density collagen matrices. Cells were monitored by time-lapse microscopy for early migration behavior then imaged again after one week. In low-density collagen, ITGB1-silenced cells maintained a similar level of migration capability to wild type (WT) cells in low-density matrices, but used an ameboid blebbing migration phenotype instead of a mesenchymal migration phenotype (Fig. 1.6b). In high-density conditions, ITGB1-silenced cells migrated faster than WT cells, but were significantly less persistent and did not invade (Fig. 1.6 c-e). Surprisingly, after 1 week ITGB1-silenced cells in high-density collagen-formed spheroid structures instead of cell networks, whereas control cells exhibited the same behavior as the WT in both collagen conditions (Fig. 1.6 f). Retrospective analysis of WT MDA-MB-231 cells in high-density collagen revealed that a small fraction spontaneously formed spheroid structures (Fig. 1.6g). These findings suggest that either basal expression level or upregulation of ITGB1 dictates the network-forming phenotype. To distinguish between these two possibilities, we next sorted the parental WT population based on basal ITGB1 expression level and then embedded high and low expressing cells separately in confining high-density collagen matrices (Fig. 1.6 h). We observed no appreciable differences in the percentage of networks versus spheroids formed by the sorted populations after one week. However, ITGB1 low cells proliferated less and displayed fewer total number of network or spheroid structures (Fig. 1.6i) even though the initial seeding density was the same (Supplementary Fig. 3a).

To further explore the link between the upregulated transcriptional module and the network-forming phenotype, we asked whether ITGB1-silenced spheroid-forming cells showed different gene expression patterns than WT network-forming cells. To assess this, we conducted qRT-PCR analysis of a subset of the 70-gene panel in the two cell phenotypes. Upregulation of several key genes were maintained in the spheroid-forming cells, whereas other genes were

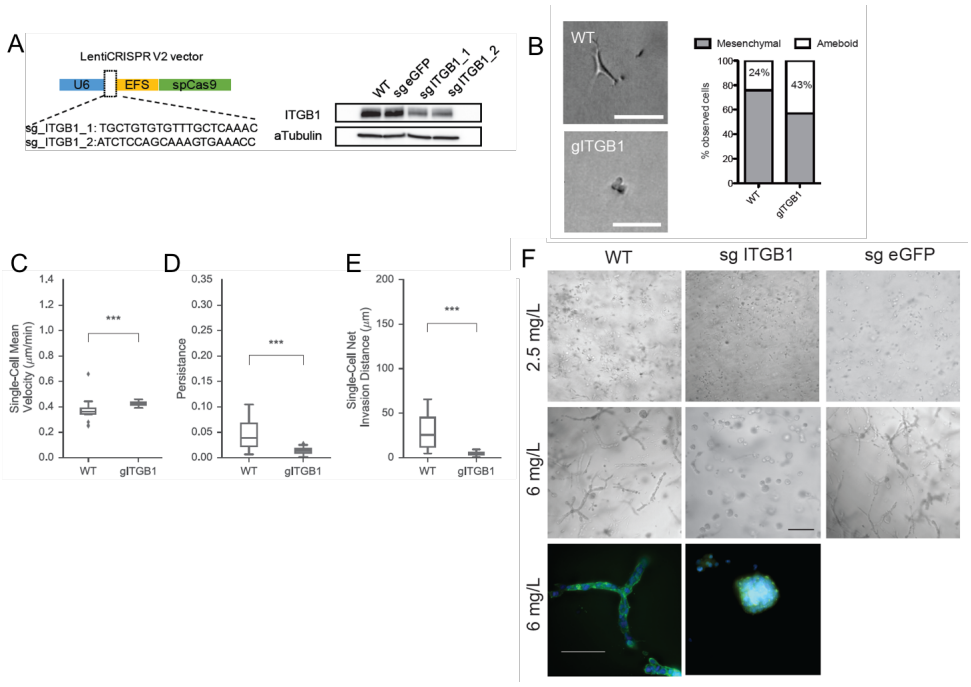

Figure 1.6: **Integrin-β1 upregulation is required for CINP a.** Schematic of lentiCRISPR V2 vector used for targeting ITGB1 gene and western blot validation of the protein depletion after 7 days of cell transduction. **b.** Comparison of MDA-MB-231 cells WT and ITGB1 depleted in low-density 3D collagen. Left: micrographs showing a representative image of a WT cell undergoing mesenchymal migration and an ITGB1-depleted cell undergoing ameboid migration. Right: quantification of mesenchymal vs. ameboid migration within the cell populations. **c.** Quantification of the effect of ITGB1 depletion on mean cell velocity when cells are cultured in 6 mgmL^{-1} collagen. **d.** Cell persistence and **e.** cell invasion distance. Comparison for c-e was performed using Mann-Whitney U test. **f.** MDA-MB-231 WT, ITGB1-depleted, and control sgRNA cell phenotypes after 7 days of culture in low-density collagen (top row) and high-density collagen (middle row). Scale bar 250μm. Bottom row shows high-magnification micrographs highlighting the difference between chain structures and spheroids. Scale bar 100μm.

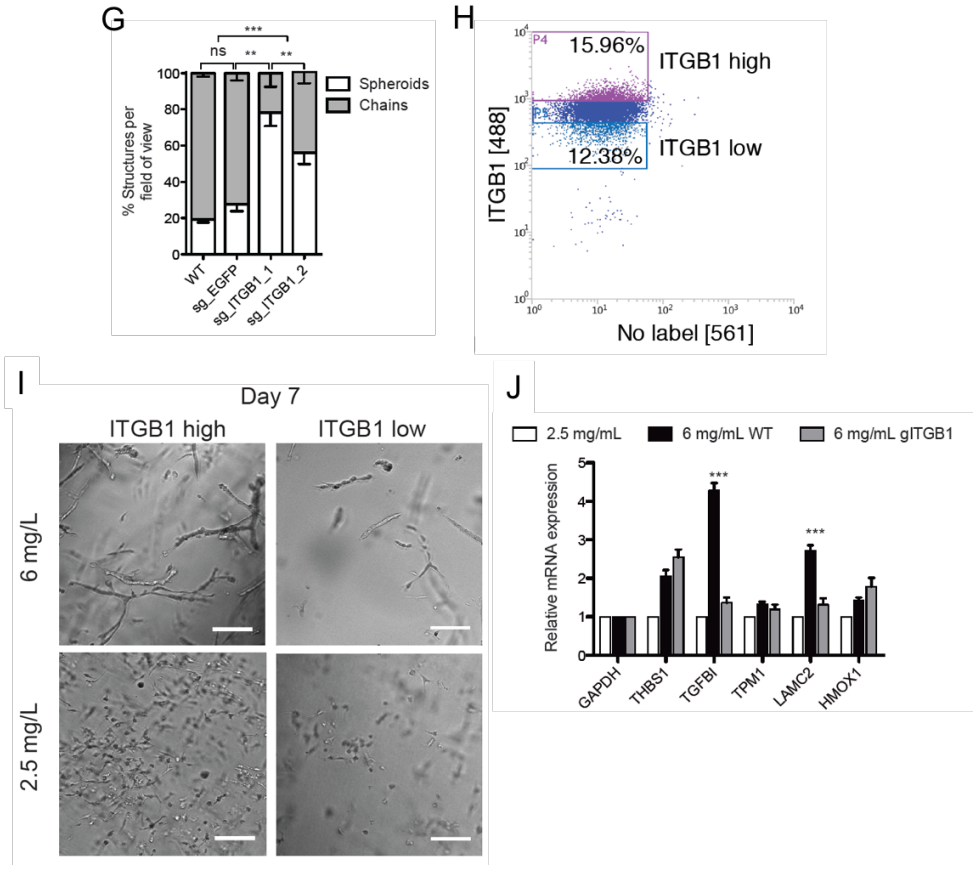

Figure 1.7: **Integrin-β1 upregulation is required for CINP g.** Quantification of proportional number of structures in each cell line when cultured in high-density collagen. **h.** Fluorescence-activated cells sorting (FACS) was used to separate the parental WT MD-MB-231 cell line population into high-ITGB1 and low-ITGB1 expressing populations. **i.** ITGB1 high and ITGB1 low cells after 7 days of culture in high-density 3D collagen (top row) and low-density (bottom row). Scale bar 200μm. **j.** RT-qPCR quantification of a small subset of genes identified in the 70-gene module in WT control- and ITGB1-silenced cells when cultured in low-density and high-density collagen. Data show mRNA levels relative to GAPDH and relative to low-density collagen level. Statistical significance evaluated between WT and gITGB1 groups, Statistical significance was determined by ANOVA test. Bar graphs represent mean±s.d. and data in box and whiskers plots is presented using Tukey method. n=3 biological replicates for all experiments unless otherwise noted. Significance is indicated as *, **, *** for $p<0.05$, $p<0.01$, $p<0.001$, respectively

no longer upregulated (Fig. 1.6j). These results show that ITGB1 regulates some aspects of the transcriptional module associated with the network-forming phenotype.

Finally, we asked whether upregulated genes in our transcriptional module that have previously been implicated as drivers of VM *in vitro* were functionally active in our network-forming phenotype. LAMC2 (Ln-5, gamma 2 chain) was previously found to be upregulated in aggressive melanoma cells that intrinsically display the VM phenotype compared to less aggressive melanoma cells that do not display VM. Moreover, it was implicated as a driver of VM network formation, since the cleavage of this secreted matrix molecule by MMP-2 and MT1-MM P produces pro-migratory fragments. In 2D culture of aggressive melanoma cells on top of collagen I, the inhibition of LAMC2 cleavage blocked VM network formation [41]. Using shRNA to knockdown LAMC2, we found that LAMC2 KD MDA-MB-231 cells maintain their ability to form network structures in 3D high-density collagen (Supplementary Fig. 3b, c). COL4A1 is another matrix molecule upregulated by cells undergoing the network phenotype (Figs. 1.2d and 1.4c) and previously implicated in driving migration [42]. COL4A1 KD in MDA-MB-231 cells also did not inhibit the ability of cells to form network structures in 3D high-density collagen (Supplementary Fig. 3b, c).

1.2.6 CINP transcriptional module predicts poor prognosis in human cancer

Finally, we sought to determine whether the CINP triggered by our 3D system was clinically relevant. To test this, we first asked whether the 70 common-to-cancer genes associated with the CINP could predict cancer patient prognosis. We anticipated that if this gene signature was indicative of a more metastatic cancer cell migration phenotype, its expression would correlate with poor patient outcomes. Since late stage tumors are already characterized by migration of tumor cells to distant lymph nodes or organs, we hypothesized that a gene signature associated with metastatic migration would correlate with prognosis in early (stage I and II) but not late

(stage III and IV) stage tumors. Using the cancer genome atlas (TCGA), we first analyzed data for breast cancer patients with respect to the expression of the 70-gene signature. An expression metagene was constructed using the loadings of the first principal component (CINP PC1) of a 195 Stage I patient by 70-gene matrix (Supplementary Fig. 4a, also see *Methods*). Then a survival analysis was conducted, comparing patients with the highest (top 30%) and lowest (bottom 30%) expression metagene scores by log-rank test. The cumulative survival rate of these two groups differed significantly (log-rank p=0.049); however, there was insufficient data to power a hazard ratio (HR) calculation (Fig. 1.7a). Analysis using the more data-rich METABRIC microarray database of breast cancer patients showed similar results for Stage I, confirming the prognostic value of the gene set (log-rank p=0.037, HR=1.40, Cox p=0.002, Fig. 1.7b). Applying the same analysis to stage II breast cancer patients revealed that the CINP metagene was associated with a marginally significant difference in 5-year survival by TCGA analysis but not by METABRIC analysis (Supplementary Fig. 4b, c). One caveat to this analysis is that data for 11 of the genes in our 70-gene panel were not available in the METABRIC dataset. The CINP metagene also did not separate patients with better prognosis in late stage tumors (Supplementary Fig. 4d). These results indicate that the CINP gene module could have clinical predictive power in the early stages of breast cancer. Importantly, further analysis of stage I patients by molecular subtype[43] revealed that the CINP metagene provided significant prognostic value for Luminal A and triple negative breast cancer patients (Table 1).

Next, we screened the predictive value of the gene module in additional cancer types in TCGA independently of stage or subtype using only age and CINP score as covariates. The CINP gene module was a significant predictor of survival in lung adenocarcinoma (LUAD), lower grade glioma (LGG), cervical squamous cell carcinoma and endocervical adenocarcinoma (CESC), pancreatic adenocarcinoma (PAAD), mesothelioma (MESO), adrenocortical carcinoma (ACC), bladder urothelial carcinoma (BLCA), and kidney chromophobe carcinoma (KICH) (Table 2),

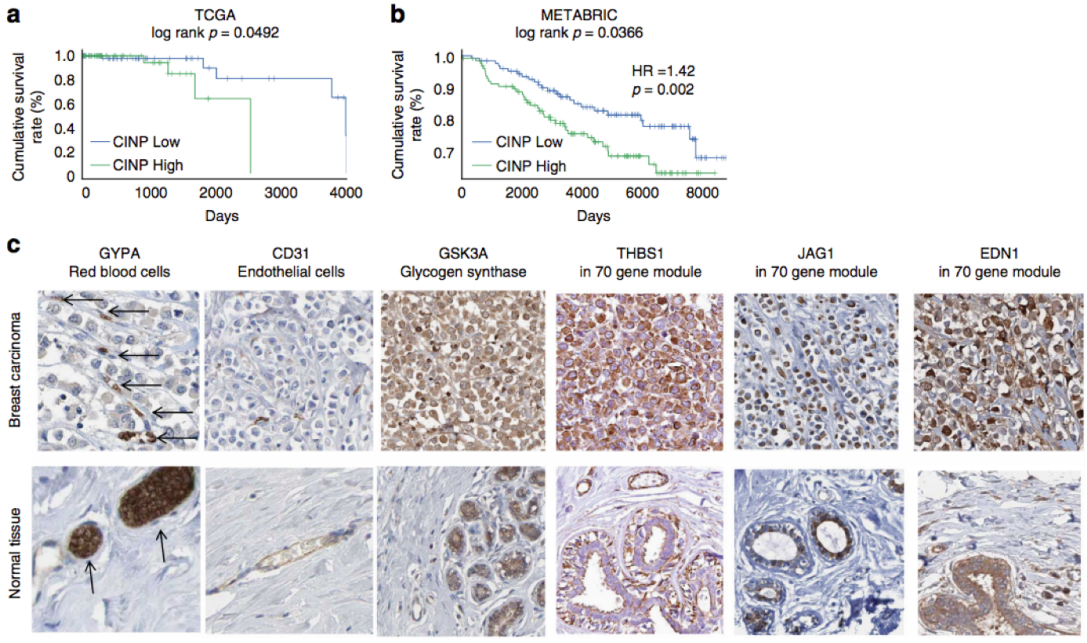

Figure 1.8: **The transcriptional response module associated with the collagen-induced network phenotype (CINP) is predictive of poor prognosis in human tumor datasets. a.** Kaplan-Meier survival analysis of stage I breast cancer patients from TCGA and **b.** METABRIC databases, when the PC1 loadings were used as an expression metagene. High CINP refers to the highest metagene expression scores and low CINP to the lowest expression scores. HR indicates hazard ratio. **c.** Sections of a primary breast carcinoma displaying the clinical VM phenotype of chain-like cell structures surrounded by a matrix network. Column 1: red blood cells, stained by an antibody against GYPA, are indicated by arrows. Several red blood cells are traversing the matrix surrounded by cancer cells. Column 2: tumor cells are negative for CD31 but in healthy tissue, stained regions colocalize to vessel structures. Column 3: tumor cells stain strongly for glycogen synthase, which likely contributes to the generation of a glycogen-rich matrix between the chains of cells. Columns 4-6: tumor cells undergoing VM stain strongly for three of the most upregulated genes in our 70-gene module. Image credit for **c.** Human Protein Atlas, patient ID 1910, available from www.proteinatlas.org [44]. See *Methods* for analysis details

but was not a significant predictor in several other tumor types found in TCGA (Supplementary Table 3).

Finally, we sought to determine whether the *in vitro* network-forming phenotype and associated transcriptional signature were related to the clinical VM phenotype. Using the Human Protein Atlas (www.proteinatlas.org)[44], we first identified breast cancer tumor slices displaying hallmarks of the VM phenotype, namely linear chains of cells lining glycogen-rich matrix

Table 1.1: Table1 CINP score potential to predict prognosis in stage I patients from metabric database broken down by molecular subtype

Metabric molecular subtype	Patient count	Death observed	HR	Cox p
Luminal B	126	33	1.2461	0.3194
Luminal A	202	34	1.5996	0.0162
Triple negative	63	14	3.8537	0.0070
HER2+	39	13	0.7152	0.3405

networks that conduct blood flow but do not stain positively for CD31 [12]. The tumor of patient 1910 displayed linear chains of cancer cells lining interconnected matrix networks (Fig. 1.7c). An immunohistochemical stain for GYPA showed red blood cells flowing through the matrix networks in tumor tissue but highly concentrated in vessel-like structures in healthy tissue. A stain against CD31 showed that there were no endothelial cells lining the matrix networks in the tumor tissues. Although a PAS stain was not available in the protein atlas database, which would determine whether the matrix networks were positive for glycogen, a stain against glycogen synthase (GSK3A) was available and showed that the chains of cancer cells significantly expressed this enzyme. The network-forming cell phenotypes combined with IHC evidence are consistent with the previously described histopathology of VM[12]. Next, we asked whether highly upregulated genes in our 70-gene CINP module were evident at the protein level in this clinical sample of VM. Stains for THBS1, JAG1, and EDN1 were available in the protein atlas database for the same tumor and showed significant expression of all three genes from our CINP transcriptional module in the VM tumor tissue but little stain in healthy tissues.

Table 1.2: Table 2 TCGA pan cancer analysis independent of stage

Cancer type	Patient count	Death observed	HR	Cox p
LGG	508	92	1.8434	1.1E-13
ACC	79	25	3.1863	2.8E-04
CESC	304	60	1.6560	5.2E-04
MESO	85	28	1.6101	6.9E-04
PAAD	178	59	1.5948	2.2E-03
BLCA	409	111	1.3338	0.0053
LUAD	521	124	1.2448	0.0169
KICH	64	8	2.9277	0.0210

1.3 Discussion

Our transcriptional, histopathologic, and phenotypic data suggest that the *in vitro* CINP and clinical VM share many commonalities. To our knowledge, this is the first time that collagen fiber architecture, characterized by short fibers and small pores, has been identified as an inducer of cancer transdifferentiation associated with a VM-like phenotype or more normal acinar phenotype, depending on the capacity of cells to upregulate ITGB1. More broadly, our findings show that collagen fiber architecture modulates the role ITGB1 plays in migration. In one architectural context, ITGB1 facilitates a switch from mesenchymal to ameboid migration and in another architectural context it mediates migration persistence and the shape of structures formed by collective morphogenesis.

Although ITGB1 was critical for directing the fate of cells during collagen-induced transdifferentiation, it was not necessary for initiating the transition from single cell to collective morphogenesis. Thus, it is not yet clear how cells sense the collagen architecture to initiate this process, but the response appears to be unique to stem-like cancer cells (MDA-MB-231 and HT-1080) as opposed to normal cells (HFF-1). Since, in our system, cells are embedded sparsely and undergo transcriptional reprogramming prior to cell division, the involvement of cell-cell interactions does not appear to have a role in transdifferentiation initiation. It is possible that cell

interactions with the unique matrix architecture involve matrix sequestration of soluble factors and autocrine signaling. Indeed, TGFβ pathways were implicated by GO enrichment analysis (Fig. 1.3b). Alternatively, the initial confinement and rounded geometry of the cells enforced by the matrix may play a role. Several studies support a role for cellular geometry in numerous cellular processes including gene expression and differentiation [45, 46, 47, 48, 49] some of which is mediated by RhoA and cytoskeletal tension. However, confinement in Matrigel did not trigger the same process, indicating a unique requirement for cell-collagen interaction. Future work will address these questions.

ECM molecules, COL4A1 and LAMC2, were also upregulated by CINP cells and have previously been implicated in driving migration and VM network formation in 2D culture [41, 42]. In our 3D collagen system, knockdown of either gene was not sufficient to block the VM-like phenotype (Supplementary Fig. 3). This suggests that regulation of *in vitro* cell network formation in a more physiological 3D culture context is distinct from regulation in a 2D culture context, which has implications for understanding molecular mechanisms. Given the significantly different requirements for cell movement in 3D ECM, such as matrix degradation and remodeling, our study highlights the importance of both the type of matrix and the dimensional context for studying physiological migration strategies. This echoes previous studies, which have shown that cell motility proteins function distinctly in a more physiologically relevant 3D context [19, 20, 21].

Interestingly, SERPINE1, a secreted protease inhibitor involved in coagulation and inflammation regulation, was upregulated by cancer cells as well as normal fibroblasts in response to confining collagen architectures. A recent study of cancer cell heterogeneity using mouse mammary carcinoma 4T1 cells and validated in human MDA-MB-231 breast cancer cells showed that cells which intrinsically expressed SERPINE family members were most efficient at spreading hematogenously, a characteristic that also correlated with their capacity to undergo VM *in vitro* [17]. Together, with our findings, this suggests that both cell-intrinsic and ECM factors may contribute to the emergence of VM. Interestingly, our finding that fibroblasts and cancer

cells both upregulate SERPINE1 expression in confining collagen conditions hints at a potential supporting role for stromal cells in SERPINE-mediated VM metastasis[17].

The significant predictive value of our CINP gene signature in several tumor types may signify the physiological relevance of the ECM context and network-forming migration phenotype we created *in vitro* to a conserved mechanism of solid tumor metastasis. It is possible that gene expression analysis of additional cancer cell types induced into VM-like behavior by our 3D collagen system could help to further refine the conserved CINP gene module. This would facilitate prioritization of the genes for targeted functional studies to identify key regulators and potential therapeutic targets. In addition to regulators of the CINP, the conserved gene module also likely contains elements responsive to collagen but not directly involved.

Profiling additional cancer cell types and patient-derived tumor cells could also help to refine the gene modules prognostic value in the nine tumor types already identified or define additional cancer-specific versions of the CINP. Validation of the prognostic value of this gene module could help patients avoid the long-term side effects of aggressive radiation and chemotherapy if the likelihood of metastasis is very low. A recent meta-analysis of histological VM in over 3000 patients with various solid tumor types found that the visual presence of this cancer phenotype is specifically associated with poor prognosis [50]. Molecular detection of VM markers could provide a more quantitative measure.

1.4 Methods

1.4.1 Cell culture

HT-1080 and HFF-1 were purchased from (ATCC, Manassas, VA) MDA-MB-231 cells were provided by Adam Engler (UCSD Bioengineering). All cell lines were cultured in high glucose Dulbecco's modified Eagle's medium supplemented with 10% (v/v) fetal bovine serum (FBS, Corning, Corning, NY) and 0.1% gentamicin (Gibco Thermofisher, Waltham, MA), and

maintained at 37°C and 5% CO2 in a humidified environment during culture and imaging. The cells were passaged every 2-3 days. Cell culture under hypoxia was done on a humidified and temperature controlled environment at 1% O_2. Cells were tested for mycoplasma contamination using the Mycoalert kit (Lonza, Basel, Switzerland) before performing experiments.

1.4.2 3D culture in collagen I matrix

Cells embedded in 3D collagen matrices were prepared by mixing cells suspended in culture medium and 10X reconstitution buffer, 1:1 (v/v), with soluble rat tail type I collagen in acetic acid (Corning, Corning, NY) to achieve the desired final concentration[19, 20]. A solution of 1M NaOH was used to normalize pH in a volume proportional to collagen required at each tested concentration (pH 7, 10-20μL 1M NaOH), and the mixture was placed in 48-well-culture plates and let polymerize at 37°C. Final gel volumes were 200μL.

1.4.3 Cell tracking and motility analysis

Cells were embedded in 3D collagen matrices in 48 well plates and left polymerize for 1?h in a standard tissue culture incubator and then 200μL of complete growth medium were added on top of the gels. The gels were transferred to a microscope stage top incubator and cells were imaged at low magnification (10x) every 2min for 48h. Coordinates of the cell location at each time frame were determined by tracking single cells using image recognition software (Metamorph/Metavue, Molecular Devices, Sunnyvale, CA). Tracking data were processed using custom written python scripts based on previously published scripts [51] to calculate cell speed, invasion distances, and mean-squared displacements (MSDs). For cell motility analysis before and after division the time-lapse videos were scanned to identify dividing cells within the imaging period and the division point was identified as the frame at which a clear separation could be identified between daughter cells. The dividing cell was tracked up to the division point and

one of the daughter cells (randomly chosen) was tracked from that point until the 48h time point. For collective cell invasion distance, the 48h time-lapse video was processed to obtain the maximum intensity projection (MIP), which highlights the tracks taken by the cells/groups of cells. Individual tracks distinguishable in the MIP were measured to obtain an equivalent invasion distance. All cell tracking data comes from three independent experiments performed on different days and with different cell passages.

1.4.4 Persistence random walk model implementation

To quantify the differences in the MSDs, we fitted the MSDs for each condition using the persistent random walk model (PRW model) as described in refs. [51, 52]. Briefly, the MSDs were calculated as in Eq. 1. The Eq. 2 describing the PWR was fitted using python's lmfit library for each MSD. The persistent time (parameter P) was then extracted to calculate differences between groups as presented in Fig. 1a, b.

$$MSD(\tau) = \langle (x(t+\tau) - x(t))^2 + (y(t+\tau) - y(t))^2 \rangle \tag{1.1}$$

where, x and y are the coordinates of the position of a cell at each time point and tau is the time lag.

$$MSD(\tau) = 2S^2P(\tau - P(1 - e^{-\frac{\tau}{P}})) + 4\sigma^2, \tag{1.2}$$

where, S is the cell speed and P is the persistence time and σ is a function of the error in the position of the cell as described in ref. [47].

1.4.5 Collagen stiffness modification and measurement using shear rheology

To modify the stiffness of collagen matrices without increasing density of material, we kept 2.5 mgmL^{-1} gels at 20°C for 30 min until they were fully polymerized. After the initial polymerization the gels were placed on a humidified tissue culture incubator at 37 °C for at least 1 hour extra before adding cell growth media on top. To measure the effect of polymerization temperature on the gel stiffness, we recreated the polymerization conditions for rheology testing (hybrid rheometer (DHR-2) from TA Instruments, New Castle, DE) using a cone and plate geometry with a sample volume of 0.6 mL. Shear storage modulus G' was measured as reported before[10]. Briefly, we first performed a strain sweep was from 0.1 to 100% strain at a frequency of 1 rad s^{-1} to determine the elastic region. Then a frequency sweep was performed at a strain within the linear region (0.8%) between 0.1 and 100 rad s^{-1}. Three independent replicates were performed for each condition tested.

1.4.6 Collagen structure modification using polyethylene glycol

To modify the structure of the collagen fibers within the gels without changing the final collagen concentration, Polyethylene glycol (PEG, MW=8000, Sigma, St. Louis, MO) was solubilized in phosphate-buffered solution (PBS), filter sterilized. Solubilized PEG was then mixed into the cells, reconstitution buffer solution described above to produce a final PEG concentration of 10 mgmL^{-1} in the collagen gel. The gels were allowed to polymerize in the same conditions as collagen only gels. Collagen structure modification was verified using confocal reflection microscopy.

1.4.7 RNA Isolation and purification

3D collagen I gels were seeded in three independent experiments and harvested after 24h of culture for RNA extraction and directly homogenized in Trizol reagent (Thermofisher, Waltham, MA). Total RNA was isolated following manufacturerx instructions. Isolated RNA was further purified using High Pure RNA Isolation Kit (ROCHE, Branford, CT). RNA integrity was verified using RNA Analysis ScreenTape (Agilent Technologies, La Jolla, CA) before sequencing.

1.4.8 RNA sequencing and data analysis

Biological triplicates of total RNA were prepared for sequencing using the TruSeq Stranded mRNA Sample Prep Kit (Illumina, San Diego, CA) and sequenced on the Illumina MiSeq platform at a depth of>25 million reads per sample. The read aligner Bowtie2 was used to build an index of the reference human genome hg19 UCSC and transcriptome. Paired-end reads were aligned to this index using Bowtie255 and streamed to eXpress [53] for transcript abundance quantification using command line "bowtie2 -a -p 10 -x /hg19 -1 reads_R1.fastq -2 reads_R2.fastq |express transcripts_hg19.fasta". For downstream analysis TPM was used as a measure of gene expression. A gene was considered detected if it had mean TPM>5.

1.4.9 Gene ontology term overrepresentation analysis

To assess the overrepresented GO terms the cytoscape app BiNGO[49] was used. Statistical test used was hypergeometric test, Benjamini-Hochberg false discovery rate (FDR) correction was used to account for multiple tests and the significance level was set at 0.05. For a given term, to assess the sensitivity of the enriched gene sets to the genes used in the analysis, we varied the threshold for including a gene as differentially upregulated from a fold change of 1.3 to a fold change of 1.9. The probability of a gene enriched with term is (# of genes in background with term)/(# of genes in background). The fold enrichment is the observed number of genes

associated with term divided by the expected number of genes associated with term.

1.4.10 Gene expression using qPCR

For qPCR experiments, RNA was extracted as stated above and cDNA was synthesized using superscript iii first-strand synthesis system (Thermofisher, Waltham, MA). Relative mRNA levels were quantified using predesigned TaqMan gene expression assays (Thermofisher, Waltham, MA). Relative expression was calculated using the DCt method using GAPDH as reference gene. Assays used were: GAPDH (Hs02758991_g1), HIF1A (Hs00153153_m1), THBS1 (Hs00962908_m1), TGFBI (Hs00932747_m1), TPM1 (Hs04398572_m1), LAMC2 (Hs01043717_m1), and HMOX1 (Hs01110250_m1).

1.4.11 Immunofluorescence and cell imaging

For cell imaging after 7 days of culture to visualize VM structures collagen gels were fixed using two washes of 4% PFA for 30 min each at room temperature. F-actin was stained using AlexaFluor® 488 Phalloidin (Cell signaling technology, Danver, MA) and the nuclei were counterstained with DAPI. For immunofluorescence staining the gels were incubated with the primary antibody for 48-72 h. Anti-COL4A1 (1:200 dilution, NB120-6586, Novus Biologicals).

1.4.12 Confocal reflection imaging and quantification

Confocal reflection images were acquired using a Leica SP5 confocal microscope (Buffalo Grove, IL) equipped with a HCX APO L 20X 1.0 water immersion objective. The sample was excited at 488 nm and reflected light was collected without an emission filter. For the estimation of pore size we used modification of a previously reported digital imaging processing technique[10]. Briefly, the images were normalized to account for uneven illumination effects. Then a threshold was applied to generate a binary mask where pores were identified as the darkest areas of the

image. Pore diameter was measured using NIS elements software (Nikon Instruments Inc., Melville, NY) measure objects tool.

1.4.13 Gene suppression

The lentiCRISPR v2 was a gift from Feng Zhang (Addgene plasmid #52961). We cloned small guide RNAs targeting the genes of interest into the lentiCRISPR v2 following Zhang's lab instructions. The sg_RNA sequences using were taken from the GECKO human library A [54]. Used sequences were: ITGB1 sg_RNA1 (5'-TGCTGTGTGTTTGCTCAAAC-3'), ITGB1 sg_RNA2 (5'-ATCTCCAGCAAAGTGAAACC-3'), EGFP sgRNA (5'-GGGCGAGGAGCTGTTCACCG-3'). The lentiCRISPR v2 vectors with the cloned desired sgRNA were sequence verified and viral particles were generated by transfecting into lentiX293T cells (Clonetech, Mountain View, CA. Cat #632180) along with packaging expressing plasmid (psPAX2, Addgene #12260) and envelope expressing plasmid (pMD2.G, Addgene #12259). Viral particles were collected at 48 h after transfection and they were purified by filtering through a 0.45 μm filter. Target cells were transduced with the viral particles in the presence of polybrene (Allele Biotechnology, San Diego, CA). After overnight incubation media was changed and cells were left 24-48h in normal growth media and then changed to puromycin selection media (2.5 μgmL^{-1} puromycin) for 7 days before experiments were performed. For shRNA-mediated gene knockdown, glycerol stocks of TRC2-pLKO.1-puro shRNA targeting LAMC2 (NM_005562.1-1019s1c1: CCGGGCTCACCAAGACTTACACATTCTCGAGAATGTGTAAGTCTTGGTGAGCTTTTTG), COL4A1 (NM_001845.3-3859s1c1:CCGGCCTGGGATTGATGGAGTTAAACTCGAGTTTAA CTCCATCAA TCCCAGGTTTTTG), and a non-targeting scramble sequence (SHC016:CCGGGCG CGATAGCGCTAATAATT TCTCGAGAAATTATT AGCGCTATCGCGCTTTTT) were purchased from Sigma-Aldrich packaged in LentiX293T (Clonetech, Mountain View, CA. Cat #632180) along with packaging expressing plasmid as described above. Lentiviral particles were transduced into target cells and stably expressing cells were selected with puromycin (2μgmL^{-1})

for at least 5 days before using.

1.4.14 Western blotting

Cells were grown to >90% confluency in 100 mm dishes. After washing 2X with PBS cells were collected into 100 μL of lysis buffer with 1X Halt protease inhibitor cocktail (Pierce IP lysis Buffer, Thermofisher, Waltham, MA) by thoroughly scraping the dish surface. Cell lysate was incubate in ice with constant shaking for 30 min and then centrifuged at 15,000Xg for 20 for protein purification. Samples were loaded at 50 μg total protein concentration for SDS-PAGE. Membranes were probed with antibodies against ITGB1 (#4706 from Cell signaling technology, Danver, MA. 1:10,000 dilution) and α-Tubulin (TU-01 MA1-19162, Thermofisher, Waltham, MA. 1:30,000 dilution).

1.4.15 Fluorescence-activated cell sorting

Wild type MDA-MB-231 cells were grown in collagen I-coated tissue culture dished until 80% confluence. Cells were harvested using HyClone HyQtase (GE Healthcare Life Sciences, Marlborough, MA) and resuspended in FACS buffer (1% BSA, 0.5 mM EDTA in PBS). The cell suspension was then labeled using a monoclonal antibody against human CD29 (β1 integrin) conjugated to AlexaFluor 488. A cell suspension without added antibody was used as negative control. After labeling, the cells were analyzed within 1 h of detachment at the stem cell core of Sanford Consortium of Regenerative Medicine (La Jolla, CA) using a BD Influx cell sorter (BD, Franklin lakes, NJ). Cells were sorted based on fluorescence intensity into the top-expressing population (15%, ITGB1 high) and bottom-expressing population (13%, ITGB1 low). Sorted cells were replated into collagen-coated dishes and left to recover overnight. After recovery, the cells were embedded in 3D collagen gels as described above.

1.4.16 Experimental data analysis and statistics

All cell motility data were analyzed for statistical significance using the Scipy Python package. Additional experimental data were analyzed using prism Graphpad (San Diego, CA). Significance is indicated as *, **, *** for $p<0.05$, $p<0.01$, $p<0.001$, respectively. Additional relevant information is detailed in the figure captions.

1.4.17 TCGA data reprocessing and survival analysis

The TCGA raw data were downloaded from CGHub directly using gtdownload [55]. Corresponding clinical metadata were obtained from the TCGA data portal (https://tcga-data.nci.nih.gov/docs/publications/tcga/). RNA-seq fastq files were realigned and quantified using sailfish v.0.7.6 [56] with default parameters. Only primary tumors were considered in our analysis. In the analysis of breast invasive carcinoma, only the patients with reported histological staining for the three markers (Her2, ER, PR) could be associated with a molecular subtype. Patients for which any of the histological markers were not evaluated or were detected at an equivocal level were assigned to an 'unknown' subtype. TCGA data for stage I, II, III, and IV breast cancer patients were analyzed by principal component analysis (PCA) with respect to the 70 CINP genes to construct gene expression meta-markers as previously described [57]. PCA-based score quantiles were mapped to CINP high and CINP low categories based on mean CINP gene expression levels. Because the CINP signature comprised only genes that were upregulated in the presence of the network phenotype, the overall mean expression of CINP genes was used to map PCA score to CINP signature activity level.

1.4.18 METABRIC data retrieval and survival analysis

We retrieved the clinical and microarray expression dataset from cBioPortal (http://www.cbiopor tal.org/study?id$\bar{b}$rca_metabric). We were able to map 59 out of 70 CINP genes to

METABRIC microarray data (missing genes: ZNF532, TRMT13, AMIGO2, KIN, NKX3-1, TANC2, TVP23C, SDHAP1, MTND2P28, GTF2IP4, H2BFS). Survival analysis was performed using the same method as described above for TCGA data. The Cox multiple regression uses CINP score, age, and three molecular subtype categories as covariates.

1.4.19 TCGA pan cancer analysis

Tumor types for which at least 100 patients had both expression and clinical metadata were analyzed to determine correlation between a CINP gene expression and 5-year survival. Only primary tumors were considered. Kaplan-Meier analysis was performed comparing the 30% of individuals with the lowest CINP expression score to the 30% with the highest score. The cox multiple regression uses age and CINP score as covariates. Both analyses use the Lifelines python library (https://lifelines.readthedocs.io/en/latest/). The log-rank test was used to determine significance of survival differences between groups.

1.4.20 Human Protein Atlas data

The online database Human Protein Atlas [44] was used to identify breast cancer tumor slices displaying hallmarks of the VM phenotype and subsequently assess protein expression of the genes associated with our *in vitro* network-forming phenotype. The tumor of patient ID 1910 was found to display linear chains of cancer cells lining interconnected matrix networks and had been stained for numerous other proteins of interest. Histological images shown in Fig. 1.7c can be found at www.proteinatlas.org by searching for the gene name in the breast cancer database and selecting patient ID 1910.

1.4.21 Code availability

Relevant scripts for the analysis of TCGA and METABRIC data are available at: https://github.com/brianyiktaktsui/Vascular_Mimicry.

1.4.22 Data availability

All sequencing data from this study has been deposited in the National Center for Biotechnology Information Gene Expression Omnibus (GEO) and is accessible through the GEO Series accession number GSE101209. All other relevant data are available within the article and supplementary files, or from the corresponding author upon request.

1.5 Supplementary material

1.5.1 Supplementary figures

1.6 Aknowledgments

This chapter is a partial reprint of ”3D collagen architecture induces a conserved migratory and transcriptional response linked to vasculogenic mimicry” as it appears on *Nature communications* 8, 1651 (2017). Velez, D.O., Tsui, B., Goshia, T., Chute, C., Han, A., Carter, H., Fraley, S. 3D collagen architecture induces a conserved migratory and transcriptional response linked to vasculogenic mimicry.. The dissertation author was the primary investigator and author of this paper.

We would like to acknowledge Kristen Jepsen and the IGM Genomics Core for assistance with RNA-seq experimentation, Christian Metallo for use of his hypoxia chamber, and Pedro Cabrales for use of his rheometer. The results shown here are in part based upon data generated

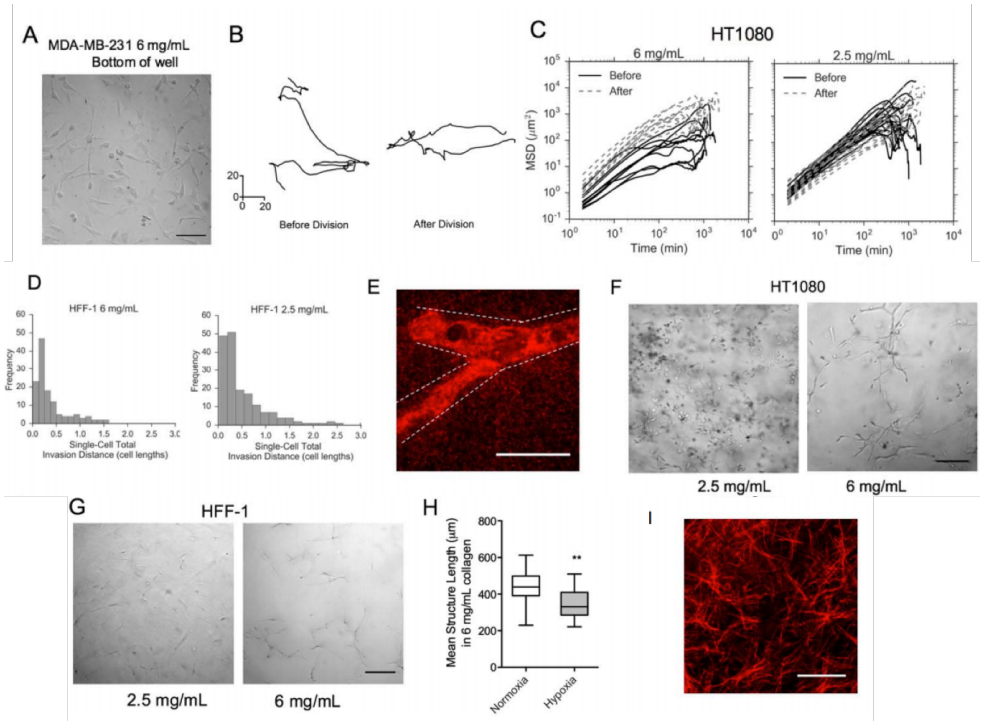

Figure 1.9: **Supplementary Figure 1 a.** Representative bright field image of MDA-MB-231 cells embedded in a 6 mg/mL collagen gel but in contact with the coverslip. Scale bar 100 μm **b.** Representative trajectories of cells cells embedded in a 6mg/mL collagen gel but in close contact with the coverslip before and after cell division. The trajectories show no appreciable differences between the cell movement before or after division.**c.** Mean Squared Displacement (MSD) and persistent time of HT-1080 cells before and after cell division for cells in low density and high density collagen. MSDs shown are 12 representative cell trajectories. **d.** Total invasion distance of single cells and their progeny for HFF-1 fibroblasts cells in 6mg/mL (left) and 2.5mg/mL (right) collagen gels in units of cell length (see methods) after 48 h of cellencapsulation. **e.** Representative confocal reflection image showing collagen fibers around a chain structure formed by MDA-MB-231 cells cultured in high density collagen gel for 7 days, dotted lines show the outline of the chain structure. Scale bar 100μm. **f.** Representative bright field images of HT-1080 cells after 7 days of culture in 2.5 mg/mL (left) and 6 mg/mL (right) collagen I matrix. Scale bar 250 μm. **g.** Representative bright field images of HFF-1 fibroblast cells after 7 days of culture in 2.5 mg/mL (left) and 6 mg/mL (right) collagen I matrix. Scale bar 250 μm. **h.** Mean structure length formed by MDA-MB231 cells cultured in high density 3D collagen after 7 days under normoxia (21% O2) or hypoxia (1% O2). Comparison was performed using Mann-Whitney U test. **i.** Representative confocal reflection image showing a 2.5mg/mL collagen gel polymerized at 20°C Scale bar 100 μm. Representative images of n=3 biological replicates for all experiments unless otherwise noted. Statistical significance is ndicated as *, **, *** for $p<0.05$, $p<0.01$, $p<0.001$, respectively.

by the TCGA Research Network: http://cancergenome.nih.gov/.

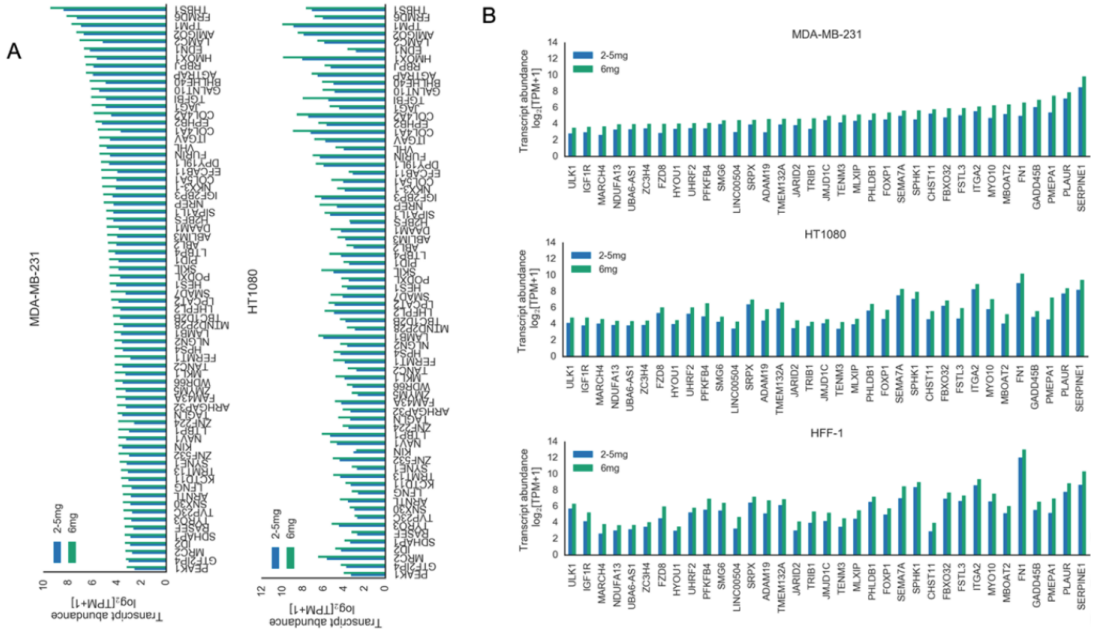

Figure 1.10: **Supplementary Figure 2 a.** Bar plot showing mean of n=3 expression values of the 70 genes upregulated by both cancer cell lines. MDA-MB-231 (top), genes sorted by low to high level of expression. HT1080 (bottom) gene order from top panel. **b.** Bar plot showing mean of n=3 expression values of the 35 genes upregulated by cancer cells and HFF-1 fibroblasts. MDA-MB-231 (top), genes sorted by low to high level of expression. HT1080 (middle) and HFF-1 (bottom) gene order from top panel

S.I.F. and lab members are supported by a Burroughs Wellcome Fund Career Award at the Scientific Interface 1012027, NSF CAREER Award 1651855, and UCSD CTRI, FISP, and AIM pilot grants. H.C. and lab members are supported by the NIH grant DP5-OD017937 and UCSD FISP grant.

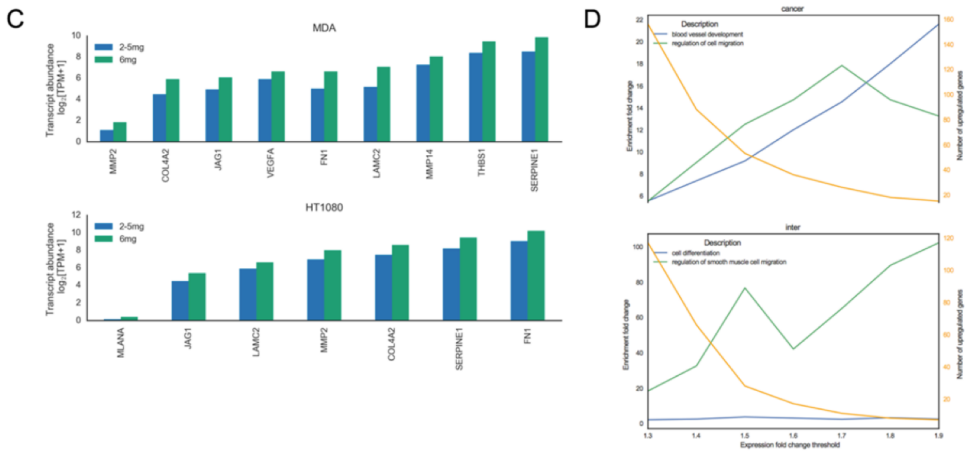

Figure 1.11: **Supplementary Figure 3 a.** Mean of n=3 expression levels of genes previously reported as being involved in vasculogenic mimicry and upregulated by cancer cells in high density collagen. For this panel TPM>5 was not required for analysis.**b.** Sensitivity analysis of Gene Ontology Analysis presented in Figure 2. Left Panel: Plot showing number of genes included in the analysis as a function of fold change threshold (yellow) and fold enrichment of 2 key terms (blood vessel development and regulation of cell migration, blue and green respectively) for the two gene sets cancer specific (70 Genes) and common to all cell lines analyzed (35 genes). Right panel shows the full sensitivity analysis when the fold change threshold is varied from 1.3 to 1.9. Details of the analysis can be found in the Methods section.

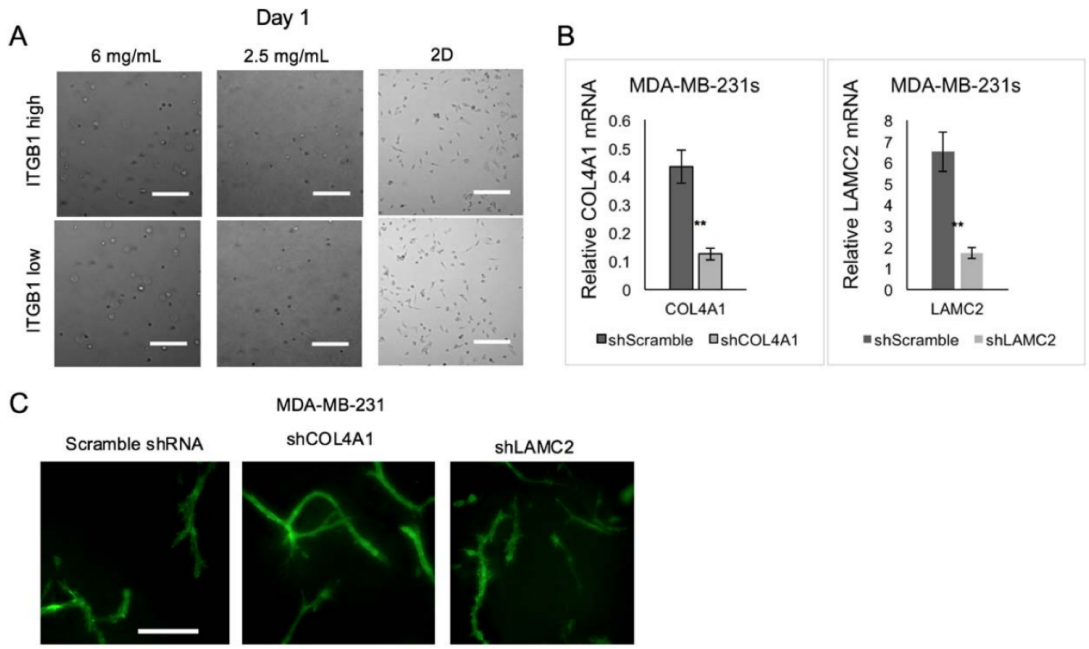

Figure 1.12: **Supplementary Figure 4 a.** ITGB1 sorted MDA-MB-231 cells at day 1 of embedding in high density and low density collagen matrices and plated on tissue culture plastic (2D). Scale bar 200 μm. **b.** RTqPCR validation of shRNA mediated knock down of LAMC2 and COL4A1**c.** Representative images of MDA-MB-231 cells expressing shRNA constructs against a scramble sequence, COL4A1, or LAMC2 after 7 days of culture in high density collagen Scale bar 200μm. N=3 biological replicates for all experiments unless otherwise noted. Statistical significance was determined by Wilcoxon rank sum test and is ndicated as *, **, *** for $p<0.05$, $p<0.01$, $p<0.001$, respectively.

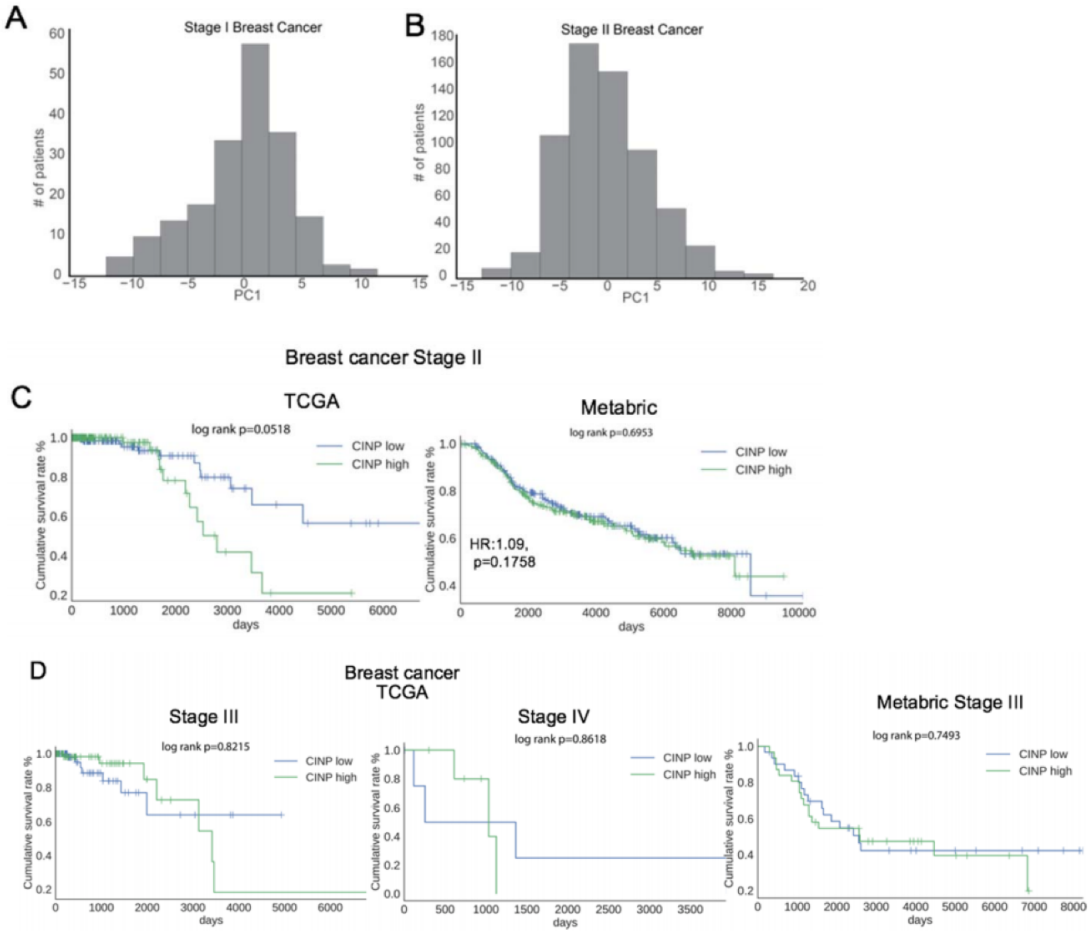

Figure 1.13: **Supplementary Figure 5 a.** Loadings of the first principal component (PC1) in stage I breast cancer patients of the 70 CINP associated genes identified in this study (Figure 1.2). **b.** Loadings of the first principal component (PC1) in stage II breast cancer patients of the 70 CINP associated genes identified in this study (Figure 1.2).**c.** Kaplan Meier survival analysis of stage II breast cancer patients in TCGA (left) and Metabric (right) databases when the PC1 loadings were used as an expression metagene. **d.** Kaplan Meier plots showing survival prediction by the CINP gene signature in Stage III and Stage IV breast cancer from TCGA data and stage III from metabric

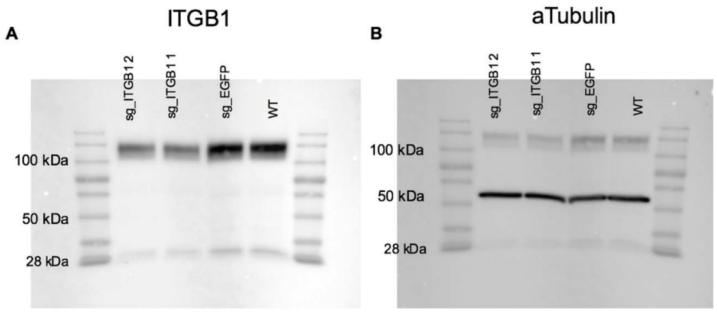

Figure 1.14: **Supplementary Figure 6** Uncropped Western blots from Figure 1.4A. **a.** Integrin B1 Western blot. **b.** Alpha tubulin western blot.

Chapter 2

Collagen architecture-induced metabolic and oxidative stress precede collective migration

2.1 Introduction

Collective cancer cell migration is thought to be the predominant means of metastatic dissemination in many solid human tumors[58, 59, 60]. In mouse models of cancer metastasis and in 3D *in vitro* tumor models, collectively migrating cells are typically more invasive and are resistant to chemotherapeutics[60, 61, 62, 63]. Improved mechanistic understanding of how collective migration is initiated may reveal novel strategies for metastasis treatment or prevention.

We and others have demonstrated that the fibrillar architecture of 3D collagen plays a unique role in inducing collective migration, independently of matrix stiffness and density[64, 65, 66, 67]. 3D collagen matrices characterized by short fibril architectures and small pores induce collective migration, both in spheroid and single cell culture models, whereas culture in Matrigel or on top of collagen or Matrigel does not induce collective migration. Importantly,

a conserved transcriptional state is associated with this collective migration phenotype and is clinically relevant to patient outcomes in nine human tumor types[66]. These findings provide translational incentive for further investigation as well as insight into the role of the extracellular matrix in initiating collective migration behaviors. However, it remains unclear how cancer cells sense and transduce these physical matrix cues. Here, we sought to address this knowledge gap by determining how distinct matrix architectures affect the four key biophysical processes involved in cell-matrix interactions: adhesion, cytoskeletal polymerization, contractility, and matrix remodeling.

By tuning the architecture of collagen without changing stiffness or density, we find that more confining architectures, i.e. shorter fibrils and smaller pores, are less susceptible to degradation by matrix metalloproteinases (MMPs). We show that cell-matrix adhesive coupling relies on matrix degradation, and low-degradability matrices force cells into a state of low adhesion, both biophysically and biochemically. The cellular response to this state is characterized by upregulation of protease activity, Notch signaling, and transition into collective migration. These findings suggest that the extracellular matrix may modulate the initiation of collective cell migration through loss-of-adhesion stress.

2.2 Results

2.2.1 3D collagen crosslinking is tuned by molecular crowding

To study the influence of matrix architecture on cellular behavior, we previously developed a collagen polymerization technique that allows us to modify fibril length and pore size of the network without altering matrix stiffness. Collagen fibril architecture is tuned independently of altering density and stiffness by molecular crowding with polyethylene glycol (PEG) during polymerization and cell embedding[66]. PEG, an inert crowding agent, is subsequently washed out of the polymerized matrix. Low density 2.5 mg/ml collagen polymerized in the presence of

10 mg/ml PEG crowding agent (P10) produces a more confining matrix architecture with short fibrils and small pores, which is similar to high density 6 mg/ml collagen matrices in terms of architecture but not mechanical properties (Figure 2.1a). Both MDA-MB-231 breast cancer and HT-1080 fibrosarcoma cells embedded sparsely in P10 or 6 mg/ml matrices undergo a migration transition characterized by rapid, persistent, invasive, and collective cell migration (Figure 2.1b)[66]. However, in 2.5 mg/ml matrices not crowded with PEG (P0), collagen forms long fibrils and large pores, and cells migrate individually in a persistent random-walk, mesenchymal migration mode.

Using reflection confocal imaging of these fibril architectures (Figure 2.1a) we verified that the differences between mesenchymal migration-inducing P0 and collective migration-inducing P10 and 6 mg/ml matrices were mainly in fiber length and pore size, i.e. confinement (Figure 2.1c-d). Since changes in fiber architecture could affect the mechanical properties of the matrices and thereby cellular behavior, we measured bulk as well as local matrix stiffness using shear rheology and atomic force microscopy (AFM), respectively (Figure 2.1e). We find that neither bulk nor local stiffness could explain the observed cell migration phenotype. Here, we use this model system to further study how cells sense and respond to matrix architecture.

2.2.2 Confining architectures reduce protrusion stability independently of actin dynamics

Cells interact with their surrounding matrix using four key biophysical processes: cytoskeletal polymerization, adhesion, contractility, and matrix remodeling. To study the effect of fibril architecture on these cell-matrix interactions, we first assessed protrusion and cytoskeletal dynamics. Time-lapse microscopy of GFP-expressing HT-1080 cells from 1-36h after embedding in collagen revealed that cells in more confining P10 and 6mg/ml matrices maintained a rounded shape for extended periods of time, as shown by cell circularity measured at 8h (Figure 2.2a) and by circularity measured as a function of time after 3D embedding (Supplementary Figure

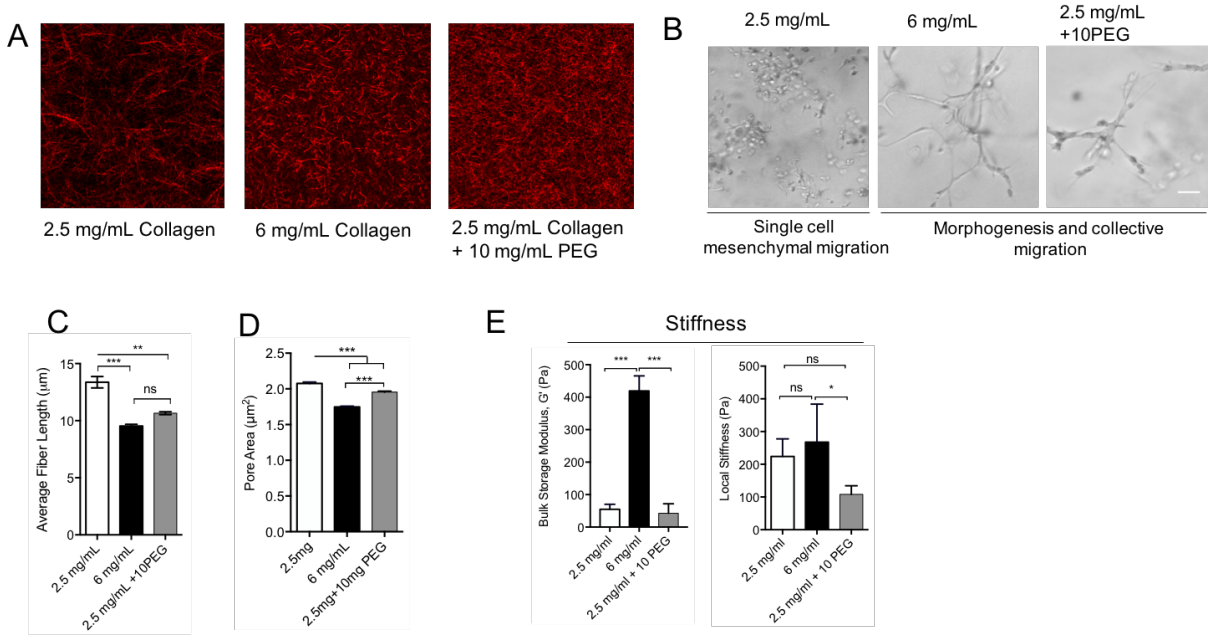

Figure 2.1: **3D collagen crosslinking is tuned by molecular crowding. a.** Confocal reflection images showing the fiber architecture of collagen matrices at 2.5 mg/mL (P0, characterized by low bulk collagen density and long fibers), 6mg/mL (characterized by high bulk collagen density and short fibers) and 2.5 mg/mL+10 mg/mL PEG (P10, characterized by low bulk collagen density and short fibers). **b.** Bright field micrographs of HT1080 cells cultured in collagen gels for 7 days, scale bar 50 μm.**b.** Quantification of mean fiber length in the 3 matrix conditions shown in A. **c.** Quantification of pore area in the 3 matrix conditions shown in A.**d.** Quantification of pore area in the 3 matrix conditions shown in A **e.** Stiffness of matrices of the 3 different conditions shown in A as measured by shear rheology (bulk stiffness, left panel) and Atomic force microscopy (AFM) (local stiffness, right panel). n=3 biological replicates for each experiment, statistical significance described as *, **, *** for $p<0.05$, $p<0.01$, $p<0.0001$ respectively

1a). On the other hand, cells in P0 matrices took on spindle-shaped mesenchymal morphology immediately after 3D collagen embedding (Supplementary Figure 1a-b). Cells in P10 and 6 mg/ml conditions also interacted with the matrix using shorter-lived and smaller protrusions than in the P0 matrices (Figure 2.2b and c). In the P0 matrix, where fibril lengths averaged 13.5 μm, protrusions extended to 31.4μm and lasted for 46 min on average. On the other hand, in P10 and 6 mg/ml matrices having average fibril lengths of 9.5 and 10 μm respectively, protrusions extended to 15.7 and 13.7 μm and lasted 19 and 16 min on average. No statistically significant differences were observed between cells in P10 and 6 mg/ml conditions.

To assess cytoskeletal dynamics, we performed fluorescence recovery after photo bleaching (FRAP) on the protrusions of HT-1080 cells expressing fluorescent Actin (Dendra2-LifeAct). We detected no significant differences in the fluorescence recovery time between the P0, P10, and 6 mg/ml matrix conditions (Figure 2.2d), suggesting that differences actin polymerization processes could not explain the observed differences in cell protrusion dynamics. Collectively, these results suggest that more highly confining matrix architectures influence cell shape and protrusion dynamics independently of actin dynamics, matrix stiffness, or bulk collagen density.

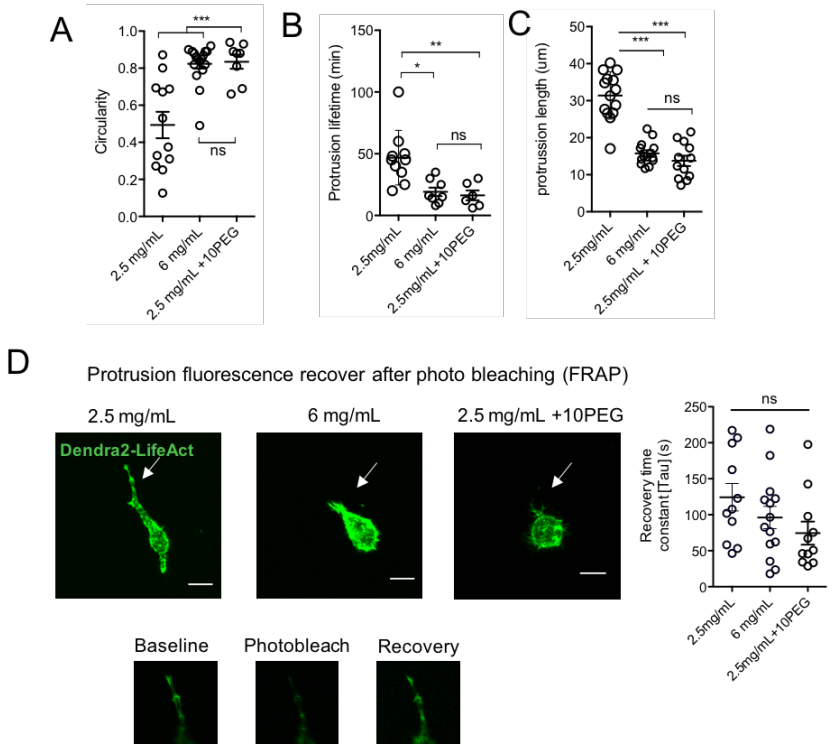

Figure 2.2: **Confining architectures reduce protrusion stability independently of actin dynamic. a.** Circularity of cells embedded in the 3 matrix conditions at 8 hours after seeding **b.** Protrusion lifetime and **c.** length for cells embedded in the 3 matrix conditions. **d.** Fluorescence recovery after photo bleaching (FRAP) analysis of actin dynamics in cellular protrusions in the 3 described matrix conditions. Scale bar 25 μm. n=3 biological replicates for each experiment, statistical significance described as *, *, ** for $p<0.05$, $p<00.01$, $p<0.0001$ respectively.

2.2.3 Confining matrix architectures destabilize cell adhesion

Since we observed small and short-lived protrusions in P10 and 6 mg/ml architectures where cells remained rounded, we hypothesized that these protrusions were less stable in their adhesion to and contraction of the matrix. Simultaneous confocal reflection imaging of collagen fibrils and the cell?s actin cytoskeleton in the P10 and 6 mg/ml conditions showed that cells were primarily moving without causing large matrix deformations. On the other hand, cells in the P0 condition showed significant pulling and displacement of fibrils (Supplementary Figure 1b).

To quantitatively assess the ability of cells to adhere to and contract the matrix, we embedded GFP+-HT-1080 cells in each matrix condition along with carboxylated fluorescent microspheres, which covalently bind to collagen fibrils and allow for high resolution, time-resolved tracking of cell traction by simultaneously monitoring bead and cell movements (Figure 2.3a, Supplementary Figure 1c and Methods). Quantification of the maximum bead displacement (Supplementary Figure 1d) by cells in each condition revealed a significant decrease in matrix deformation in the P10 and 6 mg/ml matrices compared to the P0 condition (Figure 2.3b).

Further detailed analysis of protrusion and matrix movement revealed that in the P0 architecture, cellular protrusions pull on the matrix as they near a maximum extension length, producing large bead displacements with little protrusion extension or retraction (See Methods and Supplementary Figure 2 and 3). This phenotype is characterized by high matrix pulling even when the cell's protrusion displays little local movement and is not visually translocating (Figure 2.3c). However, cells in the more confining P10 and 6 mg/ml matrices erratically push, pull, and lose attachment to the matrix as their short-lived protrusions probe the surroundings (Figure 2.3d). Additionally, we observed that a fraction of the cells in the P10 and 6 mg/ml collagen matrices exhibited a 'tumbling' phenotype, characterized by rapid cell movement without detectable bead movement around them (Figure 2.4a), as opposed to the well-defined protrusion associated deformations observed in P0 matrices . This suggested that cells remained contractile, but adhesion was reduced.

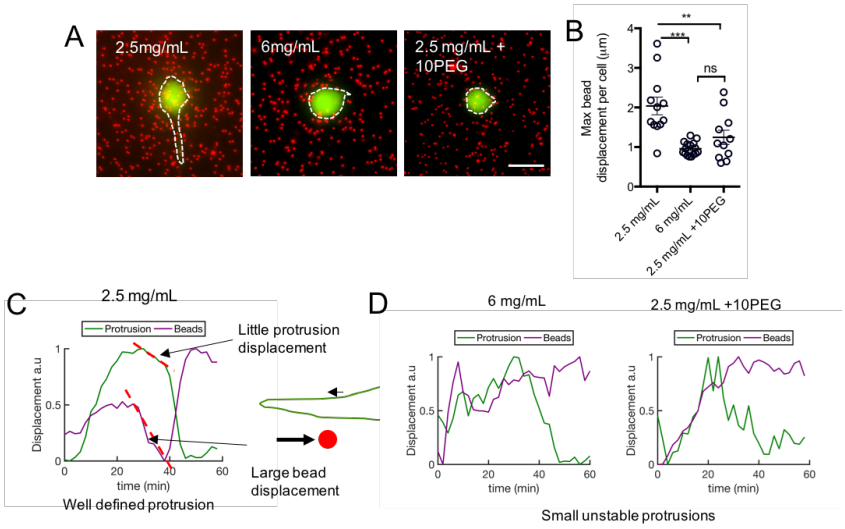

Figure 2.3: **Confining architectures limit cell interactions with matrix. a.** Representative maximum intensity projection fluorescent micrographs of GFP+ cells embedded in 3D collagen matrices containing fluorescent microbeads. Scale bar 25 μm **b.** Average max bead displacement around cells in the 3 different matrix architectures. **c.** Min max normalized data for protrusion extension- retraction and mean trajectory of the top 25% moving beads overlaid in a single plot highlights the pulling phenotype, where with little protrusion displacement a large deformation is caused in the matrix in 2.5 mg/mL matrix and. **d.** Min max normalized overlaid plots for the more confining 6 mg/mL and 2.5 mg/mL +10PEG matrix conditions showing no clear pattern of pulling by the cells.

To quantitatively characterize cell adhesion to the matrix, we simultaneously calculated the instantaneous velocity of the cells and instantaneous velocity of the beads adjacent to each cell. Cells well-coupled to the matrix are expected to produce bead movements roughly equivalent to the movement of the cell body. In contrast, beads around weakly adhered cells are expected to move at lower instantaneous rate than the cell body. Using this logic, we calculated the cell slip ratio as the ratio between the instantaneous velocity of cell body and the instantaneous velocity of the surrounding beads (Supplementary Figure 1e). We observed a significantly higher slip ratio (slip ratio$>$1) for cells embedded in P10 and 6 mg/ml matrices compared to cells in P0 (Figure 2.4b). In P0 matrices, cells are well coupled to the matrix (slip ratio$\sim$1) or occasionally exhibited tread-milling on the matrix (slip ratio$<$1), where matrix was pulled along the cell body. Analyzed cells in all conditions showed similar levels of local movement (Supplementary Figure

1f), suggesting that cells in more confining matrix architectures have similar contractility but low adhesion to the collagen.

Based on these observations, we hypothesized that cells are unable to stabilize adhesions in the more confining P10 and 6 mg/ml matrix architectures. This, in turn, would be expected to lower the amount of activated focal adhesion kinase (FAK) in the cells. Western blot analysis of phosphorylated FAK at tyrosine residue 397 (pFAK) showed a decrease in pFAK in cells embedded in the more confining matrices (Figure 2.4c). As a control, we compared this to pFAK levels in cells grown in non-adherent plates, which showed a significant decrease to almost undetectable levels, as has been previously reported[68, 69]. This suggests that more confining matrix architectures alter protrusion dynamics by reducing, but not eliminating, cell adhesion to the matrix.

Non-adherent culture conditions are known to induce metabolic and oxidative stress[70, 71]. Since cells in confining matrices maintained a low level of adhesion and pFAK, we sought to determine the extent to which they experience low-adhesion stress. Phosphorylated FAK is an important negative regulator of Tuberous Sclerosis Complex 2 (TSC2)[72], which in turn negatively regulates the mammalian target of rapamycin (mTOR) pathway. It has been shown that decreased pFAK can lead to increased TSC2 activity, which downregulates key mTOR target genes related to glycolysis, phosphate pentose pathway, and lipid biosynthesis pathways[73, 74]. Thus, we asked if the reduced levels of pFAK we observed in confining collagen matrices impacted this pathway. Analysis of RNA sequencing data revealed that mTOR target genes were largely downregulated in cells in more confining matrix conditions, consistent with their low levels of pFAK (Figure 2.4d). Further gene set enrichment analysis also revealed a decrease in the enrichment of TCA cycle and pyruvate metabolism pathways (Figure 2.4e) for cells growing in 6mg/mL matrices compared to P0.

Loss of attachment to ECM has also been shown to reduce glucose and glutamine uptake and promote accumulation of reactive oxygen species (ROS)[70, 71, 75]. To further explore the

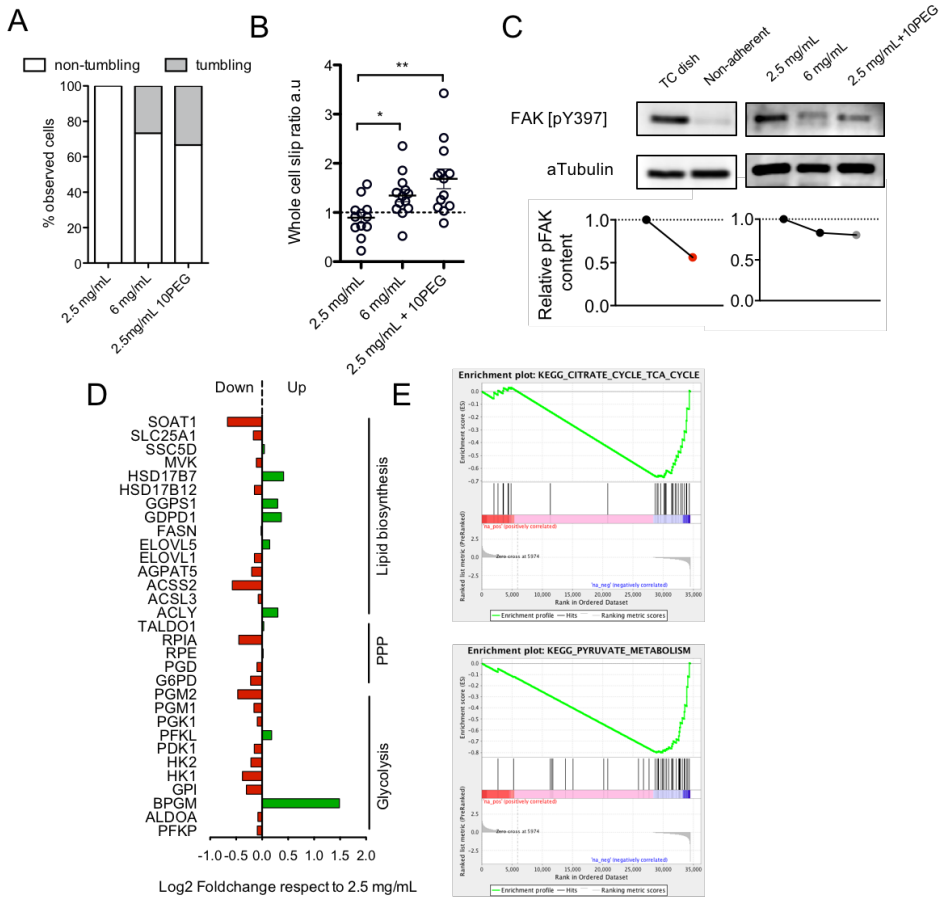

Figure 2.4: **Confining matrix architectures destabilize cell adhesion a.** Quantification of number of observed cells showing a tumbling phenotype in the different matrix architectures **b.** Whole cell slip ratio quantified from traction force microscopy data and single cell tracking (see methods). **c.** Western blot analysis of phosphorylated focal adhesion kinase (FAK) of cells cultured on 2D tissue culture treated dishes (lane 1), low attachment plates (lane 2), and the three collagen matrix architectures (lanes 3-5). **d.** Gene expression changes between culture in P0 and 6mgmL-1 matrices as measured by RNASeq for genes previously reported to be target of the mTOR pathway and critical mediators of cellular metabolism. **e.** Gene set enrichment analysis (GSEA) showing a reduced enrichment for genes of the TCA cycle and pyruvate metabolism pathways. n=3 biological replicates for each experiment, statistical significance described as *, *, ** for $p<0.05$, $p<00.01$, $p<0.0001$ respectively.

parallels between how cells experience confining collagen compared to anchorage-independent growth, we asked whether cellular ROS levels were elevated to similar extents in both environments. ROS levels were measured after 8 hours of 3D embedding and quantified by the mitochondrial superoxide sensitive dye MitoSOX. We observed that cells in P10 and 6 mg/ml ma-

trices displayed higher ROS levels than cells in P0 (Figure 2.5a). This increase was also observed in cells grown in non-adherent plates compared to traditional tissue culture plates (Supplementary Figure 4a) and was also detectable with the ROS sensitive dye cellROX (Supplementary Figure 4b). Additionally, measurement of glucose consumption and lactate production by cells at 24 h after collagen embedding revealed reduced glycolytic activity in the highly confining matrices (6mg/mL and P10) compared to non-confining matrices (P0). Cells consumed 10-20 % less glucose and secreted 10-20% less lactate in confining matrices than in low confining matrices. This biochemical state resembled that of cells cultured in non-adherent plates (Supplementary Figure 4c-d). Glutamine uptake was also reduced in confining matrices (15-20% lower) as well as in cells in non-adherent plates (40% lower) (Supplementary Figure 5a). Quantification of cell division within the 24 hr measurement time window showed a slight decrease in cell divisions in 6 mg/mL, but no statistically significant differences across the conditions (Supplementary Figure 5b). This confirms that the observed differences in glycolytic activity are not due to differences in proliferation rates at this time point. Taken together, these data indicate that confining collagen architectures are weakly-adhesive and induce metabolic changes in cells similar to that of anchorage-independent growth, which promotes downregulation of mTOR pathway target genes and a state of oxidative and metabolic stress.

2.2.4 Cell adhesion is regulated by matrix degradation

To test whether this reduction in adhesion was due to the fiber topology alone or was a function of culture dimensionality, we seeded cells on top of P0, P10, and 6 mg/ml matrices. We analyzed the state of FAK phosphorylation at 30 and 60 minutes after seeding using western blotting. We only observed an increase in pFAK at 60 minutes for cells on top of the P0 matrix (Figure 2.5b). Cells on top of P10 and 6 mg/ml matrices maintained a low level of pFAK, as was observed for cells fully embedded in these matrices.

Previous reports have shown that matrix crosslinking (i.e. smaller pores and shorter

fibers, i.e. confining architectures) can be associated with a reduction in matrix degradability[76]. Using an *in vitro* assay of collagen degradation with purified recombinant human MMP-8 (Supplementary Figure 5c), we found that the more confining P10 and 6 mg/ml matrices were significantly more resistant to degradation than the P0 matrix (Figure 2.5c). As a control, we measured the diffusivity of molecular weight-matched fluorescent dextran and found no significant differences among the different collagen architectures (Supplementary Figure 7).

We next hypothesized that matrix degradability could modulate the ability of cells to create stable adhesions to the matrix. If this were the case, then inhibition of MMP activity would be expected to decrease cell adhesion. To test this, we embedded GFP+ HT-1080 cells in bead-laden matrices with the addition of a broad-spectrum MMP inhibitor (Marimastat) and measured the cell slip ratio as described above. MMP inhibition significantly increased cell slip across all matrix conditions (Figure 2.5d-f), indicating that matrix degradation activity is required for effective cell adhesion.

To test if the requirement for MMP activity in adhesion is dimensionality dependent, we repeated the experiment where we cultured the cells on top of the P0 matrix condition and measured pFAK, but this time including Marimastat treatment. MMP inhibition repressed pFAK recovery at 60 min post seeding compared to control conditions (Figure 2.5g) suggesting that MMP activity was also necessary for proper cell-ECM attachment in 2D conditions.

2.2.5 Cells upregulate proteases and Notch signaling in response to low attachment in confining architectures

Since MMP activity is required for successful cell-ECM coupling (Figure 2.5d-f), and cells in confining matrices eventually migrate to form collective networks (Figure 2.1b), we hypothesized that cells may upregulate proteolytic activity as a means of overcoming their low-adhesion state. Gene expression analysis of cells cultured in 6 mg/ml versus P0 matrices at 24 h after embedding showed significant increased expression of MMP-1, -2, and -14 (Figure

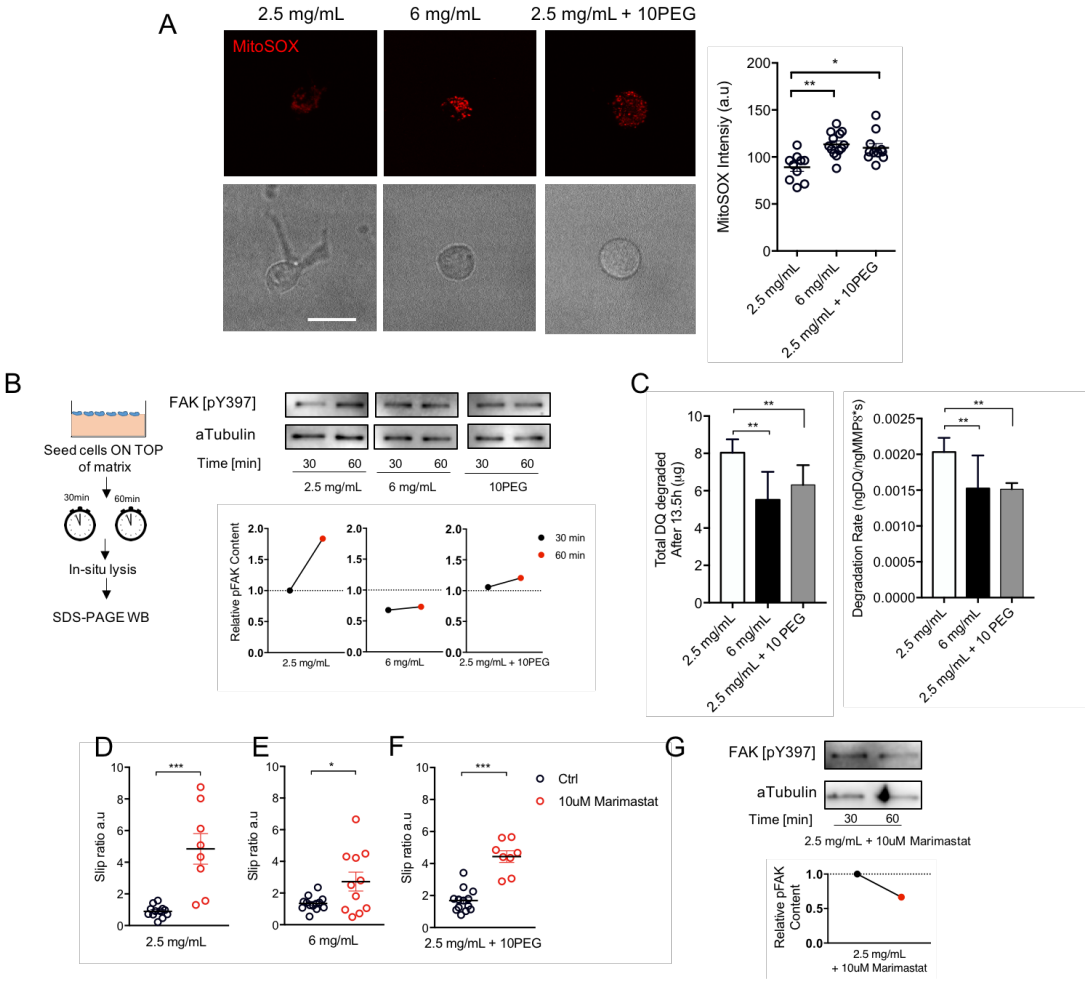

Figure 2.5: **Cell adhesion is regulated by matrix degradation a.** Mitochondrial superoxide levels as measured by MitoSOX intensity from confocal microscopy for cells growing in P0 ,6mgmL-1 and P10 matrices, scale bar 25μm. **b.** .(left) Schematic representation of the steps followed to analyze FAK phosphorylation for cells cultured on top of collagen matrices. (right) Western blot analysis of phospho FAK for cells cultured for 30 or 60 minutes on top of P0, 6 mg/mL and P10 matrices. **c.** Degradability of the 3D collagen matrices of the 3 conditions presented as measured by DQ collagen fluorescence per unit time after the addition of purified recombinant human MMP8. **d.** Slip ratio analysis for cells cultured in the presence of 10μM marimastat in 2.5mg/mL. **e.** 6 mg/mL and **f.** 2.5mg/mL +10PEG matrices. **g.** Western blot analysis of phospho FAK for cells cultured for 30 or 60 minutes on top of a 2.5mg/mL matrix with the MMP inhibitor Marimastat. Western blot images and quantifications are representative of n=1 experiments. n=>3 biological replicates for each experiment, statistical significance described as *, **, *** for p<0.05, p<00.01, p<0.001 respectively.

2.6a). To assess whether this transcriptional program was functional, we used dye quenched (DQ) collagen to measure pericellular matrix degradation patterns. DQ collagen emits strong green

fluorescence when fibrils are cleaved and the attached fluorescein dye is no longer quenched[77]. Confocal imaging of the DQ collagen fluorescent signal 24 hours after 3D embedding revealed a significant increase in collagen degradation surrounding cells in confining architectures (Figure 2.6b-c). Very little collagen degradation was observed in P0 matrices (Figure 2.6b-d), and no significant difference was observed between the DQ collagen intensity around the cell body versus protrusions (Supplementary Figure 6b).

Surprisingly, cells in confining matrices accumulated the fluorescent cleaved collagen in their cytoplasm (Figure 2.6b, white arrows), suggesting increased collagen internalization. Internalization of fluorescent collagen was completely absent during the first few hours of cell-ECM interaction (Supplementary Figure 6a), suggesting internalization was an active process. High resolution z-stack imaging confirmed the intracellular localization of the internalized collagen (Figure 2.6d). This phenomenon was significantly more prevalent in cells cultured in the more confining P10 and 6 mg/ml matrices (Figure 2.6e) compared to P0. Interestingly, gene expression analysis identified upregulation and significant enrichment of genes involved in collagen catabolic processes (23.8 fold enrichment, p=3x10-6) in cells embedded in confining matrices. Included in this set was MRC2, a gene encoding for Endo180, which is the main collagen endocytic receptor responsible for the internalization of degraded collagen[78, 79]. Using qRT-PCR, we also found that this gene is upregulated by cells growing in non-adherent plates (Figure 2.6f). However, these cells do not have access to extracellular collagen.

Genes in the Notch signaling pathway were also upregulated and significantly enriched (26.52-fold enrichment, p=0.03) by cells in confining matrices, including the Notch ligand JAG1, the transcription factor RBPJ, and Notch target genes HES1 and HEY1 (Figure 2.6g)[80].

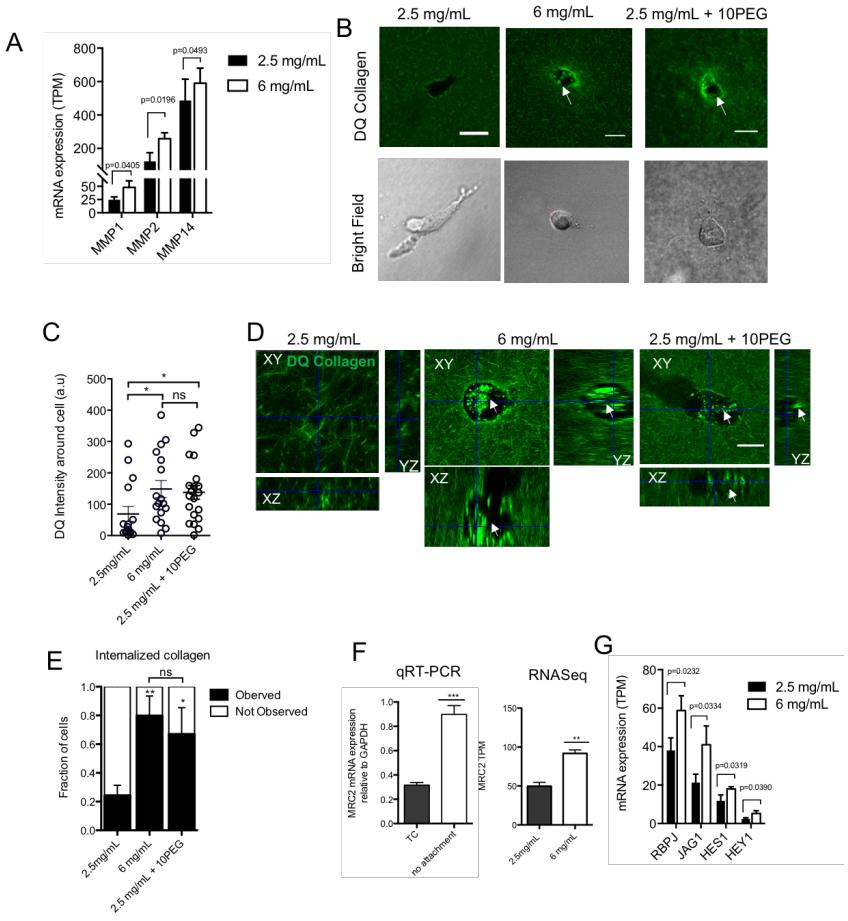

Figure 2.6: **Cells upregulate proteases and Notch signaling in response to low attachment in confining architectures a.** MMP gene expression changes between culture in P0 and 6mgmL-1 as measured by RNASeq. **b.** Fluorescent micrographs showing HT1080 cells embedded in collagen type I matrices containing 100 ug/mL DQ-collagen type I (top row), white arrows point to areas around the cells with increased DQ collagen intensity, and respective bright field images (bottom row), scale bar 25 μm. **c.** Quantification of DQ intensity around cells cultured in the three different collagen architectures. **d.** Representative confocal Zstacks showing degraded collagen fragments internalized by cells (white arrows) growing in short fiber architectures (6 mg/mL and 2.5 mg/mL+10PEG) but not in long fiber 2.5mgmL-1 matrix, scale bar 15 μm. **e.** Quantification of the fraction of cells where internalized collaged was observed F. qRT-PCR quantification of MRC2 expression in cells growing on tissue culture plates (TC) versus cells growing in low attachment plates (left) and RNASeq data showing transcript abundance for MRC2 for cells growing in 2.5mgmL-1 and 6mgmL-1 collagen matrices (right). **f.** qRT-PCR quantification of MRC2 expression in cells growing on tissue culture plates (TC) versus cells growing in low attachment plates (left) and RNASeq data showing transcript abundance for MRC2 for cells growing in 2.5mgmL-1 and 6mgmL-1 collagen matrices (right). **g.** Gene expression changes between culture in P0 and 6mgmL-1 for genes associated with NOTCH pathway as measured by RNASeq. . n=¿3 biological replicates for each experiment, statistical significance described as *, **, *** for p<0.05, p<00.01, p<0.001 respectively.

2.3 Discussion

Our study reveals that changes in the fibrillar architecture of collagen, independent of stiffness or density, influence cell-ECM adhesive coupling. Fiber architectures that are more crosslinked and confining, i.e. smaller pores and shorter fibers, reduce cell adhesion and cause cells to exhibit hallmarks of anchorage-independent growth despite being surrounded by matrix. This results in reduced glycolytic activity and increased oxidative stress, which mimics stress induced by suspension culture or growth on non-adherent plates[70, 74]. Subsequent upregulation of genes involved in collagen catabolism, in combination with increased collagen degradation and internalization in 3D confining collagen, suggests that an endocytic pathway may play a role in overcoming oxidative and glycolytic stress associated with a 3D low-adhesion state. Interestingly, recent studies have shown that collagen internalization is upregulated in nutrient-starved cells, where collagen-derived proline is used as a substitute to fuel the TCA cycle and maintain cell survival[81]. Similarly, it has been shown that macro pinocytosis of proteins can be used as an amino acid supply by transformed cells[81, 82]. Symptoms of limited nutrient availability also include upregulation of MMPs[83, 84] and MRC2[81], alluding to the possibility that low adhesion and nutrient deprivation stress responses may be linked.

Collagen matrices with small pore sizes have previously been found to drive collective cell migration behavior and the upregulation of MMPs due to biophysical confinement and restriction of the nucleus[65, 85, 86]. However, matrix degradability and cell adhesion were not assessed in these earlier studies. Our study shows that a major difference in how cells interact with confining matrices is that they are unable to stabilize adhesions, which leads to oxidative stress, and oxidative stress has previously been linked to the upregulation of MMPs through NF-kB[87, 88, 89, 90]. However, further study is needed to determine if NF-kB is activated in this system. We also show that the Notch pathway is upregulated by cells in confining collagen. This pathway is implicated in regulating collective migration by differentiating leader versus stalk cell phenotypes in normal

tissue development and in tumor growth and metastatic invasion[60, 91, 92, 93, 94]. There is evidence for NF-kB crosstalk with Notch[95] and Notch regulation by ROS[96, 97],but further examination in the context of collective cancer cell migration is necessary.

We also demonstrate that matrix degradation activity is required for efficient adhesion in all of the 3D fibrilar collagen matrices we tested, not only the more confining conditions. Interestingly, the requirement for MMP activity in efficient cell-matrix adhesion offers a mechanistic explanation as to why MMP inhibitors and integrin blocking antibodies have the same effect of promoting mesenchymal to amoeboid switching in 3D collagen matrices[65, 98]. The dependence on matrix degradability for proper adhesion and traction has been reported previously in a synthetic hydrogel model system as well. In this case, mesenchymal stem cells (hMSCs) embedded in proteolysis-resistant hydrogels could not generate cytoskeleton tension and thus produced insignificant deformations to the surrounding matrix[99]. Recent studies show that MMP proteolytic activity is also required for cell adhesion and spreading on collagen monomer-coated 2D substrates[100].

The requirement for matrix degradation in cell-ECM adhesion in fibrillar collagen I suggests that either binding sites must be revealed through degradation or that cells need to bundle and reorganize fibers to create stable adhesions. High- and low-affinity integrin-binding motifs are present in collagen fibrils[101] and could be differentially accessible based on architecture. Changes in the complex molecular assembly of bundled triple helices within the collagen fibril can make essential ligand binding sites cryptic or hidden from the molecular surface[101]. Indeed, it has been shown that collagen binding motifs can be differentially presented depending of fibril conformation and that this can modulate interaction with crosslinking enzymes and cell-ECM adhesion proteins[26]. It is believed that cell-collagen interactions are regulated by cryptic binding motifs being exposed upon structural reorganization or degradation of the fibril. Our results suggest that structural reorganization and degradation are linked. *in vitro*, deposition of collagen that is resistant to degradation occurs in fetal tissues[102, 103], fibrosis[104, 105, 106], and cancer[107, 108, 109, 110, 111]. Thus, the collagen-induced low adhesion state we identified

herein may be relevant to the onset and progression of these processes.

2.4 Methods

2.4.1 Cell culture

HT-1080 and MDA-MB-231 fibrosarcoma cells were purchased from (ATCC, Manassas, VA) and cultured in high glucose Dulbeccos modified Eagles medium supplemented with 10% (v/v) fetal bovine serum (FBS, Corning, Corning, NY) and 0.1% gentamicin (Gibco Thermofisher, Waltham, MA) and maintained at 37°C and 5% CO2 in a humidified environment during culture and imaging. The cells were passaged every 2?3 days as required.

2.4.2 Low attachment cultures

For measurements of cell activity under loss of attachment we used low attachment plates (Corning, corning, New York). Cells, were trypsin zed from standard cell culture flasks and passage into low attachment plates to a 50-60% confluency. For RNA extraction cells were collected by resuspension in PBS and centrifugation. For metabolism measurements, supernatant was collected from culture and spun down to clear cell debris.

2.4.3 3D culture in collagen I matrix

Cell laden 3D collagen matrices were prepared by mixing cells suspended in culture medium and 10X reconstitution buffer, 1:1 (v/v), with soluble rat tail type I collagen in acetic acid (Corning, Corning, NY) to achieve the desired final concentration[112, 113, 10] as described previously by our group. 1 M NaOH was used to normalize pH in a volume proportional to collagen required at each tested concentration (pH 7.0, 10-20 μL 1 M NaOH). Gels were polymerized at 37°C in a humidified incubator. To modify the structure of the collagen fibers

to obtain LDSF gels we used a technique previously reported by our group[114]. Briefly, Polyethylene glycol (PEG, MW=8000, Sigma, St. Louis, MO) was solubilized in phosphate-buffered solution (PBS) and filter sterilized. Solubilized PEG was then mixed into the cells, reconstitution buffer solution described above to produce a final PEG concentration of 10 mg/mL in the collagen gel. The gels were allowed to polymerized in the same conditions as collagen only gels. Collagen structure modification was verified using confocal reflection microscopy.

2.4.4 Confocal reflection microscopy

Confocal reflection images were acquired and processed as we have previously reported[66]. Briefly, Images were acquired using a Leica SP5 confocal microscope (Buffalo Grove, IL) equipped with a HCX APO L 20X 1.0 NAwater immersion objective. The sample was excited at 488?nm and reflected light was collected without an emission filter. Collagen fibril length was analyzed using the free software ctFIRE (http://loci.wisc.edu/software/ctfire) [115, 116].

2.4.5 Fluorescence recovery after photobleaching (FRAP)

To quantify actin polymerization activity at cell protrusion tips, HT1080 were stably transduced with Dendra-2-Lifeact (Dendra2-Lifeact-7 was a gift from Michael Davidson (Addgene plasmid # 54694)). Stably expressing cells were sorted (BD influx, FACS) to select for cell expressing the construct at low levels to avoid off target effects caused by high copy numbers. Cells were embedded into 3D collagen matrices as described before and incubated for 24 hours before assayed. FRAP was performed using an inverted confocal microscope equipped with temperature, CO2 and humidity controls for life cell imaging (Olympus FV100). Two images were taken as baseline, then a ROI was drawn around the protrusion tip (5 μm diameter circle) and the fluorescence was bleached during 10s, after that images were taken every 30 s until the fluorescence intensity was stable. Acquired baseline, photobleaching and recovery images were

processed offline using imageJ. Intensity traces were fitted using a single exponential curve and the mean recovery time was recovered from the exponential time constant tau.

2.4.6 3D matrix-bound fluorescent bead displacement analysis

To quantify collagen matrix deformations due to cellular forces, fluorescent carboxylate microspheres (1 um, Thermofisher Scientific, Waltham, MA) were added to the cell-gel solution before polymerization and GFP+ HT1080 cells were used to accurately track cell movements and protrusion extensions. Thoroughly mixed gels were the poured into custom made PDMS wells mounted on glass bottom dishes (Fluorodish, World precision Instruments). The gels were left to polymerize for at least 3 hours and full culture medium was added on top of the gels before imaging started. Imaging was performed using a Nikon TI inverted microscope equipped with a 40X (NA: 1.15) long working distance objective (Nikon Instruments Inc., Melville, NY). For each experiment replicate, between 6-9 cells were randomly selected around the matrix at different depths and a Z stack of images of the beads (red channel) and cells (green channel) was acquired every 0.8 μm, covering 17.5 μm above the cell and 17.5 μm below the cell every 2 minutes for 120 minutes. Offline analysis was performed by generating a extended depth of focus image (EDF) for each time point and tracking individual beads using ImageJ software (NIH, Bethesda, Maryland, USA, https://imagej.nih.gov/ij/). During data collection, special care was taken to select only cells that appeared mostly in polarized in the XY plane to avoid underestimation of Z movements by EDF analysis. We confirmed that the largest deformations imposed by the cells into the matrix happen in the cell plane (XY in this case). Although some information might be lost due to projection to a single plane of a 3D volume our internal controls confirm that deformations happening in the Z directions are significantly smaller than those happening in the XY directions Supplementary figure 3e.

2.4.7 Fluorescent beads trajectory analysis

Analysis of individual bead movements as a function of time yielded X,Y coordinates for each bead in the field of view for each time point. Supplementary Figure 2 describes the algorithm followed to extract different metrics from that coordinate data. First, a filter was applied to analyze only trajectories of beads that were picked up by the PIV software at all time points. Thus, beads that became out of focus of some imagining artifact impeded proper tracking were discarded. Second, the displacement at each time point from the initial point was calculated for each bead, which yielded trajectories like the ones depicted in Supplementary Figure 2b. Next, to identify beads that were actively pulled by the cells we used a moving standard deviation approach were we calculated the standard deviation of consecutive points across the entire bead trajectory. With this, as can be visualized in Supplementary Figure 3c, we were able to identify the parts of the trajectory that significantly deviate from the rest, which corresponds to a deformation in the matrix. Importantly, when examining the trajectories that are thresholded out using this method versus the ones that are kept, we can see that a bead that is very close to a cellular protrusion, and thus being strongly pulled, is kept (Supplementary Figure 2f), whereas a trajectory that shows only a drift like movement is thresholded out (Supplementary Figure 2e). From the trajectories that passed this threshold we then calculate max bead displacement (Figure 2.3b) and cell slip ratio metrics (Figure 2.4b).

2.4.8 Whole cell slip ratio calculation

Slip ratios were calculated as the ration between the instant cell velocity and the surrounding beads instant cell velocity. Cell instant velocity was calculated by tracking single cells using metamorph software (Molecular devices, San Jose, CA). Cell tracking produces x,y coordinates for the cell body at every time-lapse frame and instant velocity is computed as the distance traveled by the cell between consecutive frames. For surrounding beads instant velocity, we

tracked the trajectory of all beads in a 165x165 μm square around the cell body using ImageJs plugin MOSAIC particle tracker (http://mosaic.mpi-cbg.de/?q=downloads/imageJ). For beads trajectories, we performed the same analysis as for cell trajectories to obtain a frame by frame velocity. Slip ratio was calculated as the cell velocity divided by the average of all bead velocities around the cell (Supplementary Figure 1d).

2.4.9 Western blotting from 3D constructs

Whole 200μL 3D collagen constructs from the different culture conditions were scooped out if the well into vials containing 2mL of PBS and immediately spun down at 1500xg for 5 mins. Supernatant was the discarded and 200μL of lysis buffer containing proteases and phosphatates inhibitor cocktails was added to the pellets (Thermofisher Scientific, Waltham, MA). The samples were then sonicated on ice for 30s and immediately after loading buffer containing SDS and DTT was added to get a final 1X concentration. The samples were incubated on ice in loading buffer for 1h with vortexing every 10-15 mins. After this, the samples are spun down at 12000xg for 10 mins and then boiled at 95C for 5 mins. Proteins are separated by SDS-PAGE and transferred to a PVDF membrane. Membranes were probed with antibodies against phosphorylated FAK (44-624G, Thermofisher) and tubulin (TU-01, thermofisher).

2.4.10 Gene expression using RNA Sequencing

A previously generated RNA Sequencing dataset was used to investigate gene expression changes associated with short fiber architecture[66]. Briefly, total RNA was extracted using Trizol and prepared for sequencing on the Illumina MiSeq platform at a depth of ¿25 million reads per sample. The read aligner Bowtie2 was used to build an index of the reference human genome hg19 UCSC and transcriptome. Paired-end reads were aligned to this index using Bowtie262 and streamed to eXpress63 for transcript abundance quantification using command line

$bowtie2 - a - p10 - x/hg19 - 1reads_R1.fastq - 2reads_R2.fastq|expresstranscripts_hg19.fasta.$ For downstream analysis TPM was used as a measure of gene expression.

2.4.11 Gene set enrichment analysis (GSEA)

Gene set enrichment analysis was performed using the Broad institute GSEA tool software.broadinstitute.org/gsea/index.jsp) with standard settings. Rank list were constructed from mean log2 fold change from 2.5 mg/mL to 6 mg/mL culture conditions across 3 biological replicates.

2.4.12 Gene expression analysis using panther database

To identify gene expression programs upregulated in highly confining matrices, we used a gene module previously reported by us that is commonly upregulated to HT1080 fibrosarcoma cells and MDA-MB-231 breast cancer cells cultured in this matrix (6 mg/mL collagen). The 70 gene module was used as input for panther database analysis (http://www.pantherdb.org/geneListAnalysis.do) and enrichment test was performed.

2.4.13 Glucose, lactate and glutamine measurements

Medium from the indicated culture conditions was harvested after 24h of incubation under standard cell culture conditions. Aliquots were spun down at maximum velocity to clear cell debris. Glucose, glutamine and lactate were measured in the collected samples and in medium incubated under the same conditions but without cells, using a YSI 2950 biochemistry analyzer (YSI, Yellow Springs, OH). Consumption and production was calculated as a delta between the experimental samples and the non-cell counterparts.

2.4.14 DQ collagen degradation assay

Local matrix degradation was measured using DQ collagen (Thermofisher Scientific, Waltham, MA). Briefly, collagen matrices were prepared as described above with 100 μg/mL of DQ collagen mixed in. Cell laden DQ-gels were incubated for 24hs in standard cell culture conditions in the presence of full cell culture medium. 3D gels were imaged using a confocal microscope equipped with a 40X objective (NA:0.75) (Olympus FV100). Zstacks were acquired at a 0.4 μm step size covering the entire cell body. Images were processed offline using ImageJ. DQ intensity was quantified as the mean intensity around the cell body minus the mean intensity of an ROI of the same area in a gel area without cells to account for background DQ signal. In order to measure degradation by Matrix Metalloproteinase 8 (MMP8), 3D Collagen I-DQ matrices were formulated as previously described. Recombinant Human MMP?8 (rhMMP-8) (R&D Biosystems, Catalog # 908-MP) was activated at 100 μg/mL with 1 mM p-aminophenylmercuric acetate (APMA) (Sigma, Catalog # A-9563) in TCNB Assay Buffer at 37 °C for 1 hour. Following incubation, activated rhMMP-8 was diluted to 1.0 ng/μL in TCNB assay buffer and was added on top of each of the gels to a final concentration of 0.45 μg/mL. Within 10 minutes of MMP8 exposure, florescence was measured using a Tecan Infinite 200 Pro (Tecan, Mannedorf, Switzerland) at the stem cell core of Sanford Consortium of Regenerative Medicine (La Jolla, CA). Florescence top reading was measured at excitation (488 nm) and emission (525 nm) over a kinetic cycle of 13 hours with 2 minute intervals.

2.4.15 Diffusivity analysis

To assess whether diffusion was limited in more confining matrices (Supplementary Figure 7), we prepared collagen gels as described above and polymerized them inside commercially available rectangular microchannel (μ-Slide VI 0.4, IBIDI, Munich, Germany). 88 μM solutions of fluorescein conjugated dextran were prepared and added to one end of the microchannel

while keeping cell growth medium in the other end. The gels were then placed in the stage of a fluorescence microscope and imaged at 1 min intervals for 8 hours to monitor the fluorescence signal as an indicator of dextran concentration along the collagen matrix. Images were then analyzed using imageJ and a concentration profile was acquired for each time point. The obtained data was fitted to a 1-D diffusion process using equation 1 and the parameter D extracted.

$$C(t,X) = C_{max} * \left(1 - erf\left(\frac{X}{2\sqrt{Dt}}\right)\right)$$

where C_max is the initial concentration at the source and erf is the error function.

2.4.16 Quantitative reverse transcription PCR (RT-qPCR)

For qPCR experiments RNA was extracted using High Pure RNA Isolation Kit (Roche, Basel, Switzerland). cDNA was synthesized using superscript iii first-strand synthesis system (Thermofisher, Waltham, MA). Relative mRNA levels were quantified using predesigned TaqMan gene expression assays (Thermofisher, Waltham, MA). Relative expression was calculated using the DCt method using GAPDH as reference gene. Assays used were: GAPDH ($Hs02758991_g1$), MRC2 ($Hs00195862_m1$).

2.5 Supplementary material

2.5.1 Supplementary figures

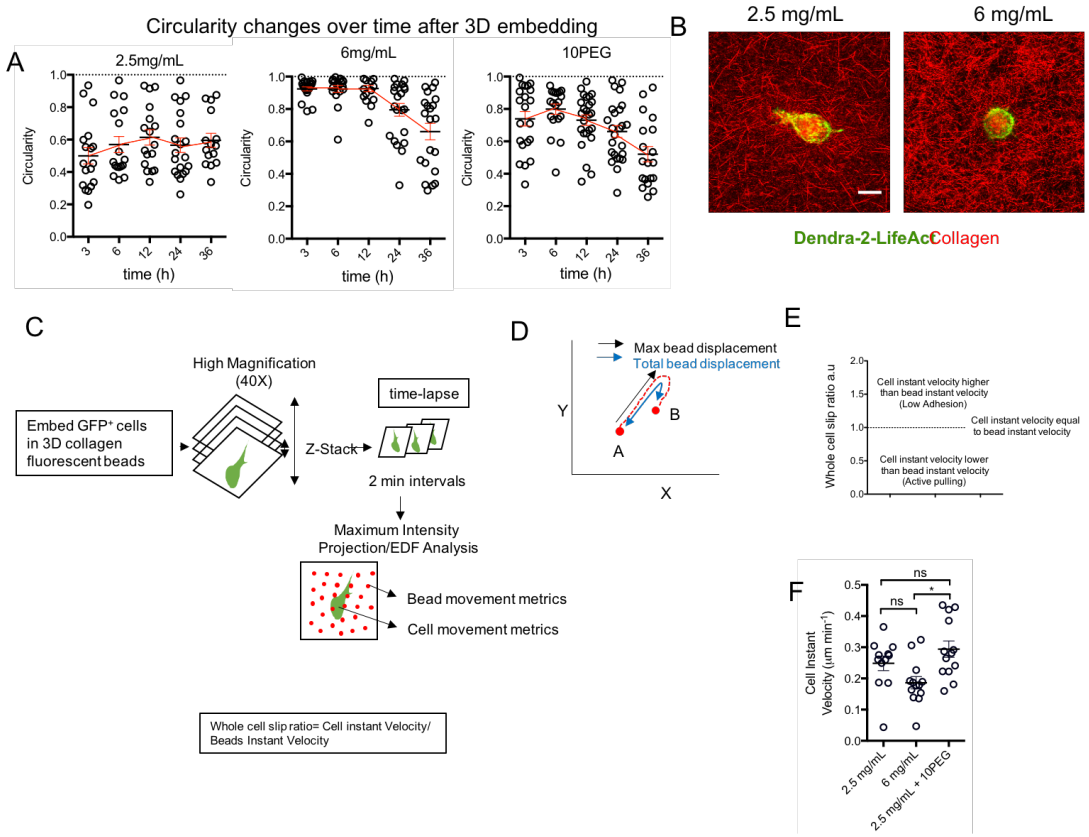

Figure 2.7: **Supplementary Figure 1 a.** Time dependent evolution of cell circularity in the three matrix conditions as measured by low magnification bright field time-lapse microscopy. **b.** Overlay images of cells expressing Dendra-2-LifeAct (Actin) and the surrounding collagen fibers as imaged by confocal reflection microscopy. **c.** Schematic representation of the strategy used to quantify cell-ECM interactions and estimate cell slip ratio. **d.** Schematic representation of the metrics used to quantify matrix deformations upon bead tracking. Max bead displacement is the maximum distance a bead is displaced from its initial (0,0) position. **e.** Definition of the whole cell slip ratio metric used to estimate the level of cell adhesion to the surrounding ECM (see methods). **f.** Instant cell velocity for cells analyzed to calculate slip ratio.

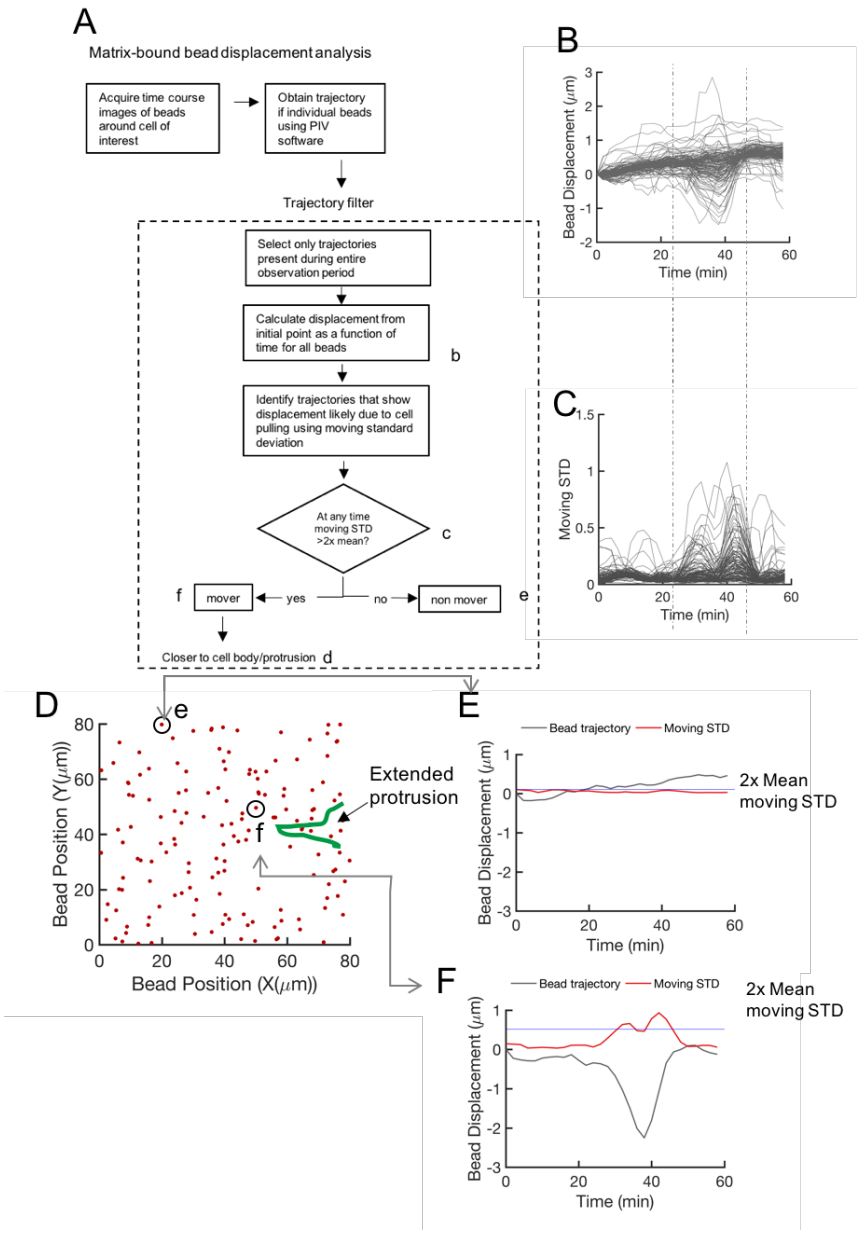

Figure 2.8: **Supplementary Figure 2 a.** Flow chart describing the algorithm followed to analyze the bead movement around cells (see methods). **b.** Representative data for a cell in a LF matrix. Each line represents the trajectory of a single bead respect to its initial position in the matrix. The big dip observed between 20-40 minutes corresponds to a protrusion associated deformation event. **c.** Moving standard deviation of each of the trajectories depicted in B. Large moving standard deviation signify a large sudden displacement from the overall trajectory, and it served to differentiate bead displacements caused by active cell pulling versus random motion or microscope drift. **d.** Coordinate map of all the beads in the same representative cell, where a highly moving bead (close to cell protrusion) and a non- moving bead (far away from cell protrusion, are highlighted. **e.** Trajectory of the non-moving bead and **f.** Highly moving bead, showing how thresholding by a high moving standard deviation can select moving vs non-moving.

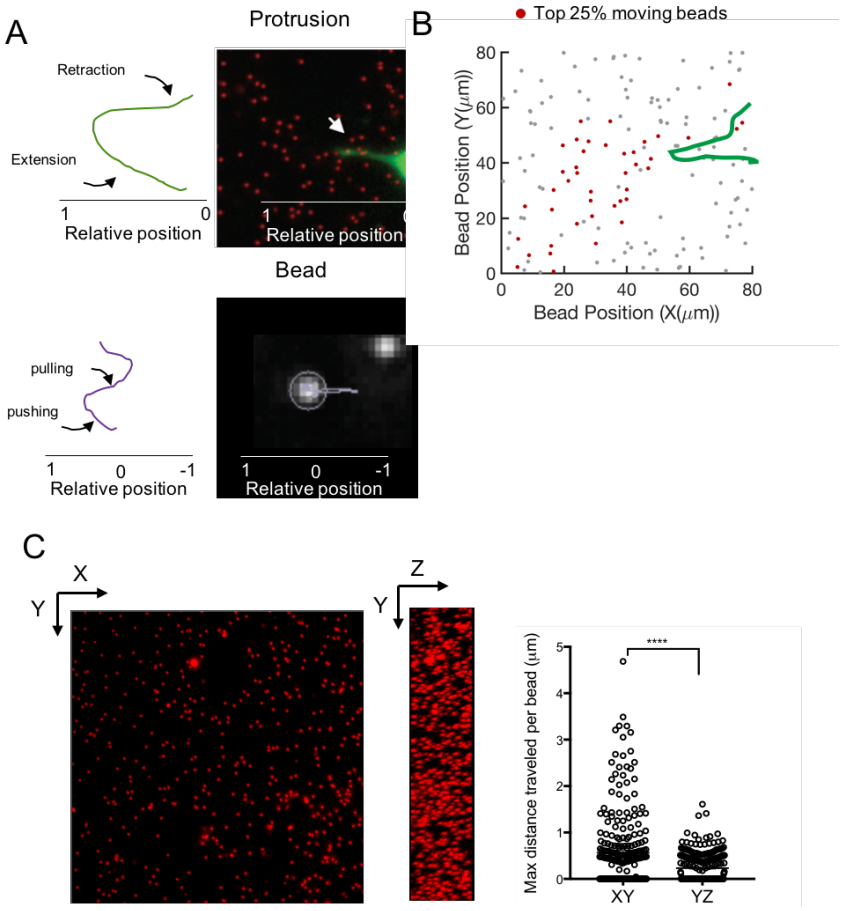

Figure 2.9: **Supplementary Figure 3 a.** Schematic representation of the approach used to simultaneously analyze protrusion extension/retraction and bead movement around it. **b.** A representative coordinates field for beads in a 2.5 mg/mL matrix. Shown in green is the location of the extending cell protrusion and highlighted in red are the top 25% moving beads. **c.** Analysis of bead movement in XY vs ZY planes. Maximum intensity projections for both planes were constructed and single bead tracking was performed. (See methods)

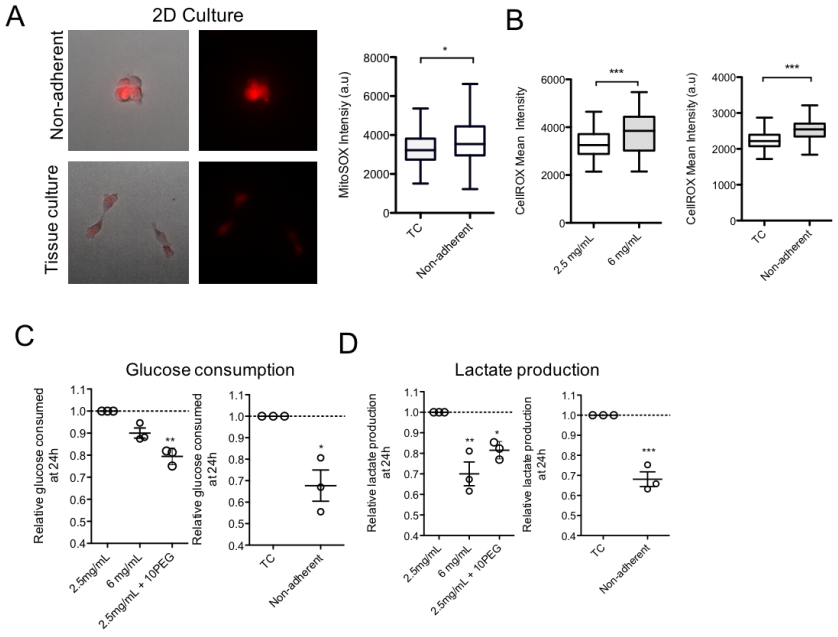

Figure 2.10: **Supplementary Figure 4 a.** Representative micrographs and quantification of mitochondrial ROS using mitoSOX dye in HT1080 cells cultured in 2D plastic culture dished (TC) or low attachment plates (Non-adherent). **b.** Quantification of cellular ROS using CellROX dye in short fiber architecture 3D cultures (left) and 2D cultures in tissue culture treated dished (TC) or low attachment plates (Non-adherent). **c.** Relative glucose uptake for cells growing in 6mgmL-1 and P10 as compared P0 matrices.

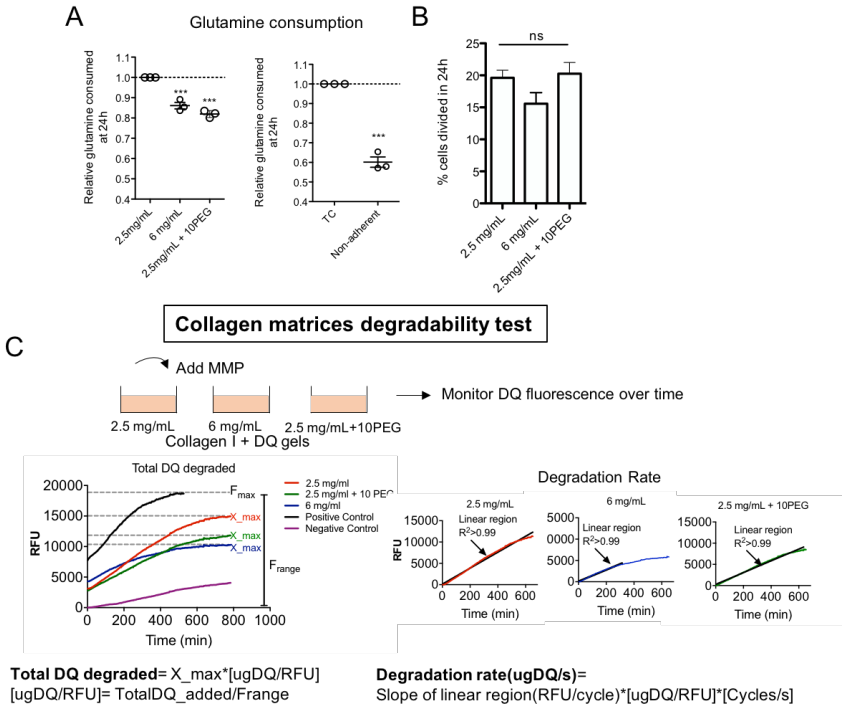

Figure 2.11: **Supplementary Figure 5 a.** Relative lactate production and **b.** Relative glutamine uptake for cells growing in 6mgmL-1 and P10 as compared P0 matrices. **c.** Fraction of cells diving in the 3 matrix conditions at 24h after seeding. **d.** Schematic representation of the *in vitro* collagen degradability assay (see methods) used to quantify differences in the architecture dependent degradability of collagen gels. n>=3 biological replicates for each experiment, statistical significance described as *, **, *** for $p<0.05$, $p<0.01$, $p<0.001$ respectively

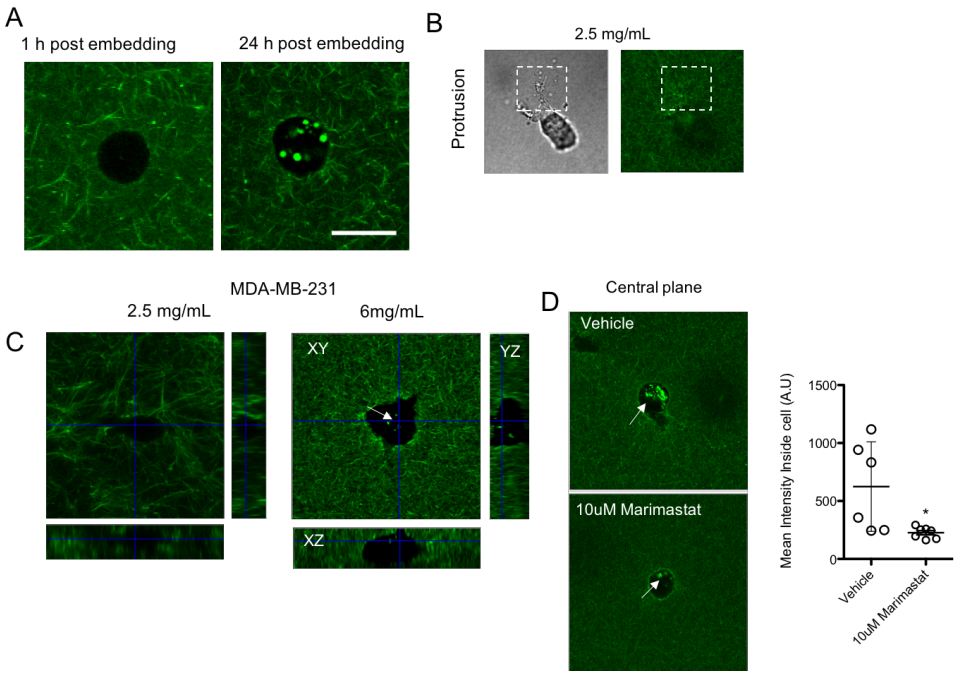

Figure 2.12: **Supplementary Figure 6 a.** Micrographs of HT1080 cells embedded in a 6 mg/mL collagen matrix with DQ collagen at 1 hour after embedding (left) and 24 hours after embedding (right), scale bar 25 μm **b.** Confocal micrographs focused at a protrusion of a cell in a 2.5 mg/mL collagen gel with DQ collagen, showing no signal above the background around the protrusion. **c.** Confocal micrographs of a MDA-MB-231 breast cancer cell where internalization of DQ collagen is evident in the 6mg/mL SF matrix but not in the 2.5m/mL LF matrix. D. Representative images and quantification of internalized DQ collagen in HT1080 cells in a 6 mg/mL SF matrix with (bottom) and without (top) treatment with the broad spectrum MMP inhibitor Marimastat.

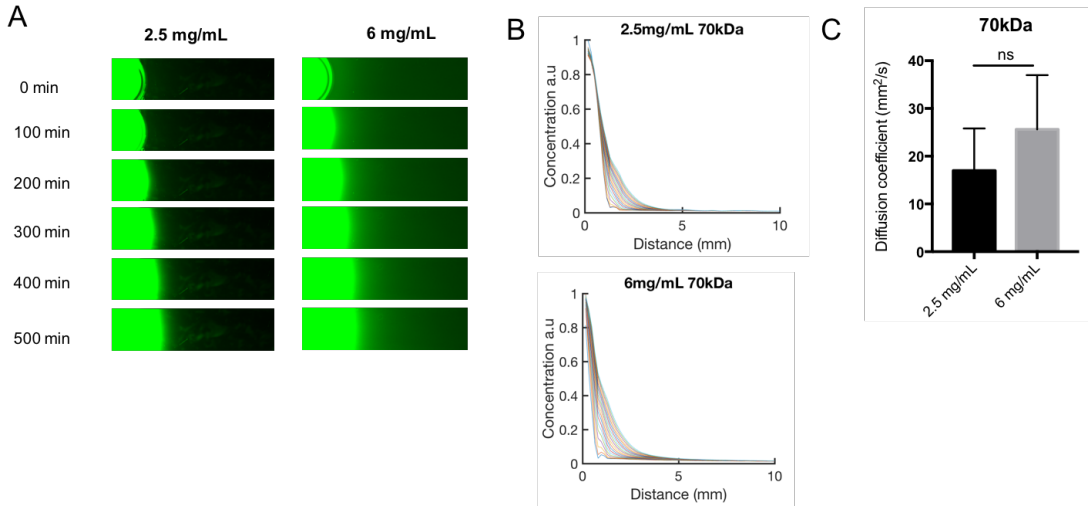

Figure 2.13: **Supplementary Figure 7 a.** Micrographs showing a time series of 70kDa FITC dextran diffusion into P0 and 6 mg/mL gels **b.** Concentration profiles for the conditions shown in A **c.** Estimated Diffusion coefficient for the conditions presented in A.

2.6 Aknowledgments

Chapter II, is a partial reprint of Velez, D.O , S.K. Ranamukhaarachchi , R.N. Modi , A. Kumar , A. J Engler , S.I. Fraley ”Collagen architecture-induced metabolic and oxidative stress precede collective migration”. Which has been submitted for publication. The dissertation author was the primary investigator and author of this paper.

S.F. and D.O. developed the project. D.O., S.R., and R.M. conducted MMP-8 degradation and diffusivity experiments. A.K. and S.R. conducted and analyzed AFM measurements with guidance from A.E. D.O. conducted all other experiments. S.F. and D.O. wrote the manuscript and all other authors edited the manuscript.

We would like to thank Christian Metallo for use of his YSI analyzer and Mehmet Badur for assistance. We also thank Pedro Cabrales for use of his shear rheometer. We thank Wei Zhang for his help with gene set enrichment analysis.

S.F. and lab is supported by a Burroughs Wellcome Fund Career Award at the Scientific

Interface (1012027), NSF CAREER Award (1651855), ACS Institutional Research Grant (15-172-45-IRG) provided through the Moores Cancer Center at UCSD, and UCSD FISP grants. Support was also provided by NIH grants (R01CA206880 to A.J.E.) and by fellowship support via NSF GRFP and NIH T32AR060712 (to A.K.).

Chapter 3

In vivo Models to Deconstruct the Role of Collagen 'Density' in the Tumor Microenvironment in Promoting Cancer Cell Metastasis

3.1 Introduction

A dense stromal microenvironment has been widely recognized as an epidemiological risk factor for the development and progression of cancer, especially in breast cancer [117, 118]. Pioneering work from Patricia Keely and colleagues, causally linked collagen density in the breast stroma to tumorigenesis[3]. Using a mouse model of increased collagen deposition in the mammary fat pad, they identified high density collagen content in the stroma of breast tumors as a key determinant of tumor incidence and metastatic potential. Even though this seminal work laid the grounds for an understanding of dense stroma as a risk factor, the molecular mechanisms leading to cancer cell transformation into aggressive phenotypes remain largely unknown.

Importantly, the mechanism by which Keely and colleagues were able to establish a mouse model of increased stromal density in the context of mammary carcinogenesis was by using a mouse model for decreased collagen degradability. Briefly, this model harbors a targeted mutation at the known collagenase cleavage site in the collagen type I gene[119]. In this model, reduced or (in the homozygous case) completely impaired, collagen degradation promotes a general buildup of collagen I, including in the mammary gland. When combined with a model of spontaneous mammary carcinoma development such as the Polyomavirus middle-T mice under the control of the mammary specific MMTV promoter (abbreviated PyVT), they were able to obtain mammary tumors with a dense collagen stroma. Thus, in this model, collagen degradability is the primary perturbation, and increased density is a consequence. This convoluted interplay between collagen density and other physical properties such as crosslinking, degradability or stiffness has made the experimental dissection of key parameter regulating cell behavior challenging.

Using 3D culture models, we have demonstrated that low-degradability collagen matrices can trigger breast cancer cells to switch to highly persistent and collective cell migration, regardless of overall collagen density. This shift in cell behavior then leads to the development of multicellular structures highly enriched in basement membrane production, which resemble a phenotype known as vasculogenic mimicry (VM) [66]. Furthermore, we show that this phenomenon is induced independently of matrix stiffness or hypoxia, but rather by collagen fibril architecture, which determines collagen degradability by cellular matrix metalloproteinases (MMPs). At a molecular level, our work suggests this highly aggressive phenotype is initiated by a cell stress response to low ECM attachment that is in part mediated by the incapacity of the cancer cells to effectively degrade the surrounding collagen. In this model, cancer cells enter a state of low attachment, due to their inability to effectively use MMPs and properly attach to the fibers. This state of low attachment then triggers metabolic stress signatures such as production of reactive oxygen species, decreased glycolysis and a transcriptional response characterized by the downregulation of the mTOR pathway and upregulation of antioxidant response genes, NOTCH

signaling genes, and conserved gene module associated with transdifferentiation to multicellular structure formation (chapter 2 and [66, 70]).

Given these characteristics of the mouse model used by the Keely group, and considering the *in vitro* results previously reported by our group, we propose that low degradability of the collagen in the tumor microenvironment and not density per se might be a key trigger for the development of highly aggressive phenotypes. Furthermore, we propose that loss of attachment stress due to low degradability might represent the basis for the molecular mechanism explaining dense stroma as a risk factor for metastatic breast cancer. Animal models can address these question and confirm our observations *in vitro*. Importantly, animal models attempting to study the role of collagen in tumor progression and metastasis, should allow for the uncoupling of collagen density and other physical properties such as degradability. Here we present the use of two different animal model approaches to ask whether low-degradability induced transformation of cancer cells into collective migration and a VM-like state represents an *in vivo* mechanism for metastasis: i) First, we combine our 3D culture approaches with an orthotropic mouse model of breast cancer to ask whether collagen induced collective migration *in vitro* represents a more metastatic phenotype *in vivo* and whether this phenotype is functionally equivalent to VM *in vivo*; ii) Second, we build on the work by the Keeley group using a model of spontaneous mammary tumor development in a low-degradability collagen microenvironment to determine whether this environment induces VM *in vivo* and whether VM can explain the enhanced metastasis observed in this model.

3.2 Orthotropic implantation of 3D cultured breast cancer cells

For this model we used a cell line of highly metastatic triple negative breast cancer (MDA-MB-231). This cell line was used in our previous studies where we discovered the transcriptional

response and phenotype associated with VM. To be able to quantify the number of cells present in different organs at the end of the experiment, we used a green fluorescent protein (GFP) expressing version of this cell line (MDA-MB-231 GFP+) and implanted them into NSG mice (NOD-SCID-Il2rg-/-) after 5 days of culture in different matrix conditions that allow for the decoupling of collagen density and degradability i) VM inducing matrices (6 mg/mL, high density low degradability and 2.5 mg/mL + 10mg/mL PEG, low density low degradability) and ii) non VM inducing matrix (2.5 mg/mL, low density high degradability). A schematic representation of the protocol followed in this experiment is shown in (Fig 3.1 a). Previous studies of orthotropic implantation into immunocompromised mice [120] showed a high capacity for metastasis into the lungs, liver and spleen. Therefore, we will focus on those organs for the quantification of metastatic burden.

3.2.1 Tumor growth is not affected by collagen degradability

Tumors consistently developed and grew after implantation in the 3D constructs irrespective of matrix condition (7/7 for 2.5 mg/mL and 6/6 for 6 mg/mL), indicating a high capacity of these cells to engraft and grow in the NSG mouse model. Measurement of tumor volume at different time points during the experiments showed a great heterogeneity in the tumor growth, and thus, we saw no significant differences in the tumor sizes when comparing cells implanted on a VM phenotype (6 mg/mL, high density low degradability) vs cells implanted as single cells on a collagen matrix (2.5 mg/mL, low density high degradability). Additionally, we observed no evident differences in the macroscopic appearance of the tumors after dissection at week 6 (Fig 3.1 b-c). Current work involves the use of an additional matrix (2.5 mg/mL collagen + 10mg/mL PEG, low density low degradability), which allows for the decoupling of ligand density and degradability and their effect in tumor growth.

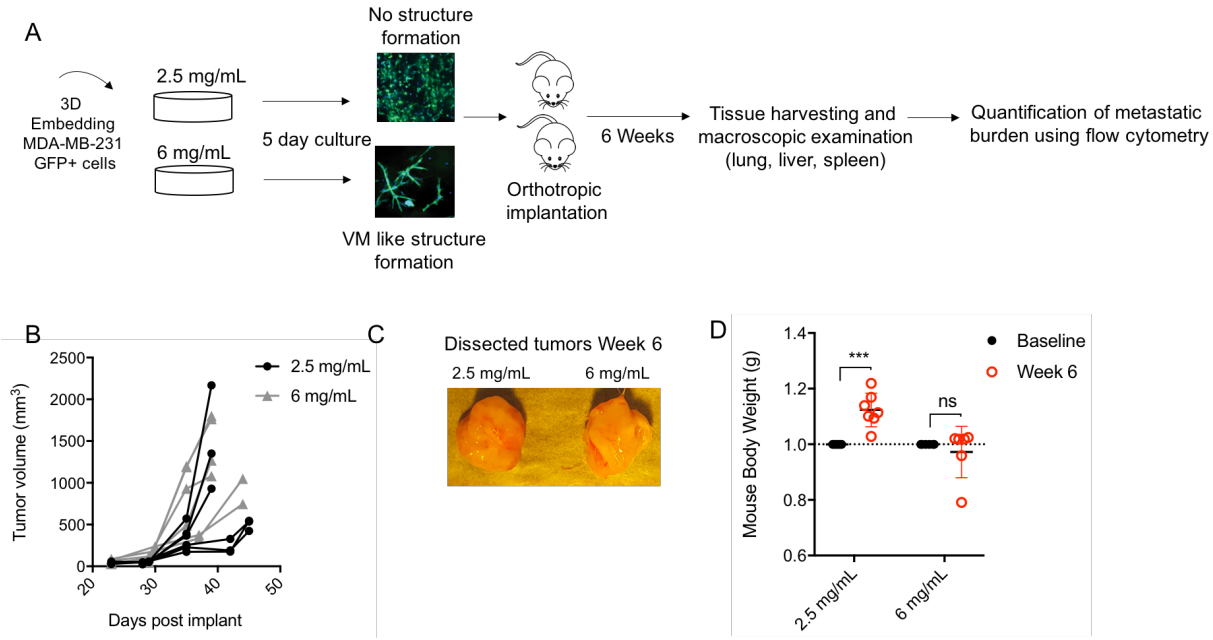

Figure 3.1: **Orthotropic implantation of 3D cultured breast cancer cells into immunocompromised mice a.**Schematic description of the experimental protocol followed. n=6 mice for 2.5 mg/mL and n=7 mice for 6 mg/mL. **b.** Tumor volume changes with time. **c.** Dissected tumor show no evident differences. **d.** Changes in mouse body weight between the beginning of the experiment and the endpoint. Statistical significance was determined by Mann-Whitney U test and is indicated as *, **, *** for $p<0.05$, $p<0.01$, $p<0.001$, respectively

3.2.2 Metastatic burden is increased by low-degradability collagen

At the end point of the experiments, we observed a noticeable difference in the overall health of the mice as was evidenced by the relative changes in body weight between the two groups, where the mice in the non-VM inducing matrix had gained around 10% body weight during the tumor growth period, the mice implanted with the VM-induced cells either remained at their initial weight or lost weight (Fig 3.1 c). This observation indicated the possibility of higher metastatic disease in the VM-induced implanted group compared to the non-VM group. To test this, we harvested key target organs (Fig 3.1 a), dissociated them and analyzed the load of GFP+ cells present in each organ as a metric of metastatic disease (see methods). We observed that the organ with the highest metastatic burden were the lungs, as observed by macroscopic examination and by GFP+ cell quantification, consistent to what has been reported for this model

[121]. However, we observed no significant differences between the two experimental groups (Fig 3.2 a). In the spleen we observed no visible metastatic lesions by macroscopic examination, and even though there was a small increase in the percent of GFP+cells recovered in the spleens of the 6 mg/mL group, the differences were not significant either (Fig 3.2 b). Interestingly, we observed the most differences between both groups when looking at the liver tissue, in this case the percentage of recovered GFP+ cells was significantly higher in the 6mg/mL mice compared to the 2.5 mg/mL and macroscopic examination showed visible metastatic lesions of a larger size in the 6 mg/mL mice (Fig 3.2 c). In this analysis, inclusion of a matrix with low density and low degradability (2.5 mg/mL + 10mg/mL PEG) will serve to uncouple density and degradability and dissect their role in increased metastatic potential.

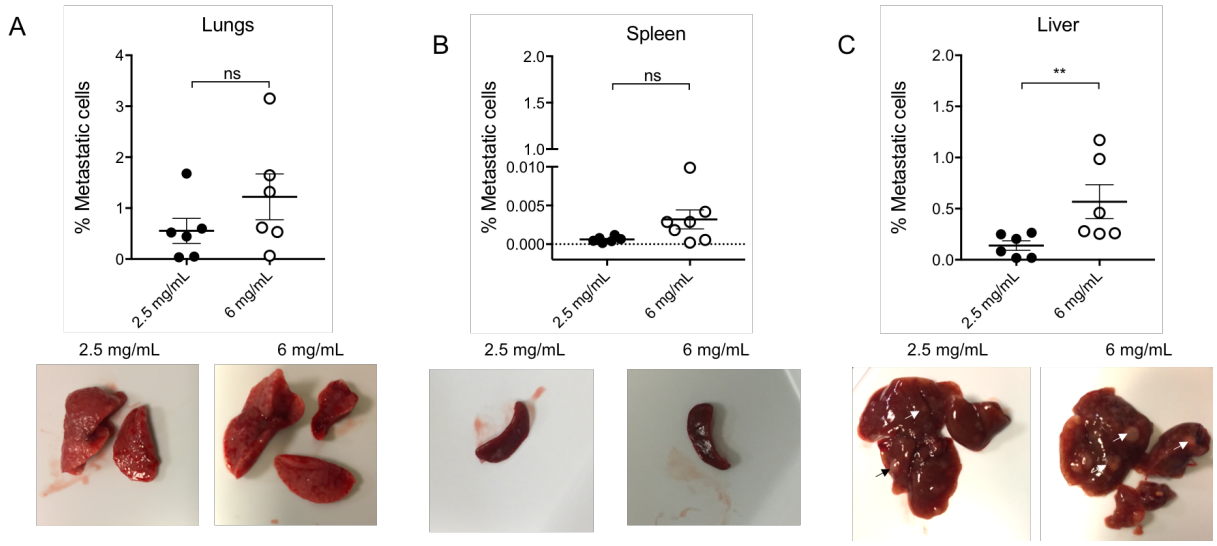

Figure 3.2: **Quantification of metastatic cells in organs of interest** Flow cytometry was used to quantify the amount of GFP+ cells is the organs of interest. Top figures show % metastatic cells quantification and bottom figures show macroscopic appearance of **a.**Lungs. **b.** Spleen. and **c.** Liver. n=6 mice for 2.5 mg/mL and n=7 mice for 6 mg/mL. Statistical significance was determined by Mann-Whitney U test and is indicated as *, **, *** for $p<0.05$, $p<0.01$, $p<0.001$, respectively

3.2.3 Preliminary Conclusions and Future Direction

Taken together, these results suggest to us that in this model, 6 weeks of tumor growth represent a late stage, where lungs and liver are colonized and in the case of the 6 mg/mL group, the health of the animals is diminished. Importantly, the observation of significant differences in metastatic burden in the liver but not the spleen or the lungs, suggest to us that there might be an organ colonization path, were cells first establish on the lungs and later on the liver. Observation of higher number of cells in the livers of mice implanted with VM forming cells, thus suggest that those cells might have left the primary tumor earlier and thus had longer incubation times in distant organs like the liver. Future work in this area is focused on establishing a timeline for progression of metastatic burden in different organs. For this, we propose the use of luciferase expressing cells, and the performance of *in vivo* imaging at different time points after implantation. We hypothesize that if VM forming cells represent a highly metastatic phenotype, and they are able to colonize earlier the lungs and liver, we would detect luciferase signal in such organs at earlier time points. Additionally, to confirm that the observed VM phenotype could have a functional role increasing tumor perfusion, we propose to use intravital microscopy to measure localization of blood flow relative to VM like structures *in vivo*.

3.3 PyVT/COL1A1 Model

Based on our previous observation *in vitro* that low degradability collagen can trigger a migration and transcriptional response in cancer cells that is correlated with VM, we asked whether this *in vitro* phenotype could mechanistically explain the observations made in the PyVT/COL1A1 mouse model. As described before, in this model, increased density is achieved by impairing collagen degradability, which makes it an ideal model to study the role of low degradability in the development of VM and metastasis. To do this, we first stained tumor sections using Periodic Acid Schiff (PAS), the most well accepted marker for VM in histology slides [122]

and used an image processing algorithm to quantify the abundance of PAS positive structures in tumors with dense collagen (PYVT/COL1A1 heterozygous) in comparison to tumors with normal collagen levels (PyVT/COL1A1 wt) (Fig. 3.3 a).

3.3.1 PyVT/COL1A1 mouse mammary tumors show evidence of VM

Evaluation of PAS+ structures in 4 mice of each genotype, revealed a significant increase in the PyVT/COL1A1 heterozygous mice compared to the wild type counterparts (Fig. 3.3 b). These results suggest the possibility that VM like structures identified *in vitro* might also be present in this mouse model *in vivo*.

3.3.2 Preliminary Conclusions and Future Directions

Further exploration of these tumor tissue and sections is required for more detailed characterization of the observed PAS+ structures to be able to link them to metastatic potential. More detailed characterization includes: i) double staining of CD31 (endothelium marker) and PAS to identify CD31-PAS+ structures (vessel like structures denuded of endothelium)[17]. ii) visualization of tumor cells relative to stromal cells to identify chain like or network structures resembling *in vitro* VM. iii) visualization of red blood cells relative to possible VM structures with increased tumor perfusion. And iv) RNA analysis for the identification of a VM gene expression signature. Additionally, since *in vitro* we observe signs of a collective migration phenotype being activated in low degradability matrices, future directions include the staining for known markers of leader cell phenotype in collective migration[60].

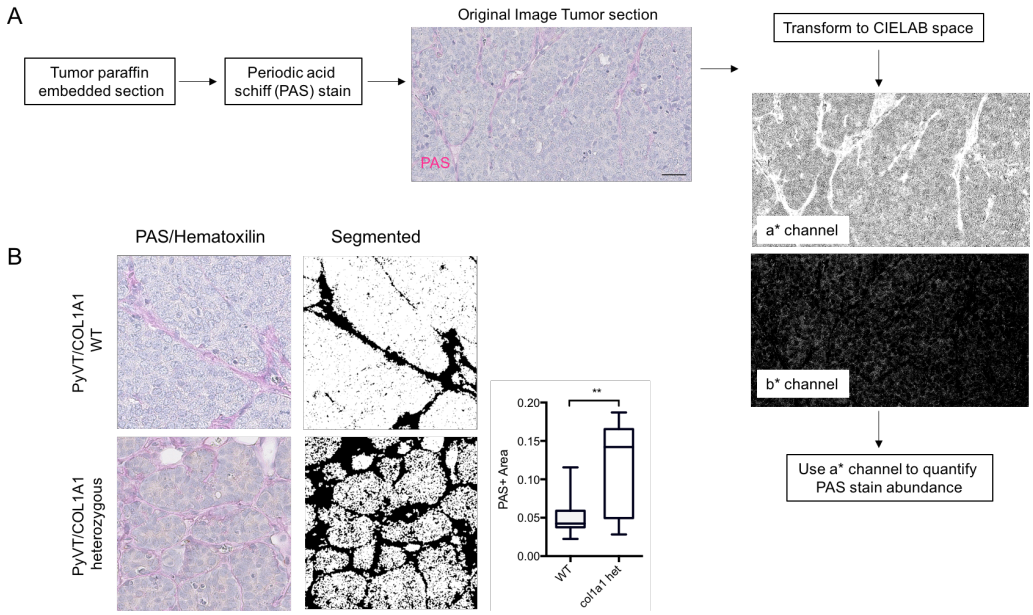

Figure 3.3: **Analysis of tumor sections from PyVT/COL1A1 mouse model a.**Schematic description of the strategy followed to analyze the PAS stained tumor sections. **b.** Quantification of PAS positive area in tumors from COL1A1 wild type mice vs. COL1A1 heterozygous mice. n=4 mice per experimental group. From each tumor section 5 fields of view were randomly selected for analysis. Statistical significance was determined by Mann-Whitney U test and is indicated as *, **, *** for $p<0.05$, $p<0.01$, $p<0.001$, respectively

3.4 Methods

3.4.1 Cell maintenance and 3D culture in collagen I matrix

For implantation experiments, MDA-MB-231 breast cancer cells expressing green fluorescent protein (GFP) were used. Cells were cultured in high glucose Dulbecco's modified Eagle's medium supplemented with 10% (v/v) fetal bovine serum (FBS, Corning, Corning, NY) and 0.1% gentamicin (Gibco Thermofisher, Waltham, MA), and maintained at 37°C and 5% CO2 in a humidified environment during culture and imaging. The cells were passaged every 2-3 days. Cell laden 3D collagen matrices were prepared by mixing cells suspended in culture medium and 10X reconstitution buffer, 1:1 (v/v), with soluble rat tail type I collagen in acetic acid (Corning, Corning, NY) to achieve the desired final concentration[19, 20]. A solution of 1M

NaOH was used to normalize pH in a volume proportional to collagen required at each tested concentration (pH 7, 10-20μL 1M NaOH), and the mixture was placed in 48-well-culture plates and let polymerize at 37°C. Final gel volumes were 200μL.

3.4.2 Animal experiments involving surgical procedures

All experiments were approved by the University of California San Diego, Institutional Animal Care and Use Committee, and conducted according to the Guide for the Care and Use of Laboratory Animals (US National Research Council, 2010). For surgical implantation of 3D collagen tissue constructs, NSG mice (NOD.Cg-Prkdc^{scid}Il2rg^{tm1Wjl}/SzJ , Jackson laboratories stock #005557) were used. Anesthesia was induced using 3-4% and maintained with 2-3% isoflurane, after verification of deep anesthesia via toe pinch test, the area adjacent to the second mammary fat pad was cleaned and all fur removed. A small incision between 5 to 10 mm long, was performed in the area were the fat pad could be visualized. Using blunt dissection and forceps, the tissue surrounding the fat pad was dissected in order to create a space for the implantation of the collagen plug. After this, the cell laden collagen gel was inserted and the incision sutured using prolene sutures (Ethicon, Somerville, NJ). After verifying that the incision was properly closed, the animals were left to recover in their cages and monitored daily for signs of infection or pain.

3.4.3 Quantification of metastatic burden using flow cytometry

After the 6 week tumor growth period was completed, animals were sacrificed by CO2 asphyxiation as per IACUC guidelines. Immediately after death was confirmed via cervical dislocation, the organs of interest were harvested, phtographed and immediatley immersed in a ice cold PBS solution. After all organs were harvested, the PBS solution was replaced by a solution containing 2mg/mL collagenase (Sigma, St. Louis, MO) and each organ was

dissociated mechanically using surgical scissors. Once the whole organ was homogenized, they were incubated at 37C for 1 hour with shaking every 15 min. After a homogeneous dissociated organ solution was obtained, they were strained trough a 70μm filter and resuspended in 500μL of FACS buffer (PBS, 1% BSA, 1mM EDTA). Then 75μL of each sample were run on a benchtop flow cytometer (BD, Accuri C6, BD, Franklin Lakes, NJ) to quantify the number of GFP+ cells in each sample. Percent of metastatic cells was calculated as:

$$\%Metastaticcells = \frac{\#GFP+cells}{Totalnumberofcells} * 100$$

3.4.4 Animal model of collagen dense stroma

The animal model for collagen dense stroma was first developed in the Keely lab. All the experiments described in this chapter involved the analysis of tissues kindly shared by Patricia Keely and her group. Briefly, mice having a highly collagen dense mammary tumors were generated by crossing PyVT mice (FVB/N-Tg(MMTV-PyVT)634Mul/J, Jackson laboratories stock #002374) with mice that harbor a mutation in their collagen 1 gene (COL1A1) that renders their stromal collagen type I resistant to degradation by collagenases and thus, develop and accumulation of collagen in their tissues including the mammary fat pads. Offspring of this cross breeding strategy could be PyVT carrier and COL1A1(WT) or COL1A1(het). Mice from the genotype corresponding to COL1A1 heterozygous develop spontaneous tumors with dense stromal whereas mice with genotype COL1A1 wild type generate spontaneous tumors with normal collagen levels.

3.4.5 Tissue section staining

Paraffin embedded tissue sections from tumors from WT and COL1A1 heterozygous mice were obtained from Patricia Keeley's lab at The University of Wisconsin, Madison. Periodic

acid schiff (PAS) stain was performed using a kit from sigma-aldrich following manufacturer?s instructions (detection kit 395B-1kt, Sigma, St. Louis, MO) and imaged at the histology core of the Moore's cancer center (University of California, San Diego).

Bibliography

[1] Trenis D Palmer, William J Ashby, John D Lewis, and Andries Zijlstra. Targeting tumor cell motility to prevent metastasis. *Advanced drug delivery reviews*, 63(8):568–581 2011.

[2] Min Fang, Jingping Yuan, Chunwei Peng, and Yan Li. Collagen as a double-edged sword in tumor progression. *Tumor Biology*, 35(4):2871–2882

[3] Paolo P Provenzano, David R Inman, Kevin W Eliceiri, Justin G Knittel, Long Yan, Curtis T Rueden, John G White, and Patricia J Keely. Collagen density promotes mammary tumor initiation and progression. *BMC medicine*, 6(1):11

[4] GuoGuang Zhu, Antti Kauppila, Leila Risteli, Markus Makinen, Frej Stenback, and Juha Risteli. Immunohistochemical study of type i collagen and type i collagen in benign and malignant ovarian neoplasms. *Cancer*, 75(4):1010–1017

[5] Cole R Drifka, Jo Tod, Agnes G Loeffler, Yuming Liu, Gareth J Thomas, Kevin W Eliceiri, and W John Kao. Periductal stromal collagen topology of pancreatic ductal adenocarcinoma differs from that of normal and chronic pancreatitis. *Modern Pathology*, 28(11):1470

[6] Ivo J Huijbers, Marjan Iravani, Sergey Popov, David Robertson, Safa Al-Sarraj, Chris Jones, and Clare M Isacke. A role for fibrillar collagen deposition and the collagen internalization receptor endo180 in glioma invasion. *PloS one*, 5(3):e9808

[7] Matthew W Conklin, Jens C Eickhoff, Kristin M Riching, Carolyn A Pehlke, Kevin W Eliceiri, Paolo P Provenzano, Andreas Friedl, and Patricia J Keely. Aligned collagen is a prognostic signature for survival in human breast carcinoma. *The American journal of pathology*, 178(3):1221–1232 0002–9440, 2011.

[8] Bojana Gligorijevic, Aviv Bergman, and John Condeelis. Multiparametric classification links tumor microenvironments with tumor cell phenotype. *PLoS biology*, 12(11):e1001995

[9] Silvia Giampieri, Cerys Manning, Steven Hooper, Louise Jones, Caroline S Hill, and Erik Sahai. Localized and reversible tgfβ signalling switches breast cancer cells from cohesive to single cell motility. *Nature cell biology*, 11(11):1287

[10] S. I. Fraley, P. H. Wu, L. He, Y. Feng, R. Krisnamurthy, G. D. Longmore, and D. Wirtz. Three-dimensional matrix fiber alignment modulates cell migration and mt1-mmp utility by spatially and temporally directing protrusions. *Sci Rep*, 5:14580, 2015.

[11] Sanjay Kumar and Valerie M Weaver. Mechanics, malignancy, and metastasis: the force journey of a tumor cell. *Cancer and Metastasis Reviews*, 28(1-2):113–127 2009.

[12] Andrew J Maniotis, Robert Folberg, Angela Hess, Elisabeth A Seftor, Lynn MG Gardner, Jacob Pe'er, Jeffrey M Trent, Paul S Meltzer, and Mary JC Hendrix. Vascular channel formation by human melanoma cells in vivo and in vitro: vasculogenic mimicry. *The American journal of pathology*, 155(3):739–752 0002–9440, 1999.

[13] Mary JC Hendrix, Elisabeth A Seftor, Paul S Meltzer, Lynn MG Gardner, Angela R Hess, Dawn A Kirschmann, Gina C Schatteman, and Richard EB Seftor. Expression and functional significance of ve-cadherin in aggressive human melanoma cells: role in vasculogenic mimicry. *Proc. Natl Acad. Sci. USA*, 98, 2001.

[14] Ji-Gang Zhang, Xiao-Yu Li, Yu-Zhu Wang, Qi-Di Zhang, Sheng-Ying Gu, Xin Wu, Guan-Hua Zhu, Qin Li, and Gao-Lin Liu. Rock is involved in vasculogenic mimicry formation in hepatocellular carcinoma cell line. *PLoS ONE*, 9, 2014.

[15] Stuart C. Williamson, Robert L. Metcalf, Francesca Trapani, Sumitra Mohan, Jenny Antonello, Benjamin Abbott, Hui Sun Leong, Christopher P. E. Chester, Nicole Simms, Radoslaw Polanski, Daisuke Nonaka, Lynsey Priest, Alberto Fusi, Fredrika Carlsson, Anders Carlsson, Mary J. C. Hendrix, Richard E. B. Seftor, Elisabeth A. Seftor, Dominic G. Rothwell, Andrew Hughes, James Hicks, Crispin Miller, Peter Kuhn, Ged Brady, Kathryn L. Simpson, Fiona H. Blackhall, and Caroline Dive. Vasculogenic mimicry in small cell lung cancer. *Nat. Commun.*, 7, 2016.

[16] TJ Liu, BC Sun, XL Zhao, XM Zhao, T Sun, Q Gu, Z Yao, XY Dong, N Zhao, and N Liu. Cd133+ cells with cancer stem cell characteristics associates with vasculogenic mimicry in triple-negative breast cancer. *Oncogene*, 32, 2013.

[17] Elvin Wagenblast, Mar Soto, Sara Gutiérrez-Ángel, Christina A. Hartl, Annika L. Gable, Ashley R. Maceli, Nicolas Erard, Alissa M. Williams, Sun Y. Kim, Steffen Dickopf, J. Chuck Harrell, Andrew D. Smith, Charles M. Perou, John E. Wilkinson, Gregory J. Hannon, and Simon R. V. Knott. A model of breast cancer heterogeneity reveals vascular mimicry as a driver of metastasis. *Nature*, 520, 2015.

[18] R. M. Misra, M. S. Bajaj, and V. P. Kale. Vasculogenic mimicry of ht1080 tumour cells in vivo: critical role of hif-1alpha-neuropilin-1 axis. *PLoS ONE*, 7, 2012.

[19] S. I. Fraley, Y. Feng, R. Krishnamurthy, D. H. Kim, A. Celedon, G. D. Longmore, and D. Wirtz. A distinctive role for focal adhesion proteins in three-dimensional cell motility. *Nat. Cell Biol.*, 12, 2010.

[20] S. I. Fraley, Y. Feng, A. Giri, G. D. Longmore, and D. Wirtz. Dimensional and temporal controls of three-dimensional cell migration by zyxin and binding partners. *Nat. Commun.*, 3, 2012.

[21] S. I. Fraley, Y. Feng, D. Wirtz, and G. D. Longmore. Reply: reducing background fluorescence reveals adhesions in 3d matrices. *Nat. Cell Biol.*, 13, 2010.

[22] A. E. Saliba, A. J. Westermann, S. A. Gorski, and J. Vogel. Single-cell rna-seq: advances and future challenges. *Nucleic Acids Res.*, 42, 2014.

[23] Z. N. Demou and M. J. Hendrix. Microgenomics profile the endogenous angiogenic phenotype in subpopulations of aggressive melanoma. *J. Cell Biochem.*, 105, 2008.

[24] M. J. Hendrix, E. A. Seftor, A. R. Hess, and R. E. Seftor. Vasculogenic mimicry and tumour-cell plasticity: lessons from melanoma. *Nat. Rev. Cancer*, 3, 2003.

[25] M. Valiente. Serpins promote cancer cell survival and vascular co-option in brain metastasis. *Cell*, 156, 2014.

[26] Silvia Rosini, Nicholas Pugh, Arkadiusz M Bonna, David JS Hulmes, Richard W Farndale, and Josephine C Adams. Thrombospondin-1 promotes matrix homeostasis by interacting with collagen and lysyl oxidase precursors and collagen cross-linking sites. *Sci. Signal.*, 11(532):eaar2566, 2018.

[27] M. Barczyk, S. Carracedo, and D. Gullberg. Integrins. *Cell Tissue Res.*, 339, 2010.

[28] C. J. Brinkerhoff and J. J. Linderman. Integrin dimerization and ligand organization: key components in integrin clustering for cell adhesion. *Tissue Eng. Part A*, 11, 2005.

[29] J. Taipale and J. Keski-Oja. Growth factors in the extracellular matrix. *FASEB J.*, 11, 1997.

[30] L. M. Przybyla, T. W. Theunissen, R. Jaenisch, and J. Voldman. Matrix remodeling maintains embryonic stem cell self-renewal by activating stat3. *Stem Cells*, 31, 2013.

[31] Zuzana Koledova, Xiaohong Zhang, Charles Streuli, Robert B Clarke, Ophir D Klein, Zena Werb, and Pengfei Lu. Spry1 regulates mammary epithelial morphogenesis by modulating egfr-dependent stromal paracrine signaling and ecm remodeling. *Proc. Natl Acad. Sci. USA*, 113, 2016.

[32] Saroja Ramanujan, Alain Pluen, Trevor D McKee, Edward B Brown, Yves Boucher, and Rakesh K Jain. Diffusion and convection in collagen gels: implications for transport in the tumor interstitium. *Biophys J.*, 83, 2002.

[33] H. E. Abaci, R. Truitt, S. Tan, and S. Gerecht. Unforeseen decreases in dissolved oxygen levels affect tube formation kinetics in collagen gels. *Am. J. Physiol. Cell Physiol.*, 301, 2011.

[34] Daisy WJ Van Der Schaft, Femke Hillen, Patrick Pauwels, Dawn A Kirschmann, Karolien Castermans, Mirjam GA oude Egbrink, Maxine GB Tran, Rafael Sciot, Esther Hauben, and Pancras CW Hogendoorn. Tumor cell plasticity in ewing sarcoma, an alternative circulatory system stimulated by hypoxia. *Cancer Res.*, 65, 2005.

[35] Baocun Sun, Danfang Zhang, Shiwu Zhang, Wenzhi Zhang, Hua Guo, and Xiulan Zhao. Hypoxia influences vasculogenic mimicry channel formation and tumor invasion-related protein expression in melanoma. *Cancer Lett.*, 249, 2007.

[36] Bernard Thienpont, Jessica Steinbacher, Hui Zhao, Flora D'Anna, Anna Kuchnio, Athanasios Ploumakis, Bart Ghesquière, Laurien Van Dyck, Bram Boeckx, Luc Schoonjans, Els Hermans, Frederic Amant, Vessela N. Kristensen, Kian Peng Koh, Massimiliano Mazzone, Mathew L. Coleman, Thomas Carell, Peter Carmeliet, and Diether Lambrechts. Tumour hypoxia causes dna hypermethylation by reducing tet activity. *Nature*, 537, 2016.

[37] Flora Cimmino, Lucia Pezone, Marianna Avitabile, Giovanni Acierno, Immacolata Andolfo, Mario Capasso, and Achille Iolascon. Inhibition of hypoxia inducible factors combined with all-trans retinoic acid treatment enhances glial transdifferentiation of neuroblastoma cells. *Scientific reports*, 5, 2015.

[38] Anna Janaszak-Jasiecka, Sylwia Bartoszewska, Kinga Kochan, Arkadiusz Piotrowski, Leszek Kalinowski, Wojciech Kamysz, Renata J Ochocka, Rafał Bartoszewski, and James F Collawn. mir-429 regulates the transition between hypoxia-inducible factor (hif)1a and hif3a expression in human endothelial cells. *Scientific reports*, 6, 2016.

[39] Richard EB Seftor, Angela R Hess, Elisabeth A Seftor, Dawn A Kirschmann, Katharine M Hardy, Naira V Margaryan, and Mary JC Hendrix. Tumor cell vasculogenic mimicry: from controversy to therapeutic promise. *The American journal of pathology*, 181, 2012.

[40] H. Lahlou and W. J. Muller. β1-integrins signaling and mammary tumor progression in transgenic mouse models: implications for human breast cancer. *Breast Cancer Res.*, 13, 2011.

[41] Richard EB Seftor, Elisabeth A Seftor, Naohiko Koshikawa, Paul S Meltzer, Lynn MG Gardner, Martin Bilban, William G Stetler-Stevenson, Vito Quaranta, and Mary JC Hendrix. Cooperative interactions of laminin 5 gamma2 chain, matrix metalloproteinase-2, and membrane type-1-matrix/metalloproteinase are required for mimicry of embryonic vasculogenesis by aggressive melanoma. *Cancer Res.*, 61, 2001.

[42] L. Castro-Sanchez, A. Soto-Guzman, M. Guaderrama-Diaz, P. Cortes-Reynosa, and E. P. Salazar. Role of ddr1 in the gelatinases secretion induced by native type iv collagen in mda-mb-231 breast cancer cells. *Clin. Exp. Metastasis*, 28, 2011.

[43] Nadia Howlader, Sean F Altekruse, Christopher I Li, Vivien W Chen, Christina A Clarke, Lynn AG Ries, and Kathleen A Cronin. Us incidence of breast cancer subtypes defined by joint hormone receptor and her2 status. *Journal of the National Cancer Institute*, 106(5), 2014.

[44] Mathias Uhlén, Linn Fagerberg, Björn M. Hallström, Cecilia Lindskog, Per Oksvold, Adil Mardinoglu, Åsa Sivertsson, Caroline Kampf, Evelina Sjöstedt, Anna Asplund, IngMarie Olsson, Karolina Edlund, Emma Lundberg, Sanjay Navani, Cristina Al-Khalili Szigyarto, Jacob Odeberg, Dijana Djureinovic, Jenny Ottosson Takanen, Sophia Hober, Tove Alm, Per-Henrik Edqvist, Holger Berling, Hanna Tegel, Jan Mulder, Johan Rockberg, Peter Nilsson, Jochen M. Schwenk, Marica Hamsten, Kalle von Feilitzen, Mattias Forsberg, Lukas Persson, Fredric Johansson, Martin Zwahlen, Gunnar von Heijne, Jens Nielsen, and Fredrik Pontén. Proteomics. tissue-based map of the human proteome. *Science*, 347, 2015.

[45] N. Jain, K. V. Iyer, A. Kumar, and G. V. Shivashankar. Cell geometric constraints induce modular gene-expression patterns via redistribution of hdac3 regulated by actomyosin contractility. *Proc. Natl Acad. Sci. USA*, 110, 2013.

[46] R. P. Jean, D. S. Gray, A. A. Spector, and C. S. Chen. Characterization of the nuclear deformation caused by changes in endothelial cell shape. *J. Biomech. Eng.*, 126, 2004.

[47] M. Versaevel, T. Grevesse, and S. Gabriele. Spatial coordination between cell and nuclear shape within micropatterned endothelial cells. *Nat. Commun.*, 3, 2012.

[48] M. Thery, A. Pepin, E. Dressaire, Y. Chen, and M. Bornens. Cell distribution of stress fibres in response to the geometry of the adhesive environment. *Cell Motil. Cytoskeleton*, 63, 2006.

[49] L. Vergani, M. Grattarola, and C. Nicolini. Modifications of chromatin structure and gene expression following induced alterations of cellular shape. *Int. J. Biochem. Cell Biol.*, 36, 2004.

[50] JP Yang, YD Liao, DM Mai, P Xie, YY Qiang, LS Zheng, MY Wang, Y Mei, DF Meng, and L Xu. Tumor vasculogenic mimicry predicts poor prognosis in cancer patients: a meta-analysis. *Angiogenesis*, 19, 2016.

[51] P. H. Wu, A. Giri, S. X. Sun, and D. Wirtz. Three-dimensional cell migration does not follow a random walk. *Proc. Natl Acad. Sci. USA*, 111, 2014.

[52] P. H. Wu, A. Giri, and D. Wirtz. Statistical analysis of cell migration in 3d using the anisotropic persistent random walk model. *Nat. Protoc.*, 10, 2015.

[53] A. Roberts and L. Pachter. Streaming fragment assignment for real-time analysis of sequencing experiments. *Nat. Methods*, 10, 2013.

[54] Ophir Shalem, Neville E. Sanjana, Ella Hartenian, Xi Shi, David A. Scott, Tarjei S. Mikkelsen, Dirk Heckl, Benjamin L. Ebert, David E. Root, John G. Doench, and Feng Zhang. Genome-scale crispr-cas9 knockout screening in human cells. *Science*, 343, 2014.

[55] Christopher Wilks, Melissa S. Cline, Erich Weiler, Mark Diehkans, Brian Craft, Christy Martin, Daniel Murphy, Howdy Pierce, John Black, Donavan Nelson, Brian Litzinger,

Thomas Hatton, Lori Maltbie, Michael Ainsworth, Patrick Allen, Linda Rosewood, Elizabeth Mitchell, Bradley Smith, Jim Warner, John Groboske, Haifang Telc, Daniel Wilson, Brian Sanford, Hannes Schmidt, David Haussler, and Daniel Maltbie. The cancer genomics hub (cghub): overcoming cancer through the power of torrential data. *Database*, 2014:bau093, 2014.

[56] R. Patro, S. M. Mount, and C. Kingsford. Sailfish enables alignment-free isoform quantification from rna-seq reads using lightweight algorithms. *Nat. Biotechnol.*, 32, 2014.

[57] Andrew M Gross, Ryan K Orosco, John P Shen, Ann Marie Egloff, Hannah Carter, Matan Hofree, Michel Choueiri, Charles S Coffey, Scott M Lippman, D Neil Hayes, Ezra E Cohen, Jennifer R Grandis, Quyen T Nguyen, and Trey Ideker. Multi-tiered genomic analysis of head and neck cancer ties tp53 mutation to 3p loss. *Nature Genetics*, 46:939 EP –, 08 2014.

[58] Kevin J Cheung and Andrew J Ewald. A collective route to metastasis: Seeding by tumor cell clusters. *Science*, 352(6282):167–169, 2016.

[59] Joan Massagué and Anna C Obenauf. Metastatic colonization by circulating tumour cells. *Nature*, 529(7586):298, 2016.

[60] Kevin J Cheung, Veena Padmanaban, Vanesa Silvestri, Koen Schipper, Joshua D Cohen, Amanda N Fairchild, Michael A Gorin, James E Verdone, Kenneth J Pienta, and Joel S Bader. Polyclonal breast cancer metastases arise from collective dissemination of keratin 14-expressing tumor cell clusters. *Proceedings of the National Academy of Sciences*, 113(7):E854–E863, 2016.

[61] Wentao Shi, Jean Kwon, Yongyang Huang, Jifu Tan, Christopher G Uhl, Ran He, Chao Zhou, and Yaling Liu. Facile tumor spheroids formation in large quantity with controllable size and high uniformity. *Scientific reports*, 8(1):6837, 2018.

[62] Daniela Loessner, Kathryn S Stok, Matthias P Lutolf, Dietmar W Hutmacher, Judith A Clements, and Simone C Rizzi. Bioengineered 3d platform to explore cell–ecm interactions and drug resistance of epithelial ovarian cancer cells. *Biomaterials*, 31(32):8494–8506, 2010.

[63] Nicola Aceto, Aditya Bardia, David T Miyamoto, Maria C Donaldson, Ben S Wittner, Joel A Spencer, Min Yu, Adam Pely, Amanda Engstrom, and Huili Zhu. Circulating tumor cell clusters are oligoclonal precursors of breast cancer metastasis. *Cell*, 158(5):1110–1122, 2014.

[64] Colin D Paul, Panagiotis Mistriotis, and Konstantinos Konstantopoulos. Cancer cell motility: lessons from migration in confined spaces. *Nature Reviews Cancer*, 2016.

[65] K. Wolf, M. te Lindert, M. Krause, S. Alexander, J. te Riet, A. L. Willis, R. M. Hoffman, C. G. Figdor, S. J. Weiss, and P. Friedl. *Physical limits of cell migration: Control by ECM*

space and nuclear deformation and tuning by proteolysis and traction force, volume 201, pages 1069–84. 2013.

[66] DO Velez, B Tsui, T Goshia, CL Chute, A Han, H Carter, and SI Fraley. 3d collagen architecture induces a conserved migratory and transcriptional response linked to vasculogenic mimicry. *Nature communications*, 8(1):1651, 2017.

[67] Britta Trappmann, Brendon M Baker, William J Polacheck, Colin K Choi, Jason A Burdick, and Christopher S Chen. Matrix degradability controls multicellularity of 3d cell migration. *Nature communications*, 8(1):371, 2017.

[68] Lori Kornberg, H Shelton Earp, J Thomas Parsons, Michael Schaller, and RL Juliano. Cell adhesion or integrin clustering increases phosphorylation of a focal adhesion-associated tyrosine kinase. *Journal of Biological Chemistry*, 267(33):23439–23442, 1992.

[69] Abdelkader Hamadi, Maya Bouali, Monique Dontenwill, Herrade Stoeckel, Kenneth Takeda, and Philippe Rondé. Regulation of focal adhesion dynamics and disassembly by phosphorylation of fak at tyrosine 397. *Journal of cell science*, 118(19):4415–4425, 2005.

[70] Zachary T Schafer, Alexandra R Grassian, Loling Song, Zhenyang Jiang, Zachary Gerhart-Hines, Hanna Y Irie, Sizhen Gao, Pere Puigserver, and Joan S Brugge. Antioxidant and oncogene rescue of metabolic defects caused by loss of matrix attachment. *Nature*, 461(7260):109, 2009.

[71] Lei Jiang, Alexander A Shestov, Pamela Swain, Chendong Yang, Seth J Parker, Qiong A Wang, Lance S Terada, Nicholas D Adams, Michael T McCabe, and Beth Pietrak. Reductive carboxylation supports redox homeostasis during anchorage-independent growth. *Nature*, 532(7598):255, 2016.

[72] Boyi Gan, Youngdong Yoo, and Jun-Lin Guan. Association of focal adhesion kinase with tuberous sclerosis complex 2 in the regulation of s6 kinase activation and cell growth. *Journal of Biological Chemistry*, 281(49):37321–37329, 2006.

[73] Katrin Düvel, Jessica L Yecies, Suchithra Menon, Pichai Raman, Alex I Lipovsky, Amanda L Souza, Ellen Triantafellow, Qicheng Ma, Regina Gorski, and Stephen Cleaver. Activation of a metabolic gene regulatory network downstream of mtor complex 1. *Molecular cell*, 39(2):171–183, 2010.

[74] AR Grassian, JL Coloff, and JS Brugge. Extracellular matrix regulation of metabolism and implications for tumorigenesis. In *Cold Spring Harbor symposia on quantitative biology*, volume 76, pages 313–324. Cold Spring Harbor Laboratory Press.

[75] Alexandra R Grassian, Christian M Metallo, Jonathan L Coloff, Gregory Stephanopoulos, and Joan S Brugge. Erk regulation of pyruvate dehydrogenase flux through pdk4 modulates cell proliferation. *Genes and development*, 25(16):1716–1733, 2011.

[76] Brendan P Flynn, Amit P Bhole, Nima Saeidi, Melody Liles, Charles A DiMarzio, and Jeffrey W Ruberti. Mechanical strain stabilizes reconstituted collagen fibrils against enzymatic degradation by mammalian collagenase matrix metalloproteinase 8 (mmp-8). *PLoS One*, 5(8):e12337, 2010.

[77] Christopher Jedeszko, Mansoureh Sameni, Mary B Olive, Kamiar Moin, and Bonnie F Sloane. Visualizing protease activity in living cells: from two dimensions to four dimensions. *Current protocols in cell biology*, pages 4.20. 1–4.20. 15, 2008.

[78] Maria C Melander, Henrik J Jürgensen, Daniel H Madsen, Lars H Engelholm, and Niels Behrendt. The collagen receptor uparap/endo180 in tissue degradation and cancer. *International journal of oncology*, 47(4):1177–1188, 2015.

[79] Daniel H Madsen, Lars H Engelholm, Signe Ingvarsen, Thore Hillig, Rebecca A Wagenaar-Miller, Lars Kjøller, Henrik Gårdsvoll, Gunilla Høyer-Hansen, Kenn Holmbeck, and Thomas H Bugge. Extracellular collagenases and the endocytic receptor, urokinase plasminogen activator receptor-associated protein/endo180, cooperate in fibroblast-mediated collagen degradation. *Journal of Biological Chemistry*, 282(37):27037–27045, 2007.

[80] Brendan D'Souza, Laurence Meloty-Kapella, and Gerry Weinmaster. *Canonical and non-canonical Notch ligands*, volume 92, pages 73–129. Elsevier, 2010.

[81] Orianne Olivares, Jared R Mayers, Victoire Gouirand, Margaret E Torrence, Tristan Gicquel, Laurence Borge, Sophie Lac, Julie Roques, Marie-Noëlle Lavaut, and Patrice Berthezène. Collagen-derived proline promotes pancreatic ductal adenocarcinoma cell survival under nutrient limited conditions. *Nature communications*, 8:16031, 2017.

[82] Cosimo Commisso, Shawn M Davidson, Rengin G Soydaner-Azeloglu, Seth J Parker, Jurre J Kamphorst, Sean Hackett, Elda Grabocka, Michel Nofal, Jeffrey A Drebin, and Craig B Thompson. Macropinocytosis of protein is an amino acid supply route in ras-transformed cells. *Nature*, 497(7451):633, 2013.

[83] TJ Liu, BC Sun, XL Zhao, XM Zhao, T Sun, Q Gu, Z Yao, XY Dong, N Zhao, and N Liu. Cd133+ cells with cancer stem cell characteristics associates with vasculogenic mimicry in triple-negative breast cancer. *Oncogene*, 32(5):544–553, 2013.

[84] D. Gingras, M. Page, B. Annabi, and R. Beliveau. Rapid activation of matrix metalloproteinase-2 by glioma cells occurs through a posttranslational mt1-mmp-dependent mechanism. *Biochim Biophys Acta*, 1497(3):341–50, 2000.

[85] A. Haeger, M. Krause, K. Wolf, and P. Friedl. Cell jamming: collective invasion of mesenchymal tumor cells imposed by tissue confinement. *Biochim Biophys Acta*, 1840(8):2386–95, 2014.

[86] Katarina Wolf and Peter Friedl. Extracellular matrix determinants of proteolytic and non-proteolytic cell migration. *Trends in cell biology*, 21(12):736–744, 2011.

[87] Michael J Morgan and Zheng-gang Liu. Crosstalk of reactive oxygen species and nf-Î°b signaling. *Cell research*, 21(1):103, 2011.

[88] Yunbiao Lu and Larry M Wahl. Oxidative stress augments the production of matrix metalloproteinase-1, cyclooxygenase-2, and prostaglandin e2 through enhancement of nf-Î°b activity in lipopolysaccharide-activated human primary monocytes. *The Journal of Immunology*, 175(8):5423–5429, 2005.

[89] Chunhong Yan and Douglas D Boyd. Regulation of matrix metalloproteinase gene expression. *Journal of cellular physiology*, 211(1):19–26, 2007.

[90] Ella Kratsovnik, Yael Bromberg, Oded Sperling, and Esther Zoref-Shani. Oxidative stress activates transcription factor nf-Î°b-mediated protective signaling in primary rat neuronal cultures. *Journal of molecular neuroscience*, 26(1):27–32, 2005.

[91] Eric Theveneau and Claudia Linker. Leaders in collective migration: are front cells really endowed with a particular set of skills? *F1000Research*, 6, 2017.

[92] Reza Riahi, Jian Sun, Shue Wang, Min Long, Donna D Zhang, and Pak Kin Wong. Notch1–dll4 signalling and mechanical force regulate leader cell formation during collective cell migration. *Nature communications*, 6:6556, 2015.

[93] Masahiro Sonoshita, Yoshiro Itatani, Fumihiko Kakizaki, Kenji Sakimura, Toshio Terashima, Yu Katsuyama, Yoshiharu Sakai, and M Mark Taketo. Promotion of colorectal cancer invasion and metastasis through activation of notch–dab1–abl–rhogef protein trio. *Cancer discovery*, 2014.

[94] Andreas Fischer, Nina Schumacher, Manfred Maier, Michael Sendtner, and Manfred Gessler. The notch target genes hey1 and hey2 are required for embryonic vascular development. *Genes and development*, 18(8):901–911, 2004.

[95] Eleni Maniati, Maud Bossard, Natalie Cook, Juliana B Candido, Nia Emami-Shahri, Sergei A Nedospasov, Frances R Balkwill, David A Tuveson, and Thorsten Hagemann. Crosstalk between the canonical nf-kb and notch signaling pathways inhibits pparγ expression and promotes pancreatic cancer progression in mice. *The Journal of clinical investigation*, 121(12):4685–4699, 2011.

[96] Nicolas Coant, Sanae Ben Mkaddem, Eric Pedruzzi, Cécile Guichard, Xavier Tréton, Robert Ducroc, Jean-Noel Freund, Dominique Cazals-Hatem, Yoram Bouhnik, and Paul-Louis Woerther. Nadph oxidase 1 modulates wnt and notch1 signaling to control the fate of proliferative progenitor cells in the colon. *Molecular and cellular biology*, 30(11):2636–2650, 2010.

[97] C Caliceti, P Nigro, P Rizzo, and R Ferrari. Ros, notch, and wnt signaling pathways: crosstalk between three major regulators of cardiovascular biology. *BioMed research international*, 2014, 2014.

[98] Katarina Wolf, Yi I Wu, Yueying Liu, Jörg Geiger, Eric Tam, Christopher Overall, M Sharon Stack, and Peter Friedl. Multi-step pericellular proteolysis controls the transition from individual to collective cancer cell invasion. *Nature cell biology*, 9(8):893, 2007.

[99] Sudhir Khetan, Murat Guvendiren, Wesley R Legant, Daniel M Cohen, Christopher S Chen, and Jason A Burdick. Degradation-mediated cellular traction directs stem cell fate in covalently crosslinked three-dimensional hydrogels. *Nature materials*, 12(5):458, 2013.

[100] A. Das, M. Monteiro, A. Barai, S. Kumar, and S. Sen. Mmp proteolytic activity regulates cancer invasiveness by modulating integrins. *Sci Rep*, 7(1):14219, 2017.

[101] C. L. Hoop, J. Zhu, A. M. Nunes, D. A. Case, and J. Baum. Revealing accessibility of cryptic protein binding sites within the functional collagen fibril. *Biomolecules*, 7(4), 2017.

[102] S. A. Jimenez, R. I. Bashey, M. Benditt, and R. Yankowski. Identification of collagen alpha1(i) trimer in embryonic chick tendons and calvaria. *Biochem Biophys Res Commun*, 78(4):1354–61, 1977.

[103] H. Lesot, V. Karcher-Djuricic, and J. V. Ruch. Synthesis of collagen type i, type i trimer and type iii by embryonic mouse dental epithelial and mesenchymal cells in vitro. *Biochim Biophys Acta*, 656(2):206–12, 1981.

[104] A. S. Narayanan, R. C. Page, and D. F. Meyers. Characterization of collagens of diseased human gingiva. *Biochemistry*, 19(22):5037–43, 1980.

[105] M. Rojkind, M. A. Giambrone, and L. Biempica. Collagen types in normal and cirrhotic liver. *Gastroenterology*, 76(4):710–9, 1979.

[106] H. P. Ehrlich, H. Brown, and B. S. White. Evidence for type v and i trimer collagens in dupuytren's contracture palmar fascia. *Biochem Med*, 28(3):273–84, 1982.

[107] E. Makareeva, S. Han, J. C. Vera, D. L. Sackett, K. Holmbeck, C. L. Phillips, R. Visse, H. Nagase, and S. Leikin. Carcinomas contain a matrix metalloproteinase-resistant isoform of type i collagen exerting selective support to invasion. *Cancer Res*, 70(11):4366–74, 2010.

[108] Y. A. DeClerck, E. T. Bomann, B. A. Spengler, and J. L. Biedler. Differential collagen biosynthesis by human neuroblastoma cell variants. *Cancer Res*, 47(24 Pt 1):6505–10, 1987.

[109] J. H. Rupard, S. J. Dimari, I. Damjanov, and M. A. Haralson. Synthesis of type i homotrimer collagen molecules by cultured human lung adenocarcinoma cells. *Am J Pathol*, 133(2):316–26, 1988.

[110] C. D. Little, R. L. Church, R. A. Miller, and F. H. Ruddle. Procollagen and collagen produced by a teratocarcinoma-derived cell line, tsd4: evidence for a new molecular form of collagen. *Cell*, 10(2):287–95, 1977.

[111] S. Minafra, C. Luparello, F. Rallo, and I. Pucci-Minafra. Collagen biosynthesis by a breast carcinoma cell strain and biopsy fragments of the primary tumour. *Cell Biol Int Rep*, 12(10):895–905, 1988.

[112] S. I. Fraley, Y. Feng, R. Krishnamurthy, D. H. Kim, A. Celedon, G. D. Longmore, and D. Wirtz. A distinctive role for focal adhesion proteins in three-dimensional cell motility. *Nature Cell Biology*, 12(6):598–604, 2010.

[113] S. I. Fraley, Y. Feng, A. Giri, G. D. Longmore, and D. Wirtz. Dimensional and temporal controls of three-dimensional cell migration by zyxin and binding partners. *Nature Communications*, 3:719, 2012.

[114] Anthony Han, Sural Ranamukhaarachchi, Daniel O Velez, Aditya Kumar, Adam J Engler, and Stephanie I Fraley. Crowding tunes 3d collagen fibrils and reveals matrix regulation of cancer cell morphogenesis. *bioRxiv*, page 274696, 2018.

[115] Jeremy S Bredfeldt, Yuming Liu, Matthew W Conklin, Patricia J Keely, Thomas R Mackie, and Kevin W Eliceiri. Automated quantification of aligned collagen for human breast carcinoma prognosis. *Journal of pathology informatics*, 5, 2014.

[116] Jeremy S Bredfeldt, Yuming Liu, Carolyn A Pehlke, Matthew W Conklin, Joseph M Szulczewski, David R Inman, Patricia J Keely, Robert D Nowak, Thomas R Mackie, and Kevin W Eliceiri. Computational segmentation of collagen fibers from second-harmonic generation images of breast cancer. *Journal of biomedical optics*, 19(1):016007–016007, 2014.

[117] Norman F Boyd, Gillian S Dite, Jennifer Stone, Anoma Gunasekara, Dallas R English, Margaret RE McCredie, Graham G Giles, David Tritchler, Anna Chiarelli, and Martin J Yaffe. Heritability of mammographic density, a risk factor for breast cancer. *New England Journal of Medicine*, 347(12):886–894 0028–4793, 2002.

[118] Norman F Boyd, Gina A Lockwood, Jeff W Byng, David L Tritchler, and Martin J Yaffe. Mammographic densities and breast cancer risk. *Cancer Epidemiology and Prevention Biomarkers*, 7(12):1133–1144

[119] Xin Liu, Hong Wu, Michael Byrne, John Jeffrey, Stephen Krane, and Rudolf Jaenisch. A targeted mutation at the known collagenase cleavage site in mouse type i collagen impairs tissue remodeling. *The Journal of cell biology*, 130(1):227–237 1995.

[120] Elizabeth Iorns, Katherine Drews-Elger, Toby M Ward, Sonja Dean, Jennifer Clarke, Deborah Berry, Dorraya El Ashry, and Marc Lippman. A new mouse model for the study of human breast cancer metastasis. *PloS one*, 7(10):e47995

[121] Madhavi Puchalapalli, Xianke Zeng, Liang Mu, Aubree Anderson, Laura Hix Glickman, Ming Zhang, Megan R Sayyad, Sierra Mosticone Wangensteen, Charles V Clevenger, and Jennifer E Koblinski. Nsg mice provide a better spontaneous model of breast cancer metastasis than athymic (nude) mice. *PloS one*, 11(9):e0163521

[122] Mary JC Hendrix, Elisabeth A Seftor, Angela R Hess, and Richard EB Seftor. Angiogenesis: Vasculogenic mimicry and tumour-cell plasticity: lessons from melanoma. *Nature Reviews Cancer*, 3(6):411